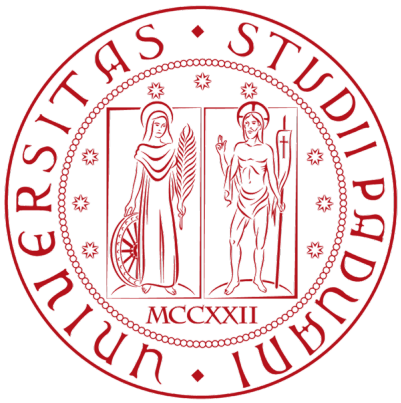

Università degli Studi di Padova

Department of Physics and Astronomy "Galileo Galilei"
Ph.D. in Physics

Final Dissertation

Quantum Probes of the Standard Model: Muon g-2 and Higgs Physics

Coordinator:
Prof. Giulio Monaco

Thesis Supervisors:
Prof.ssa Ramona Gröber
Dr. Massimo Passera

Ph.D. Student
Elisa Balzani
Matriculation Number
2018159

Cycle XXXVI

Abstract

The main uncertainty of the Standard Model prediction of the muon g-2 originates from its hadronic vacuum polarization (HVP) contribution, which cannot be reliably calculated perturbatively in QCD and relies on experimental data as input to dispersion relations. Traditionally, this contribution has been computed via a dispersive, or time-like, integral using hadronic production cross-sections in low energy electron-positron annihilation. A novel approach to determine the HVP contribution to the muon g-2 is desirable. In the first part of this work we present simple analytic expressions to compute the HVP contribution to the muon g-2 in the space-like region up to next-to-next-to-leading order. After that, we derive approximations for the euclidean-time kernel obtained from the HVP contributions in the space-like region up to next-to-leading order. The series expansions presented in this work overcome the problems given by their asymptotic behaviour for large value of the time. These results can be employed in lattice QCD calculations of this contribution as well as in space-like determinations based on scattering data, like that expected from the proposed MUonE experiment at CERN.

For the second part of this thesis, we focus on the constraints of the Yukawa couplings of the first-generation quarks, which are notoriously challenging to determine due to their small values within the framework of the Standard Model. We propose the utilization of off-shell Higgs production, where the Higgs boson decays into four leptons, as a method to investigate the up- and down-quark Yukawa couplings. Employing kinematic discriminants akin to those utilized in Higgs width measurements, we have found that the down (up) Yukawa coupling can be constrained to approximately 156 (260) times its Standard Model value, considering only experimental systematic uncertainties, in a high-luminosity LHC scenario. This approach to off-shell Higgs production demonstrates superior sensitivity to the first-generation quark Yukawa couplings compared to other methods, such as Higgs+jet or Higgs pair production.

This work is based on the research carried on by the author during her Ph.D. studies at the Università degli Studi di Padova, Dipartimento di Fisica e Astronomia Galileo Galilei.

Articles:

1. E. Balzani, S. Laporta and M. Passera, "Hadronic vacuum polarization contributions to the muon g-2 in the space-like region," Phys. Lett. B **834** (2022), 137462 [arXiv:2112.05704 [hep-ph]].

2. E. Balzani, R. Gröber and M. Vitti, "Light-quark Yukawa couplings from off-shell Higgs production," JHEP **10** (2023), 027 [arXiv:2304.09772 [hep-ph]].

3. E. Balzani, S. Laporta and M. Passera, "Time-kernel for lattice determinations of NLO hadronic vacuum polarization contributions to the muon g-2," in progress.

Contents

Chapter 1

Introduction

The Standard Model (SM) of particle physics forms the basis of our understanding of the fundamental interactions. More precisely, the SM is the quantum field theory (QFT) that describes how the basic matter constituents (quarks and leptons) interact at the microscopic level via weak, strong, and electromagnetic forces. While all data from earth-based laboratory experiments agree with the SM predictions, there is indirect evidence, derived from cosmological observations, that the model is not complete: this model does not explain the baryon asymmetry of the universe, dark matter, and dark energy. These are all phenomena that could naturally find their explanation in the domain of particle physics or, more generally, within QFT. There are also theoretical concerns about the SM itself, such as the strong sensitivity of the Higgs mass term to high-energy modes in the renormalization procedure (the so-called hierarchy problem), the absence of an explanation for the hierarchical structure of the fermion spectrum, and the lack of a bridge to quantum gravity. Last but not least, non-vanishing neutrino masses cannot be accounted for by the classical version of the SM, containing only left-handed neutrinos and renormalizable interactions.

A long-standing discrepancy between SM predictions and observations concerns the anomalous magnetic moment of the muon, $a_\mu = (g_\mu - 2)/2$. Therefore, a_μ plays an important role in testing the SM of fundamental interactions. The Muon g-2 (E989) experiment at Fermilab has recently presented its measurement of a_μ [1, 2], confirming the earlier results of the E821 experiment at Brookhaven [3]. By the end of its run, the E989 experiment is expected to achieve an unprecedented precision of 0.14 parts-per million (ppm) for the muon anomalous magnetic moment. In addition, a completely new low-energy approach to measuring the muon g-2 is being developed by the E34 collaboration at J-PARC [4].

The present muon g-2 experimental average shows an intriguing 5.1σ discrepancy with the value of the SM a_μ prediction quoted by the Muon g-2 Theory Initiative [5]. If confirmed with high significance, this discrepancy would be indirect evidence for new physics beyond the SM.

On the theory side, the hadronic correction to the muon g-2 are under close scrutiny, as they induce the leading uncertainty of the SM prediction of $a_\mu^{\rm SM}$. The calculation of the leading hadronic contribution to the muon g-2, $a_\mu^{\rm HLO}$, traditionally relies on a

dispersive, or time-like, integral using the hadronic production cross section in electron-positron annihilation at low energies. The present time-like calculation of the hadronic vacuum polarization contribution $a_\mu^{\rm HVP}$ includes the leading-order (LO), next-to-leading-order (NLO) and next-to-next-to-leading-order (NNLO) terms [6]-[14]. The NNLO term is comparable to the final uncertainty of the a_μ measurement expected from the Muon g-2 experiment at Fermilab.

Alternative evaluations of $a_\mu^{\rm HLO}$ can be obtained via lattice QCD [15]-[24]. In 2021 the BMW lattice QCD collaboration (BMWc) computed the leading order HVP contribution $a_\mu^{\rm HLO}$ with a sub-percent precision, finding a value larger than that obtained by the dispersive approach [25]. The so-called window quantities, derived by incorporating weight functions into the Euclidean-time integral of the coordinate-space representation of HVP [17], has emerged as a valuable tool, as the intermediate window is significantly less susceptible to lattice systematics compared to the overall HVP contribution to a_μ. The BMWc value associated with this quantity exhibits a tension of 3.7σ with the cross-section data [27], and several lattice collaborations have now confirmed this result [28]-[31]. In addition, a new preliminary measurement of $e^+e^- \to \pi^+\pi^-$ cross section from the CMD-3 experiment [26] disagrees significantly with all other e^+e^- data used in [5].

Therefore a new and competitive determination of $a_\mu^{\rm HVP}$, possibly at NNLO accuracy, based on a method alternative to the time-like and lattice QCD ones, is desirable.

Recently, a new experiment, MUonE, has been proposed at CERN to determine the leading order hadronic contribution to the muon g-2, measuring the effective electromagnetic coupling in the space-like region via scattering data [32]-[34]. The elastic scattering of high energy muons on atomic electrons has been identified as an ideal process for this measurement. In order to reach a determination of the HVP contribution with a precision below one percent, the *shape* of the μe differential cross section must be measured with a systematic uncertainty of the order of 10 ppm or better. An analogous precision is therefore required in the theoretical prediction [32], [35]-[54].

Goal of the first part of this thesis is to present analytic expressions to compute the hadronic vacuum polarization contribution to the muon g-2 in the space-like region up to NNLO. In Chapter 2 we introduce the anomalous magnetic moment of the muon and the current status of the theoretical prediction. In Chapter 3 we discuss the MUonE proposal focusing on the space-like kernels for the HVP. At LO, simple results are long known and form the basis for present lattice QCD and future MUonE determinations of $a_\mu^{\rm HVP}$(LO). Our goal is to provide simple analytic expressions to extend the space-like calculation of the $a_\mu^{\rm HVP}$ contribution to NNLO. Chapter 4 is dedicated to the evaluation of the kernels functions in the time-momentum representation, often used in the lattice QCD calculations.

In the relentless pursuit of understanding the fundamental laws governing the universe, the discovery of the Higgs boson at the Large Hadron Collider (LHC) has represented a significant milestone. The observation of a scalar resonance, with a mass approximately 125 GeV [55, 56], by ATLAS and CMS experiments, has marked the discovery of the last missing ingredient of the SM [57]-[60] of particle physics. Notably, this observation has provided substantial evidence supporting the mechanism of spontaneous Electro-Weak Symmetry Breaking (EWSB) [61]-[66] as the theoretical framework for comprehending the

origin of the masses of the SM particles. The Higgs sector of the SM consists of an $SU(2)$ doublet scalar field that acquires a non-zero vacuum expectation value (VEV), thereby spontaneously breaking the $SU(2) \times U(1)$ EW symmetry. Through the interactions between the Higgs field and the weak gauge bosons, as well as the fermions, their masses can be accounted for in a manner consistent with the fundamental principle of gauge symmetry. By measuring the Higgs mass through the LHC experiments and combining it with the knowledge of the VEV obtained from muon decay, unambiguous predictions within the framework of the SM can be made.

While the Higgs boson couplings to gauge bosons and to third-generation fermions have been measured at the $O(5-20\%)$ level [67, 68], little is known about the Higgs boson couplings to first- and second-generation quarks and leptons, with the exception of the Higgs coupling to muons [69, 70]. For the first- and second-generation quark Yukawa couplings the current best limits are obtained from a global fit. It was found that the modification factor $\kappa_q = y_q/y_q^{\mathrm{SM}}$ of the quark Yukawa coupling y_q with respect to its Standard Model (SM) value y_q^{SM} can be constrained to $\kappa_u < 560$, $\kappa_d < 260$, $\kappa_s < 13$ and $\kappa_c < 1.2$ even at the HL-LHC [71]. This analysis is not completely model-independent; rather, it relies on the assumption that the light-quark Yukawa couplings can be constrained from the Higgs untagged branching ratio. A more direct way of constraining these couplings is hence welcome.

In the second part of this thesis we study a direct probe of the first-generation quark Yukawa couplings; more specifically, the measurement of an off-shell Higgs boson decaying to a Z boson pair that subsequently decays to leptons. A study of light quark Yukawa couplings for the $h \to ZZ$ final state has been presented in Ref. [72] for the 7 and 8 TeV runs of the LHC. In Chapter 5 we reconsider the idea of Ref. [72] in light of the evidence for off-shell production found by recent measurements [73, 74] and show that the use of kinematic discriminants can significantly improve the projected limits on κ_q at the HL-LHC.

Chapter 2

The Muon Anomalous Magnetic Moment

In this chapter we will provide a brief review of the theoretical prediction for a_μ in the SM, analyzing the three contributions into which $a_\mu^{\rm SM}$ is usually split: QED, electroweak (EW) and hadronic, contributions. We will follow Refs. [5, 75]

2.1 The Standard Model Prediction of the Muon g-2

The determination of the SM prediction for the anomalous magnetic moment of the muon a_μ has captivated physicists for more than seventy years. While the agreement between the experimental results and the QED leading contribution for the anomalous magnetic moment of the electron a_e provided an early confirmation of this theory, a_e is relatively insensitive to strong and weak interactions, as well as unknown physics beyond the Standard Model (BSM), especially at higher energy scales. On the other hand, a_μ serves as a comprehensive test of the entire Standard Model and is much more effective in revealing or constraining the effects of "new physics". For a lepton ℓ, the contribution to a_ℓ is generally proportional to m_ℓ^2/Λ^2, where m_ℓ is the mass of the lepton and Λ the scale of "new physics", thus leading to an $(m_\mu/m_e)^2 \sim 4 \times 10^4$ relative enhancement of the sensitivity of the muon versus the electron anomalous magnetic moment. However, it might be worth noting that the situation is not as heavily skewed in favor of a_μ. Currently, the experimental precision of a_e, 1.3×10^{-13} [76], is approximately 2×10^3 times that of a_μ, 2.4×10^{-10}, resulting in a sensitivity difference of approximately 20. For the future, we expect an improvement of a factor of 10 in the sensitivity of a_e [77], and together with the results of the E989 experiment at Fermilab, this could potentially modify the sensitivity ratio between them.

2.1.1 The QED contribution to a_μ

The QED contribution to the anomalous magnetic moment of the muon arises from the subset of SM diagrams containing only the interaction between leptons (e, μ, τ) and pho-

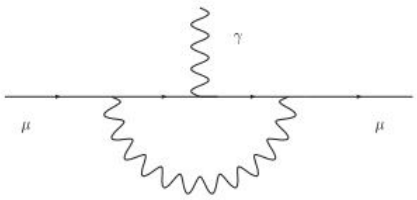

Figure 2.1: Lowest-order QED contribution to a_μ

tons. As a dimensionless quantity, it can be cast in the following general form

$$a_\mu^{\rm QED} = A_1 + A_2(m_\mu/m_e) + A_2(m_\mu/m_\tau) + A_3(m_\mu/m_e, m_\mu/m_\tau) \tag{2.1}$$

where m_e, m_μ and m_τ are the masses of the electron, muon and tau, respectively. The term A_1, arising from diagrams containing only photons and muons, is mass independent. In contrast, the terms A_2 and A_3 are functions of the indicated mass ratios, and are generated by graphs containing also electrons and taus. The renormalizability of QED guarantees that the functions $A_i (i = 1, 2, 3)$ can be expanded as power series in α/π and computed order-by-order

$$A_i = A_i^{(2)}\left(\frac{\alpha}{\pi}\right) + A_i^{(4)}\left(\frac{\alpha}{\pi}\right)^2 + A_i^{(6)}\left(\frac{\alpha}{\pi}\right)^3 + A_i^{(8)}\left(\frac{\alpha}{\pi}\right)^4 + A_i^{(10)}\left(\frac{\alpha}{\pi}\right)^5 + ... \tag{2.2}$$

By 2018, all terms up to the eighth order have been obtained and cross-checked by multiple groups using different methods [78]-[82]. However, the complete calculation of the tenth-order contribution has been carried out by only one group, employing numerical techniques [83]. In the following sections, we summarize all perturbative coefficients $A_i^{(2n)}$ up to the tenth order.

A. One-Loop contribution

The evaluation of the lowest-order contribution involves only one diagram, depicted in Fig. 2.1. This diagram is associated with the renowned result derived by Schwinger [84], $A_1^{(2)} = 1/2$ ($A_2^{(2)} = A_3^{(2)} = 0$).

B. Higher-order QED contributions

The fourth order QED corrections to a_μ are made up by nine diagrams depicted in Fig. 2.2. Among them seven contribute to $A_1^{(4)}$, they are obtained attaching two virtual photons to the muon lines and one is related to the insertion of a muon vacuum polarization. The remaining two diagrams contribute to $A_2^{(4)}(m_\mu/m_e)$ and $A_2^{(4)}(m_\mu/m_\tau)$, thanks to the insertion of an electron and a tau lepton vacuum polarization loop in the virtual photon line.

The analytic result for the coefficient $A_1^{(4)}$ has been known for more sixty years [85, 86]. The closed analytic expression of $A_2^{(4)}(x)$, for any mass ratio x, is also known [75] [87, 88].

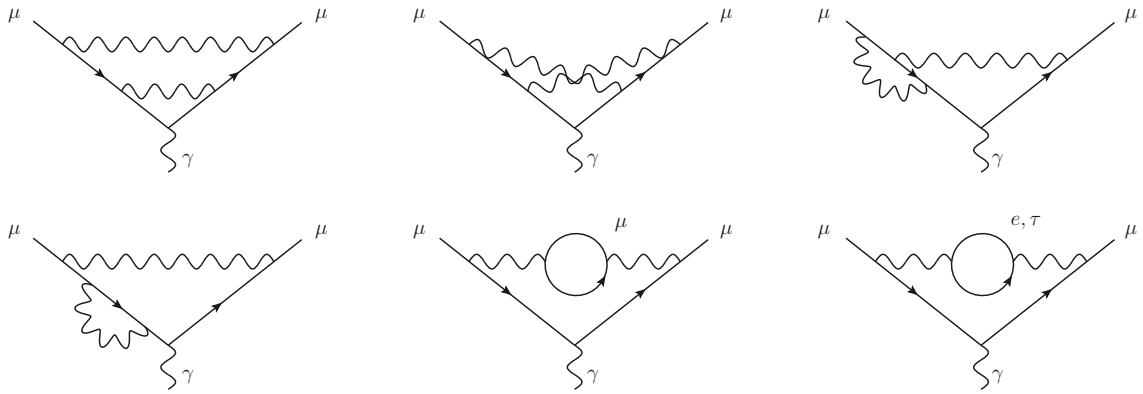

Figure 2.2: The QED diagrams contributing to the muon g-2 in order α^2. The mirror reflections (not shown) of the third and fourth diagrams must be included as well.

One gets [5]

$$\begin{aligned} A_1^{(4)} &= -0.328\ 478\ 965\ 579... \\ A_2^{(4)}(m_\mu/m_e) &= 1.094\ 258\ 3093\ (76) \\ A_2^{(4)}(m_\mu/m_\tau) &= 0.000\ 078\ 076\ (11), \end{aligned} \tag{2.3}$$

where the standard uncertainties are only caused by the experimental uncertainties of the lepton mass ratio. As there are no two-loop diagrams containing both virtual electrons and taus, $A_3^{(4)}(m_\mu/m_e, m_\mu/m_\tau) = 0$. Those diagrams arise for the first time at sixth-order.

Summing up all the results in Eq. (2.3), one gets the two-loop QED coefficient

$$C_2 = A_1^{(4)} + A_2^{(4)}(m_\mu/m_e) + A_2^{(4)}(m_\mu/m_\tau) = 0.765\ 857\ 419\ (13). \tag{2.4}$$

The uncertainties in $A_2^{(4)}(m_\mu/m_e)$ and $A_2^{(4)}(m_\mu/m_\tau)$ have been added in quadrature. The resulting error $\delta C_2 = 1.3 \times 10^{-8}$ leads to a tiny 0.05×10^{-12} uncertainty in a_μ^{QED}.

The evaluation of the three-loop (sixth-order) QED contribution involves more than one hundred diagrams. The coefficient $A_1^{(6)}$ arises from 72 diagrams, its calculation in closed analytic form has been achieved by [89, 90]. The result reads [5]

$$A_1^{(6)} = 1.181\ 241\ 4566... \tag{2.5}$$

The calculation of the exact expression for the coefficient $A_2^{(6)}(m/M)$, that for our analysis $m = m_\mu$ and $M = m_e$ or m_τ, can be further split into two parts: the first one receives contributions from 36 diagrams containing electron or τ vacuum polarization loops [91], meanwhile the second one is due to 12 light-by-light scattering diagrams with electron or τ loops [92]. The exact expression for $A_2^{(6)}(m/M)$ in closed analytic form is complicated as it contains hundreds of polylogarithmic functions up to fifth degree with complex arguments. The result is [5]:

$$\begin{aligned} A_2^{(6)}(m_\mu/m_e) &= 22.868\ 379\ 98\ (20), \\ A_2^{(6)}(m_\mu/m_\tau) &= 0.000\ 360\ 671\ (94). \end{aligned} \tag{2.6}$$

The analytic result, for the three-loop diagrams with both electron and τ loop insertion in the photon propagator, yields the numerical value [5]

$$A_3^{(6)}(m_\mu/m_e, m_\mu/m_\tau) = 0.000\ 527\ 738\ (75) \tag{2.7}$$

providing a small 0.7×10^{-11} contribution to $a_\mu^{\rm QED}$. The error is caused by the uncertainty of the ratio m_μ/m_τ. Combining the three-loop results presented above, one obtains the sixth-order QED coefficient

$$C_3 = A_1^{(6)} + A_2^{(6)}(m_\mu/m_e) + A_2^{(6)}(m_\mu/m_\tau) + A_3^{(6)}(m_\mu/m_e, m_\mu/m_\tau) = 24.050\ 509\ 94\ (23). \tag{2.8}$$

The error $\delta C_3 = 2.3 \times 10^{-7}$, due to the measurement uncertainties of the lepton masses, induces a negligible $O(10^{-14})$ uncertainty in $a_\mu^{\rm QED}$. In parallel to these analytic results, numerical methods were also developed for the evaluation of the full set of three-loop diagrams.

More than one thousand diagrams enter the evaluation of the four-loop QED contribution to a_μ. As only few of them are known analytically [93], this eighth-order term has thus far been evaluated only numerically in Ref. [78, 79]. Recently, the eighth-order mass-independent contribution $A_1^{(8)}$ has been calculated in analytical form by Laporta [80]. Since this eighth-order QED contribution is about six times larger than the present experimental uncertainty of a_μ, it is crucial for the comparison between the SM prediction of a_μ and its experimental determination. There are 891 four-loop diagrams contributing to the mass-independent coefficient, the updated result, obtained up to 1100 digits, is [80]

$$A_1^{(8)} = -1.912\ 245\ 764\ 926... \tag{2.9}$$

The latest value of the coefficient $A_2^{(8)}(m_\mu/m_e)$, arising from 469 diagrams, is [5]

$$A_2^{(8)}(m_\mu/m_e) = 132.6823\ (72). \tag{2.10}$$

The eighth-order τ-lepton contributions, $A_2^{(8)}(m_\mu/m_\tau)$ and $A_3^{(8)}(m_\mu/m_e, m_\mu/m_\tau)$, are also independently checked. This is done in two ways, first by numerical calculation [83] and second by use of asymptotic expansion [82],

$$\begin{aligned} A_2^{(8)}(m_\mu/m_\tau) &= 0.042\ 4941\ (53), \\ A_3^{(8)}(m_\mu/m_e, m_\mu/m_\tau) &= 0.062\ 722\ (10), \end{aligned} \tag{2.11}$$

which provide a small $O(10^{-12})$ contribution to $a_\mu^{\rm QED}$.

Summing up the four-loop results described above, we obtain the eighth-order QED coefficient

$$C_4 \simeq A_1^{(8)} + A_2^{(8)}(m_\mu/m_e) + A_2^{(8)}(m_\mu/m_\tau) + A_3^{(8)}(m_\mu/m_e, m_\mu/m_\tau) = 130.876\ 170\ (81). \tag{2.12}$$

At tenth order in QED there are more than ten thousand diagrams five-loop contributing to a_μ. The numerical results for the sum of all diagrams with one or more fermion

loops are given by [5]:

$$\begin{aligned} A_1^{(10)} &= 6.737\ (159), \\ A_2^{(10)}(m_\mu/m_e) &= 742.32\ (86), \\ A_2^{(10)}(m_\mu/m_\tau) &= -0.0656\ (45), \\ A_3^{(10)}(m_\mu/m_e, m_\mu/m_\tau) &= 2.011\ (10), \end{aligned} \tag{2.13}$$

where all the uncertainties are attributed entirely to the statistical fluctuation in the Monte-Carlo integration of Feynman amplitudes. Therefore, we obtain

$$C_5 \simeq A_1^{(10)} + A_2^{(10)}(m_\mu/m_e) + A_2^{(10)}(m_\mu/m_\tau) + A_3^{(10)}(m_\mu/m_e, m_\mu/m_\tau) = 751.0024\ (169). \tag{2.14}$$

C. The numerical value of $a_\mu^{\mathbf{QED}}$

Adding up all the above contributions and using the latest recommended value for the fine-structure constant, that comes from Cs atom-interferometry experiment [94],

$$\alpha^{-1} = 137.035\ 999\ 046\ (27), \tag{2.15}$$

the updated value for the QED contribution to the muon g-2 is [5]

$$a_\mu^{\mathrm{QED}} = 116\ 584\ 718.931\ (7)\ (17)\ (6)\ (100)\ (23)\ [104] \times 10^{-11}. \tag{2.16}$$

Where the uncertainties are due to τ-lepton mass m_τ, the eighth-order QED, the tenth-order QED, the estimate of the twelfth-order QED, the fine structure constant α, and the sum in quadrature of all of these.

2.1.2 The electroweak contribution

Contrary to the QED effects, the electroweak (EW) contribution to the anomalous magnetic moment of the muon is suppressed by a factor (m_μ^2/M_W^2). The one-loop part was computed in 1972 by several authors [95].

A. One-loop contribution

The one-loop EW contribution to a_μ is characterized by the analytic expression

$$a_\mu^{\mathrm{EW}(1)} = \frac{5G_F m_\mu^2}{24\sqrt{2}\pi^2}\Big[1 + \frac{1}{5}(1 - 4\sin^2\theta_w)^2 + O\Big(\frac{m_\mu^2}{M_{Z,W,H}^2}\Big)\Big], \tag{2.17}$$

where $G_F = 1.16637(1) \times 10^{-5}\ \mathrm{GeV}^{-2}$ is the Fermi coupling constant, M_Z, M_W and M_H are the masses of the Z, W and Higgs boson, and θ_w is the weak mixing angle. Taking into account the fact that the contribution of the Higgs boson to $a_\mu^{\mathrm{EW}(1)}$ is of order $O(10^{-14})$, it can be safely neglected, obtaining [5]

$$a_\mu^{\mathrm{EW}(1)} = 194.79\ (1) \times 10^{-11}. \tag{2.18}$$

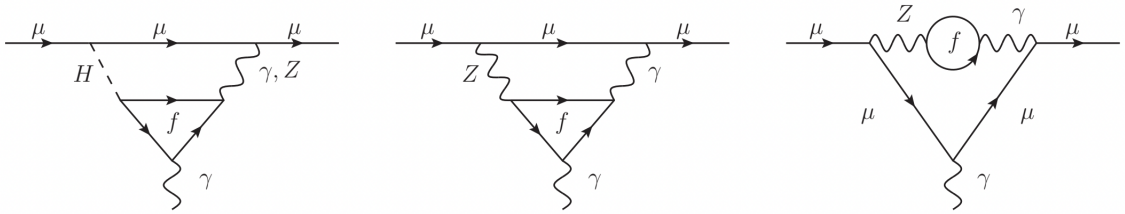

Figure 2.3: Sample fermionic two-loop Feynman diagrams contributing to $a_\mu^{EW(2)}$

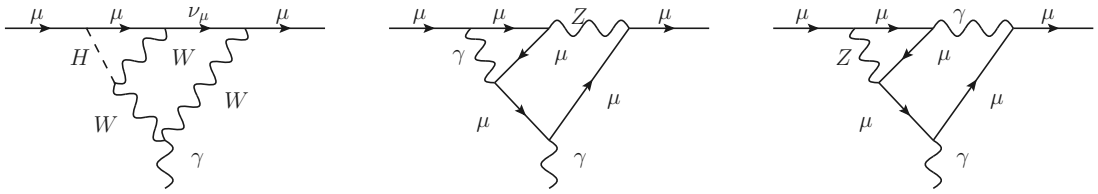

Figure 2.4: Sample bosonic two-loop Feynman diagrams contributing to $a_\mu^{EW(2)}$

B. Higher-order contributions

The two-loop EW contribution to a_μ was computed in 1995 by Czarnecki *et al* [96, 97]. Naively one would expect the two-loop EW contribution to be of order $(\alpha/\pi) \times a_\mu^{\mathrm{EW}(2)}$, and thus negligible, but this turns out not to be. In fact, $a_\mu^{\mathrm{EW}(2)}$ is quite substantial because of the appearance of terms enhanced by a factor of $\log(M_{Z,W}/m_f)$, where m_f is a fermion mass scale much smaller than M_W.

We can divide the two-loop contributions into fermionic and bosonic parts (Figs. 2.3 and 2.4 show examples of two-loop EW diagrams); the former includes all two-loop EW corrections containing closed fermion loops, whereas all others are grouped into the latter. The full two-loop calculation involves 1678 diagrams in the linear 't Hooft-Feynman gauge [98]. In particular, we can subdivide the fermionic two-loop contributions into:

$$a_\mu^{\mathrm{EW(2,\ fermionic)}} = a_\mu^{\mathrm{EW}(2)}(e,\mu,u,c,d,s) + a_\mu^{\mathrm{EW}(2)}(\tau,t,b) + a_{\mu,H}^{\mathrm{EW}(2)} + a_{\mu,rest}^{\mathrm{EW}(2)}\,. \tag{2.19}$$

The last two diagrams in Fig. 2.3 contain loops of the light quarks u, d, s. A perturbative evaluation produces large logarithms of light quark masses. Because of confinement, these quark masses are not well defined and significant non-perturbative corrections to these Feynman diagrams are expected. A non-perturbative evaluation of these diagrams, which can replace the perturbative result, has been pioneered in Ref. [99] and improved in Refs. [100, 101]. While, for the third generation fermions, one could proceed with a perturbative evaluation. Therefore, the first two terms of the RHS of (2.19) yields respectively [100]

$$\begin{aligned} a_\mu^{\mathrm{EW}(2)}(e,\mu,u,c,d,s) &= -6.91\ (20)\ (30) \times 10^{-11}, \\ a_\mu^{\mathrm{EW}(2)}(\tau,t,b) &= -8.21\ (10) \times 10^{-11}. \end{aligned} \tag{2.20}$$

The uncertainties are obtained by varying respective input parameters of the hadronic model and perturbative calculations. The hadronic uncertainties, above estimated to be

$\sim 2 \times 10^{-11}$, arise from two types of two-loop diagrams: hadronic photon-Z mixing, and quark triangle loops with the external photon, a virtual photon and a Z attached to them. The tiny hadronic $\gamma - Z$ mixing terms can be evaluated either in the free quarks approximation or via a dispersion relation using data from e^+e^- annihilation into hadrons.

The third term of (2.19) denotes the Higgs-dependent fermion loop diagrams, an exact expression can be found in [102]

$$a_{\mu,H}^{\mathrm{EW}(2)} = -1.51\ (1) \times 10^{-11}, \tag{2.21}$$

where the indicated uncertainty arises essentially from the uncertainty of the input parameters m_τ and M_H. The fourth term of (2.19) collects all remaining fermionic two-loop contributions, e.g. W boson exchange [102]

$$a_{\mu,rest}^{\mathrm{EW}(2)} = -4.64\ (10) \times 10^{-11}. \tag{2.22}$$

The bosonic two-loop contributions $a_\mu^{\mathrm{EW(2,\ boson)}}$ are defined by two-loop and associated counterterm diagrams without closed fermion loops, yielding [5, 103]

$$a_\mu^{\mathrm{EW(2,\ boson)}} = -19.96\ (1) \times 10^{-11}. \tag{2.23}$$

The given theory error is the parametric uncertainty resulting from the experimental uncertainty of the Higgs boson and W-boson masses, using the PDG value $M_H = 125.18(16)$ GeV [104].

Summing up the quoted results, one obtains [5]

$$a_\mu^{\mathrm{EW}} = 153.6\ (1) \times 10^{-11}. \tag{2.24}$$

There are very large logarithmically enhanced corrections to the one-loop result in Eq. (2.18). These arise from diagrams like the second and third ones in Fig. 2.3, Fig. 2.4, generally from two-loop diagrams that contain heavy particles and a photon. The resulting large logarithms $\log(M_z^2/m_f^2)$, where m_f is one of the light fermions, partially compensate the two-loop suppression. Numerically, these logarithmic two-loop effects reduce the one-loop result by approximately 20%.

2.1.3 The hadronic contribution

In this section we will analyze the contribution to the muon g-2 which originates from QED diagrams involving hadrons. Hadronic effects in two-loop EW contributions are already included in a_μ^{EW} in the previous section.

In particular, the most consistent hadronic effect is the $O(\alpha^2)$ hadronic vacuum polarization (HVP) insertion in the internal photon line of the one-loop muon vertex diagram.

A. Leading-order hadronic contribution

The leading hadronic contribution to the muon g-2 is due to the hadronic vacuum polarization insertion in the internal photon propagator of the one-loop diagram. The evaluation

of this $O(\alpha^2)$ diagram involves long-distance QCD for which perturbation theory cannot be employed. However, Bouchiat and Michael [105], using analyticity and unitarity, showed that this contribution can be computed from hadronic e^+e^- annihilation data via the dispersion integral [105]-[111] [1]

$$a_\mu^{\rm HLO} \equiv a_\mu^{\rm HVP}\,({\rm LO}) = \frac{1}{4\pi^3}\int_{s_0}^{\infty} ds\; K^{(2)}(s/m_\mu^2)\;\sigma^{(0)}(s) = \frac{\alpha^2}{3\pi^2}\int_{s_0}^{\infty}\frac{ds}{s}\;K^{(2)}(s/m_\mu^2)\;R(s), \tag{2.25}$$

where $s_0 = m_{\pi^0}^2$ is the squared neutral pion mass, $\sigma^{(0)}(s)$ is the experimental total cross section for e^+e^- annihilation into any hadronic state, with extraneous QED radiative corrections subtracted off, and $R(s)$ is the ratio of $\sigma^{(0)}(s)$ and the high-energy limit of the Born cross section for μ-pair production: $R(s) = \sigma^{(0)}(s)/(4\pi\alpha^2/3s)$. The kernel $K(s)$ is a well-known function

$$K^{(2)}(s/m_\mu^2) = \int_0^1 dx \frac{x^2(1-x)}{x^2 + (s/m_\mu^2)(1-x)}. \tag{2.26}$$

It decreases monotonically for increasing s, and for large s it behaves as $m_\mu^2/3s$ to a good approximation. For this reason the low-energy region of the dispersive integral is enhanced by $\sim 1/s^2$.

Therefore (2.25) offers an approach to overcome long-distance QCD issues appearing in the LO hadronic contribution to the a_μ calculation. Since it makes use of hadronic e^+e^- annihilation data, thus involving a positive squared momentum transfer, we will call it time-like approach.

Detailed evaluations of the dispersive integral (2.25) have been carried out by several authors. The hadronic contribution $a_\mu^{\rm HLO}$ is of order 7000×10^{-11} and, even if this is a small fraction of the total SM prediction for a_μ, it is very large compared to the current experimental uncertainty $\delta a_\mu^{\rm EXP} = 22 \times 10^{-11}$. Here we only focus on the most recent dispersive evaluation from the WP of the g-2 Theory Initiative [5],[6]-[13]

$$a_\mu^{\rm HLO} = 6931\;(40) \times 10^{-11}, \tag{2.27}$$

where the error is due to the experimental measurement of hadronic e^+e^- annihilation. In addition, a new preliminary measurement of $e^+e^- \to \pi^+\pi^-$ cross section from the CMD-3 experiment [26] disagrees significantly with all other e^+e^- data used in [5].

Alternatively, the LO HVP contribution to a_μ has been computed by BMW lattice QCD collaboration, finding a value larger than that in Eq. (2.27), 7075 (55) $\times 10^{-11}$ [25]. In particular, The BMWc's value for the window quantity, derived by incorporating weight functions into the Euclidean-time integral of the coordinate-space representation of HVP [17], exhibits a tension of 3.7σ with the cross-section data [27], and several lattice collaborations have now confirmed this result [28]-[31].

[1] Details of dispersion integrals will be treated in Chapter 3.

B. Higher-order hadronic contributions

We will now briefly discuss the higher order hadronic contribution to the muon g-2, $a_\mu^{\rm HHO}$, which can be divided into several parts:

$$a_\mu^{\rm HHO} = a_\mu^{\rm HVP}\,({\rm NLO}) + a_\mu^{\rm HVP}\,({\rm NNLO}) + a_\mu^{\rm Hlbl}\,({\rm LO}) + a_\mu^{\rm Hlbl}\,({\rm NLO})\,. \tag{2.28}$$

The first and second terms on the r.h.s. are the $O(\alpha^3)$ and $O(\alpha^4)$ contributions to a_μ of diagrams containing HVP insertion, while the third and the fourth terms are the hadronic light-by-light contributions at LO and NLO. The term $a_\mu^{\rm HVP}\,({\rm NLO})$ was computed in [112, 113]. In recent years it was re-evaluated by Keshavarzi *et al.* [12]

$$a_\mu^{\rm HVP}\,({\rm NLO}) = -98.3\;(7)\times 10^{-11}, \tag{2.29}$$

where the error is due to the experimental measure of hadronic e^+e^- annihilation data. The term $a_\mu^{\rm HVP}\,({\rm NNLO})$ was computed in [14]:

$$a_\mu^{\rm HVP}\,({\rm NNLO}) = 12.4\;(1)\times 10^{-11}. \tag{2.30}$$

The latest value for $a_\mu^{\rm Hlbl}\,({\rm LO})$ was reported in [5]

$$a_\mu^{\rm Hlbl}\,({\rm LO}) = +92\;(19)\times 10^{-11}. \tag{2.31}$$

The error is about 20% and it is completely dominated by the model estimates of a numerically subdominant part of the total. The NLO hadronic light-by-light contribution has been estimated to be [5, 114]:

$$a_\mu^{\rm Hlbl}\,({\rm NLO}) = 2\;(1)\times 10^{-11}. \tag{2.32}$$

2.2 The Standard Model prediction versus measurement

The WP 2020 Theory Initiative value for muon g-2 is:

$$a_\mu^{\rm SM} = a_\mu^{\rm QED} + a_\mu^{\rm EW} + a_\mu^{\rm HLO} + a_\mu^{\rm HHO} = 116\;591\;810\;(43)\times 10^{-11}. \tag{2.33}$$

The measurement of the anomalous magnetic moment of negative muons by the experiment E989 at Fermilab [1, 2] is

$$a_{\mu^-}^{\rm FNAL} = 116\;592\;055\;(24)\times 10^{-11}\quad (0.20{\rm ppm}). \tag{2.34}$$

The BNL E821 and Fermilab E989 experimental average is:

$$a_{\mu^-}^{\rm EXP} = 116\;592\;059\;(22)\times 10^{-11}\quad (0.19{\rm ppm}). \tag{2.35}$$

The comparison of the WP 2020 Theory Initiative value with the present experimental average gives the discrepancy

$$a_\mu^{\rm EXP} - a_\mu^{\rm SM} = 249\;(48)\times 10^{-11}, \tag{2.36}$$

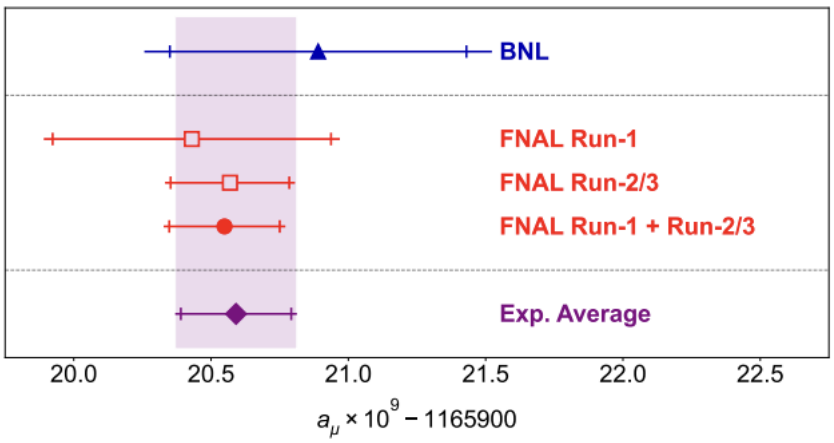

Figure 2.5: Experimental values of a_μ from BNL E821 [3], FNAL Run-1 result [1], Run-2 and Run-3 measurement [2], the combined Fermilab result, and the new experimental average. The inner tick marks indicate the statistical contribution to the total uncertainties. Figure taken from [2].

corresponding to a 5.1σ discrepancy. However, the BMW lattice QCD result for the LO HVP contribution to a_μ reduces this discrepancy to less than 2σ [25].

The E989 experiment is expected to reach a sensitivity four-times better than the earlier E821 experiment at Brookhaven [3]. In addition, a completely new low-energy approach to measuring the g-2 is being developed by the E34 collaboration at J-PARC [4].

Chapter 3

Hadronic Vacuum Polarization Contributions to the Muon g-2 in the Space-Like Region

In the pursuit of new physics, low-energy high-precision measurements serve as a valuable complement to the high-energy frontier of the LHC. Over the years, the persistent discrepancy between the experimental value of the muon anomalous magnetic moment and the prediction of the Standard Model (SM) has been regarded as one of the most intriguing indications of physics beyond the SM. However, the precision of the SM prediction, which stands at 43×10^{-11}, is hindered by the presence of strong interaction effects that cannot be reliably computed perturbatively at low energies. The persistent tension between the lattice results and dispersive ones makes the determination of the HVP contribution to a_μ through alternative methods desirable. This will be the topic for this Chapter.

In recent times, a novel experiment known as MUonE has been proposed at CERN with the objective of determining the leading-order hadronic contribution to the muon g-2. This experiment aims to measure the effective electromagnetic coupling in the space-like region through scattering data [32]-[34]. A comparison of experimental data with perturbative calculations can be used to extract the hadronic contribution to the running of the QED coupling α. The elastic scattering of high-energy muons on atomic electrons has been identified as an ideal process for carrying out this measurement. The effects of the HVP changes the differential cross section of μe scattering by up to $O(10^{-3})$, depending on the scattering angle of the outgoing electron. To achieve a determination of the HVP with a precision below one percent, it is imperative to measure the shape of the μe differential cross section with a systematic uncertainty of the order of 10 ppm or better. Consequently, an analogous level of precision is required in the theoretical prediction [32], [35]-[54].

The precision expected at the MUonE experiment also raised the question whether possible new physics (NP) could affect its measurement. The problem was addressed in [106], studying possible NP signals in muon-electron scattering at MUonE due to heavy or light mediators (depending on whether their mass is higher or lower than 1 GeV). The

former were analysed through an effective field theory approach in a model-independent way, while for the latter different scenarios with light spin-0 and spin-1 bosons were discussed. The authors showed that possible NP effects in muon-electron scattering are expected to lie below MUonE's sensitivity, hence concluding that it is very unlikely that NP contributions will contaminate MUonE's extraction of the HVP. Another research of NP signals at MUonE was dealt with in [107], where the authors addressed the sensitivity of the experiment to new light scalar or vector mediators, able to explain the muon g-2 discrepancy. They concluded that the measurement of the HVP at MUonE is not vulnerable to these NP scenarios. Therefore these two analysis reach similar conclusions where they overlap. These results confirm and reinforce the physics case of the MUonE experiment.

3.1 MUonE theoretical framework

In the previous chapter, we explored the computation of the leading-order (LO) hadronic contribution to the muon g-2 using dispersion relations and the optical theorem. This contribution is expressed by formula (2.25). It is important to note that $R(s)$ represents the ratio of the total cross section for e^+e^- annihilation into hadrons and the Born cross section for e^+e^- annihilation into $\mu^+\mu^-$. In the integrand of formula (2.25), this function exhibits significant fluctuations at low energies due to the presence of hadronic resonances and threshold effects. Typically, the dispersive integral in formula (2.25) is evaluated by utilizing the experimental measurement of $R(s)$ up to a certain value of s, combined with perturbative QCD in the high-energy region [108]. This approach is referred to as the time-like approach, but an alternative formula can also be exploited [32]. The optical theorem relates the $R(s)$ ratio with the imaginary part of the renormalized HVP function

$$R(s) = \frac{3}{\alpha}\mathrm{Im}\Pi_{\mathrm{h}}(s), \tag{3.1}$$

so that Eq. (2.25) can be written as

$$a_\mu^{\mathrm{HVP}}(\mathrm{LO}) = \frac{\alpha}{\pi^2}\int_{s_0}^{\infty}\frac{\mathrm{d}s}{s}\,K^{(2)}(s/m^2)\,\mathrm{Im}\Pi_{\mathrm{h}}(s). \tag{3.2}$$

Now, if we exchange the x and the s integration in the equation (3.2), we obtain

$$\begin{aligned} a_\mu^{\mathrm{HLO}} &= \frac{\alpha}{\pi}\int_0^1 dx\ (x-1)\Pi_{\mathrm{h}}[t(x)] \\ &= \frac{\alpha}{\pi}\int_0^1 dx\ (1-x)\Delta\alpha_{\mathrm{h}}[t(x)], \end{aligned} \tag{3.3}$$

where $\Delta\alpha_{\mathrm{h}}(t) = -\Pi_{\mathrm{h}}(t)$ is the hadronic contribution to the running of the fine-structure constant, evaluated at

$$t(x) = \frac{x^2 m_\mu^2}{x-1} < 0, \tag{3.4}$$

the space-like squared four-momentum transfer. In contrast with the integrand function of Eq. (2.25), the integrand in the Eq. (3.3) is smooth and free of resonances.

By measuring the running of α,

$$\alpha(t) = \frac{\alpha(0)}{1 - \Delta\alpha(t)}, \tag{3.5}$$

where $t = q^2 < 0$ and $\alpha(0) = \alpha$ is the fine-structure constant in the Thomson limit, the hadronic contribution $\Delta\alpha_{\rm h}(t)$ can be extracted by subtracting from $\Delta\alpha(t)$ the purely leptonic part $\Delta\alpha_\ell(t)$, which can be calculated order-by-order in perturbation theory. Recently, an alternative evaluation of the LO HVP contribution to a_μ at MUonE as been proposed in [115].

3.2 Kinematics of μe scattering

The MUonE experiment proposes to direct a 160 GeV muon beam towards a fixed target made of Beryllium or Carbon. To ensure an adequate number of events for statistical analysis and minimize the impact of multiple-scattering effects [109, 116], the target is divided into numerous thin layers. The experiment aims to achieve a high level of precision in measuring the scattering angles of the electrons θ_e and muons θ_μ in the laboratory frame.

From an idealised point of view we consider

$$\mu^\pm(p_1)e^-(p_2) \to \mu^\pm(p_3)e^-(p_4) + X \tag{3.6}$$

where the initial electron is at rest and X stands for any further radiation. Since the energy of the incoming muon is set to $E_1 = 160$ GeV, the center-of-mass energy is fixed as $s = m_e^2 + m_\mu^2 + 2m_e E_1 \simeq (400\ \text{MeV})^2$, where m_e and m_μ denote the electron and muon mass, respectively. The momentum transfer t ranges from $t_{min} \simeq -(391\ \text{MeV})^2$ to zero. Therefore, there are two widely different scales entering the process with $m_e^2 \ll Q^2$, where Q^2 stands for the large scales $m_\mu^2 \sim s \sim |t|$. The resulting large logarithms $\log(m_e^2/Q^2)$ will have to be properly accounted for the theoretical treatment of the process.

In a fixed-target experiment, where the electron is initially at rest, the Mandelstam variables s and t are given by

$$\begin{aligned} s &= m_\mu^2 + m_e^2 + 2m_e E_1, \\ t &= 2m_e^2 - 2m_e E_4, \\ t_{min} &= -\frac{\lambda(s, m_\mu^2, m_e^2)}{s} \le t \le 0. \end{aligned} \tag{3.7}$$

Here E_1 is the energy of the incident muon, E_4 is the electron recoil energy and

$$\lambda(a, b, c) = a^2 + b^2 + c^2 - 2ab - 2ac - 2bc \tag{3.8}$$

is the Källén function. The third Mandelstam variable u is related to s and t in the usual way as $s + t + u = 2m_\mu^2 + 2m_e^2$. It is also convenient to define the variable x that is related

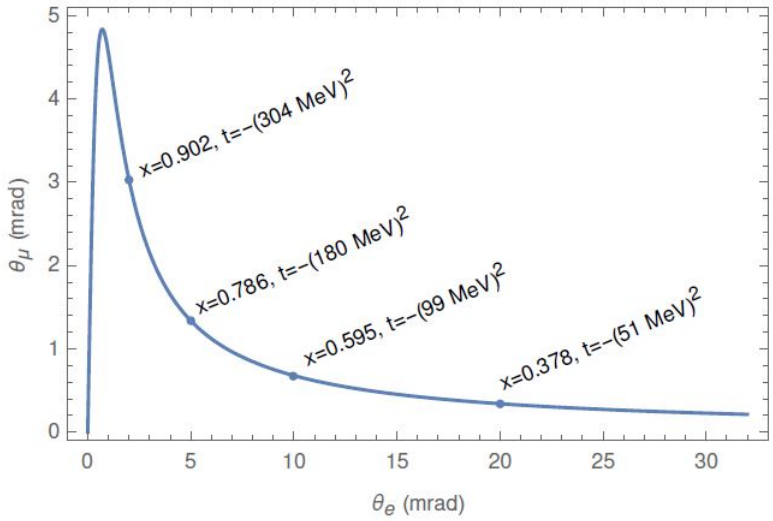

Figure 3.1: The elasticity curve, i.e. the relation between the muon and the electron scattering angles for 150 GeV incident muon beam momentum [40].

to t as

$$x(t) = \left(1 - \sqrt{1 - \frac{4m_\mu^2}{t}}\right)\frac{t}{2m_\mu}. \tag{3.9}$$

With $t_{min} \simeq -(391\ \text{MeV})^2$ the range of x is $0 \leq x \lesssim 0.936$ and $x = 0$ corresponds to $t = 0$. Given the incoming muon energy E_1, in a fixed target experiment the variable t is also related to the energy of the scattered electron E_4 or its angle θ_e:

$$E_4 = m\frac{1 + r^2 c_e^2}{1 - r^2 c_e^2}, \qquad \theta_e = \arccos\left(\frac{1}{r}\sqrt{\frac{E_4 - m_e}{E_4 + m_e}}\right), \tag{3.10}$$

where

$$r \equiv \frac{\sqrt{E_1^2 - m_\mu^2}}{E_1 + m_e}, \qquad c_e \equiv \cos\theta_e. \tag{3.11}$$

The angles of the scattered electron and muon are correlated as shown in Fig. 3.1. The mentioned constraint plays a crucial role in the selection of elastic scattering events, enabling the rejection of background events stemming from radiative or inelastic processes. It also serves to minimize systematic effects when determining the scattering variable, denoted as t. It is important to note that for scattering angles within the range of $(2 - 3)$ mrad, an ambiguity arises between the outgoing electron and muon due to their similar angles and momenta. This ambiguity can be resolved through the use of $\mu - e$ discrimination.

The MUonE experiment is expected to extract $\Delta\alpha_{\rm h}(t)$ from the shape of the differential μe scattering cross section by a template fit method [34]. The basic idea is that $\Delta\alpha_{\rm h}(t)$ can be obtained measuring, bin by bin, the ratio N_i/N_n, where N_i is the number of scattering events in a specific t-bin, labelled by the index i, and N_n is the number of events in the normalization t-bin corresponding to $x(t) \sim 0.3$ (for this value of x, $\Delta\alpha_{\rm h}(t)$ is comparable

to the experimental sensitivity expected at MUonE and its error is negligible). Therefore, this measurement will not rely on the absolute knowledge of the luminosity. To extract the leading hadronic correction to the μe scattering cross section in the t-bin i, one can split the theoretical prediction into

$$\sigma_{\text{th},i} = \sigma_i^{(0)}[1 + 2\Delta\alpha_{\text{h},i} + \delta_i + \delta_{\text{NP},i}], \tag{3.12}$$

where $\sigma_i^{(0)}$ is the LO QED prediction integrated in the t-bin i, $2\Delta\alpha_{\text{h},i}$ is the leading hadronic correction, δ_i is the reminder of the SM corrections, and $\delta_{\text{NP},i}$ is a possible NP contribution. The experimentally measured ratio N_i/N_n can then be equated with the ratio of the theoretical predictions,

$$\frac{N_i}{N_n} = \frac{\sigma_{\text{th},i}}{\sigma_{\text{th},n}} \simeq \frac{\sigma_i^{(0)}}{\sigma_n^0}[1 + 2(\Delta\alpha_{\text{h},i} - \Delta\alpha_{\text{h},n}) + (\delta_i - \delta_n) + (\delta_{\text{NP},i} - \delta_{\text{NP},n})]. \tag{3.13}$$

As $\Delta\alpha_{\text{h},n}$ is known with a negligible error, if $(\delta_i - \delta_n)$ is computed with sufficient precision, one can extract

$$2\Delta\alpha_{\text{h},i} + (\delta_{\text{NP},i} - \delta_{\text{NP},n}), \tag{3.14}$$

bin by bin, from N_i/N_n. Equation (3.13) shows that the impact of the SM corrections on this extractions can only be established after subtracting their value in the normalization region, and that, as we underlined before, the MUonE experiment will not be sensitive to a NP signal constant in t relative to the LO QED one, i.e. such that $\delta_{\text{NP},i} = \delta_{\text{NP},n}$ [106]. In any case, as already discussed, possible NP effects in muon-electron scattering are expected to lie below MUonE's sensitivity.

3.3 The HVP contribution at leading order

Following [46], we now present simple analytic expressions to compute the hadronic vacuum polarization contribution to the muon g-2 in the space-like region up to next-to-next-to-leading order. These results can be employed in lattice QCD calculations of this contribution as well as in space-like determinations based on scattering data, like that expected from the proposed MUonE experiment at CERN.

3.3.1 Time-like method

Consider the hadronic component of the vacuum polarization (VP) tensor with four-momentum q,

$$\begin{aligned} i\Pi_{\text{h}}^{\mu\nu}(q) &= i\Pi_{\text{h}}(q^2)\left(g^{\mu\nu}q^2 - q^\mu q^\nu\right) \\ &= \int \mathrm{d}^4x\, e^{iqx}\langle 0|T\left\{j_{\text{em}}^\mu(x) j_{\text{em}}^\nu(0)\right\}|0\rangle, \end{aligned} \tag{3.15}$$

where $j_{\text{em}}^\mu(x)$ is the electromagnetic hadronic current and $\Pi_{\text{h}}(q^2)$ is the renormalized hadronic vacuum polarization function satisfying the condition $\Pi_{\text{h}}(0) = 0$. The function $\Pi_{\text{h}}(q^2)$ cannot be computed using perturbation theory due to the non-perturbative

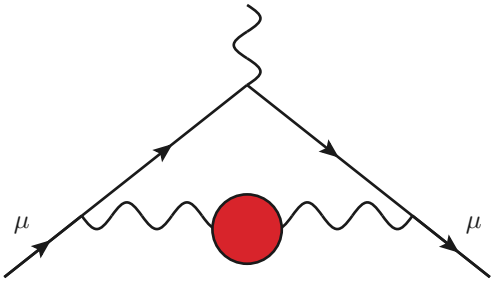

Figure 3.2: The leading, $O(\alpha^2)$, hadronic contribution to the muon g-2. The red blob indicates the HVP insertion.

behaviour of strong interactions at low energy. Yet, the optical theorem

$$\mathrm{Im}\Pi_{\mathrm{h}}(s) = (\alpha/3)R(s), \tag{3.16}$$

where α is the fine-structure constant and the R-ratio is

$$R(s) = \frac{\sigma(e^+e^- \to \text{hadrons})}{4\pi\alpha^2/(3s)} \tag{3.17}$$

allows to express the imaginary part of the hadronic vacuum polarization in terms of the measured cross section of the process $e^+e^- \to$ hadrons as a function of the positive squared four-momentum transfer s. This result forms the basis for the time-like method.

The LO hadronic contribution to the muon g-2, due to the $O(\alpha^2)$ diagram in Fig. 3.2, can be calculated integrating experimental time-like (i.e. $q^2 > 0$) data using the well-known formula [105]-[111]

$$a_\mu^{\mathrm{HVP}}(\mathrm{LO}) = \frac{\alpha}{\pi^2}\int_{s_0}^{\infty}\frac{\mathrm{d}s}{s}\,K^{(2)}(s/m^2)\,\mathrm{Im}\Pi_{\mathrm{h}}(s), \tag{3.18}$$

where m is the muon mass and $s_0 = m_{\pi^0}^2$ is the squared neutral pion mass. Defining

$$z = \frac{q^2}{m^2} \tag{3.19}$$

and the rationalizing variable

$$y(z) = \frac{z - \sqrt{z(z-4)}}{z + \sqrt{z(z-4)}}, \tag{3.20}$$

the second-order function $K^{(2)}(z)$ is

$$K^{(2)}(z) = \frac{1}{2} - z + \left(\frac{z^2}{2} - z\right)\ln z + \frac{\ln y(z)}{\sqrt{z(z-4)}}\left(z - 2z^2 + \frac{z^3}{2}\right). \tag{3.21}$$

For $z \geq 0$, $K^{(2)}(z)$ is real, positive and monotonic (it has no cut for $0 \leq z \leq 4$). At $z = 0$, $K^{(2)}(0) = 1/2$, while for $z \to +\infty$ the asymptotic behaviour of the kernel function is $K^{(2)}(z) \to 1/(3z)$, therefore vanishing at infinity.

3.3.2 Space-like method

The time-like expression for $a_\mu^{\rm HVP}({\rm LO})$ provided by (3.18) can be rewritten using the dispersion relation satisfied by $K^{(2)}(z)$ [117],

$$K^{(2)}(z) = \frac{1}{\pi}\int_{-\infty}^{0} {\rm d}z' \, \frac{{\rm Im}K^{(2)}(z')}{z'-z}, \quad z>0. \tag{3.22}$$

Indeed, replacing $K^{(2)}(s/m^2)$ in (3.18) with (3.22) and integrating over s via the subtracted dispersion relation satisfied by $\Pi_{\rm h}(q^2)$,

$$\frac{\Pi_{\rm h}(q^2)}{q^2} = \frac{1}{\pi}\int_{s_0}^{\infty} \frac{{\rm d}s}{s}\frac{{\rm Im}\Pi_{\rm h}(s)}{s-q^2}, \quad q^2<0, \tag{3.23}$$

we obtain the space-like expression

$$a_\mu^{\rm HVP}({\rm LO}) = -\frac{\alpha}{\pi^2}\int_{-\infty}^{0}\frac{{\rm d}t}{t}\,\Pi_{\rm h}(t)\,{\rm Im}K^{(2)}(t/m^2). \tag{3.24}$$

The function $K^{(2)}(z)$, real for any $z\geq 0$, has a cut along the negative real axis $z<0$ with the imaginary part

$$\begin{aligned}{\rm Im}K^{(2)}(z+i\epsilon) &= \pi\,\theta(-z)\left[\frac{z^2}{2}-z+\frac{z-2z^2+z^3/2}{\sqrt{z(z-4)}}\right]\\ &= \pi\,\theta(-z)\,F^{(2)}(1/y(z)),\end{aligned} \tag{3.25}$$

where

$$F^{(2)}(u) = \frac{u+1}{u-1}\,u^2. \tag{3.26}$$

The $i\epsilon$ prescription, with $\epsilon>0$, indicates that, in correspondence of the cut, the function ${\rm Im}K^{(2)}(z)$ is evaluated approaching the real axis from above.

If in Eq. (3.24) one uses the explicit expression for ${\rm Im}K^{(2)}(t/m^2)$ of Eq. (3.25) and changes the integration variable from t to $x=1+y$ via the substitution

$$t(x) = \frac{m^2x^2}{x-1}, \tag{3.27}$$

obtained from (3.20), one finds [118]

$$a_\mu^{\rm HVP}({\rm LO}) = \frac{\alpha}{\pi}\int_0^1 {\rm d}x\,\kappa^{(2)}(x)\,\Delta\alpha_{\rm h}(t(x)), \tag{3.28}$$

where the space-like kernel is remarkably simple,

$$\kappa^{(2)}(x) = 1-x \tag{3.29}$$

and $\Delta\alpha_{\rm h}(t) = -\Pi_{\rm h}(t)$ is the (five-flavor) hadronic contribution to the running of the effective fine-structure constant in the space-like region.

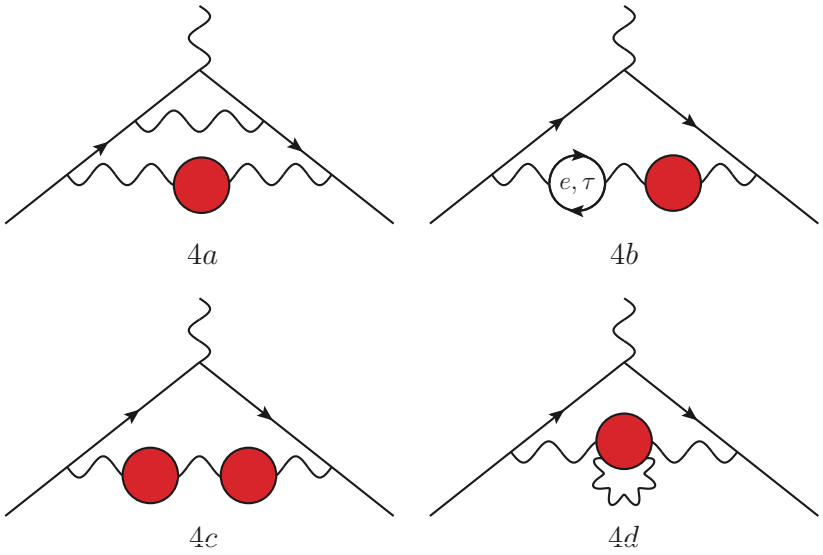

Figure 3.3: LO and sample NLO diagrams contributing to the HVP correction to the muon g-2.

Equation (3.28) (or forms equivalent to it) is used in lattice QCD calculations of $a_\mu^{\rm HVP}$(LO) (see e.g. [119] and a discussion in [5]). It also forms the basis for the MUonE proposal to determine $a_\mu^{\rm HVP}$(LO) via muon-electron scattering data [32]-[40], as we have seen in Section 3.1.

We note that, in Fig. 3.2 a virtual photon can be emitted and reabsorbed by the HVP insertion of the LO diagram. These represent irreducible hadronic contributions of higher order in α, that are normally incorporated into the time-like determinations of $a_\mu^{\rm HVP}$(LO) by including corrections for final-state radiation in the R-ratio (see e.g. [5, 6])[1]. For a meaningful comparison, space-like evaluations of $a_\mu^{\rm HVP}$(LO) should also incorporate these higher-order corrections. This can be accomplished by including them in the expression for $\Delta\alpha_{\rm h}(t)$ in Eq. (3.28). In this regard, the fully inclusive measurement of $\Delta\alpha_{\rm h}(t)$ from the MUonE experiment is particularly advantageous [39]. By incorporating these higher-order corrections, the MUonE experiment provides an ideal platform for obtaining a comprehensive understanding of the hadronic vacuum polarization contribution in the space-like region.

3.4 The HVP contribution at NLO

The hadronic vacuum polarization contribution to the muon g-2 at NLO, $a_\mu^{\rm HVP}$(NLO) has been studied as early as in Ref. [112]. This contribution arises from $O(\alpha^3)$ diagrams, which can be categorized as follows (see Fig. 3.3). Class ($4a$) comprises diagrams where a single HVP insertion appears in one of the photon lines of the two-loop QED diagrams

[1]Note that, consistently, the lower limit of integration in Eq. (3.18) has been chosen to be $s_0 = m_{\pi_0}^2$, the threshold of the $\pi_0\gamma$ cross section.

contributing to the muon g-2, without any VP insertion due to electron or tau loops[2]. Class $(4b)$ contains diagrams with one HVP and one additional VP due to an electron or tau loop. Class $(4c)$ consists of the single diagram with two HVPs. Class $(4d)$ diagrams contain internal radiative corrections to the HVP. As mentioned in the previous section, it is important to note that the contribution belonging to Class $(4d)$ is not considered as part of $a_\mu^{\rm HVP}(\rm NLO)$, even though of the same order in α, because it is already incorporated into $a_\mu^{\rm HVP}(\rm LO)$. Similarly, the contributions at $O(\alpha^4)$, which arise by adding a virtual photon emitted and reabsorbed by an HVP insertion to the diagrams of classes $(4a)$, $(4b)$, and $(4c)$, should be included in $a_\mu^{\rm HVP}(\rm NLO)$. Although these contributions are of higher order in α, they need to be accounted for either via the R-ratio method in the time-like approach or via $\Delta\alpha_{\rm h}(t)$ in the space-like approach. If a second virtual photon is attached to the HVP insertion of class $(4d)$, the resulting contribution should be incorporated into $a_\mu^{\rm HVP}(\rm LO)$ (See also Section 3.5).

Numerically, class $(4a)$ yields the largest (negative) contribution, class $(4b)$ partially cancels it, and the contribution of class $(4c)$ is small, as expected. Their sum

$$a_\mu^{\rm HVP}(\rm NLO) = a_\mu^{(4a)} + a_\mu^{(4b)} + a_\mu^{(4c)} \tag{3.30}$$

is negative and of the order $O(10^{-9})$.

3.4.1 Class $(4a)$

The NLO HVP contribution of class $(4a)$ to the muon g-2 can be written in the time-like form [117]

$$a_\mu^{(4a)} = \frac{\alpha^2}{\pi^3}\int_{s_0}^{\infty}\frac{{\rm d}s}{s}\,2K^{(4)}(s/m^2)\,{\rm Im}\Pi_{\rm h}(s). \tag{3.31}$$

The fourth-order function $K^{(4)}(z)$ was first computed by Barbieri and Remiddi in [117].[3] Its lengthy expression is reported in their Eq. (3.21) for $z > 0$, where it is real and negative. An approximate series expansion for $K^{(4)}(s/m^2)$ in the parameter m^2/s, with terms up to fourth order, can be found in [113]. Like $K^{(2)}(z)$, the function $K^{(4)}(z)$ is real for any $z \geq 0$, has a cut for $z < 0$, and satisfies the dispersion relation

$$K^{(4)}(z) = \frac{1}{\pi}\int_{-\infty}^{0}{\rm d}z'\,\frac{{\rm Im}K^{(4)}(z')}{z'-z}, \quad z > 0. \tag{3.32}$$

Just as we did for $a_\mu^{\rm HVP}(\rm LO)$, using the dispersion relations (3.23) and (3.32) the NLO hadronic contribution of class $(4a)$ can be cast in the space-like form

$$a_\mu^{(4a)} = -\frac{\alpha^2}{\pi^3}\int_{-\infty}^{0}\frac{{\rm d}t}{t}\,\Pi_{\rm h}(t)\,2{\rm Im}K^{(4)}(t/m^2). \tag{3.33}$$

[2]This class comprises also the contribution given by the diagram with one HVP and one additional VP due to muon loop in the same photon line

[3]Note the coefficient 2 in front of the function $K^{(4)}(z)$ due to the original normalization chosen in Ref. [117].

The function $\mathrm{Im}K^{(4)}(t/m^2)$ can be calculated from $K^{(4)}(z)$ expression of Ref. [117]. Taking the imaginary parts of the polylogarithms of order 1, 2, and 3, we obtain[4] [46]

$$\mathrm{Im}K^{(4)}(z+i\epsilon) = \pi\,\theta(-z)\,F^{(4)}(1/y(z)), \tag{3.34}$$

where

$$\begin{aligned} F^{(4)}(u) = {} & R_1(u) + R_2(u)\ln(-u) \\ & + R_3(u)\ln(1+u) + R_4(u)\ln(1-u) \\ & + R_5(u)\Big[4\mathrm{Li}_2(u) + 2\mathrm{Li}_2(-u) \\ & \quad + \ln(-u)\ln\Big((1-u)^2(1+u)\Big)\Big], \end{aligned} \tag{3.35}$$

and the rational functions $R_i(u)$ $(u = 1, \ldots, 5)$ are

$$\begin{aligned} R_1 = {} & \frac{23u^6-37u^5+124u^4-86u^3-57u^2+99u+78}{72(u-1)^2u(u+1)}, \\ R_2 = {} & \frac{12u^8-11u^7-78u^6+21u^5+4u^4-15u^3+13u+6}{12(u-1)^3u(u+1)^2}, \\ R_3 = {} & \frac{(u+1)\,(-u^3+7u^2+8u+6)}{12u^2}, \\ R_4 = {} & \frac{-7u^4-8u^3+8u+7}{12u^2}, \\ R_5 = {} & -\frac{3u^4+5u^3+7u^2+5u+3}{6u^2}. \end{aligned} \tag{3.36}$$

The dilogarithm is $\mathrm{Li}_2(u) = -\int_0^u (\mathrm{d}v/v)\ln(1-v)$.

Using the explicit expression for $\mathrm{Im}K^{(4)}(t/m^2)$ of (3.34), (3.33) can be conveniently expressed in terms of the variable $x = 1 + y$. We obtain

$$a_\mu^{(4a)} = \left(\frac{\alpha}{\pi}\right)^2 \int_0^1 \mathrm{d}x\,\kappa^{(4)}(x)\,\Delta\alpha_{\mathrm{h}}(t(x)), \tag{3.37}$$

where, for $0 \le x < 1$,

$$\kappa^{(4)}(x) = \frac{2-x}{x\,(x-1)}\,2F^{(4)}(x-1). \tag{3.38}$$

Equation (3.37) is the analogue of (3.28) for the NLO contribution of class $(4a)$.

Figure 3.4 shows the space-like functions $\kappa^{(2)}(x)$ and $\kappa^{(4)}(x)$ entering the $a_\mu^{\mathrm{HVP}}(\mathrm{LO})$ and $a_\mu^{(4a)}$ expressions, respectively. We note that the function $\kappa^{(4)}(x)$ provides a stronger weight to $\Delta\alpha_{\mathrm{h}}(q^2)$ at large negative values of q^2 than $\kappa^{(2)}(x)$. In particular, for $q^2 \to -\infty$, $\kappa^{(2)}(1) = 0$, whereas $\kappa^{(4)}(1) = -23/18$. Figure 3.5 shows the LO integrand $(\alpha/\pi)\kappa^{(2)}(x)\Delta\alpha_{\mathrm{h}}(t(x))$ of (3.28) and the NLO integrand $(\alpha/\pi)^2\kappa^{(4)}(x)\Delta\alpha_{\mathrm{h}}(t(x))$ of (3.37), multiplied by 10^7 and -10^8, respectively. The Fortran libraries KNT18VP [8], [108], [122]-[125] were used for the numerical implementation of $\Delta\alpha_{\mathrm{h}}(t(x))$ in the space-like region. The LO integrand has a peak at $x \sim 0.914$, where $t \sim -(0.33\mathrm{GeV})^2$. On the other hand, the NLO integrand of class $(4a)$ increases monotonically with $x \to 1$ (i.e. with $t \to -\infty$) like $\sim \ln(1-x)$.

[4] After presenting our $\mathrm{Im}K^{(4)}(z)$ result, Eqs. (3.34-3.36), in [120] (see also [121]), we were informed by Alexander Nesterenko that he has independently derived it in [45].

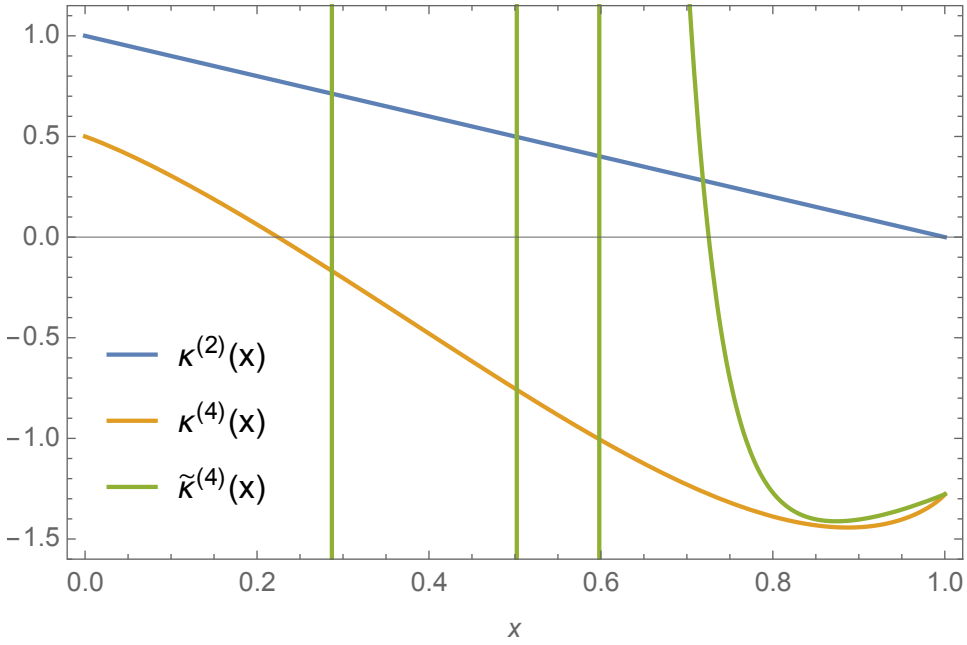

Figure 3.4: The space-like functions $\kappa^{(2)}(x)$ (blue), $\kappa^{(4)}(x)$ (orange) and $\tilde{\kappa}^{(4)}(x)$ (green). Figure taken from [46].

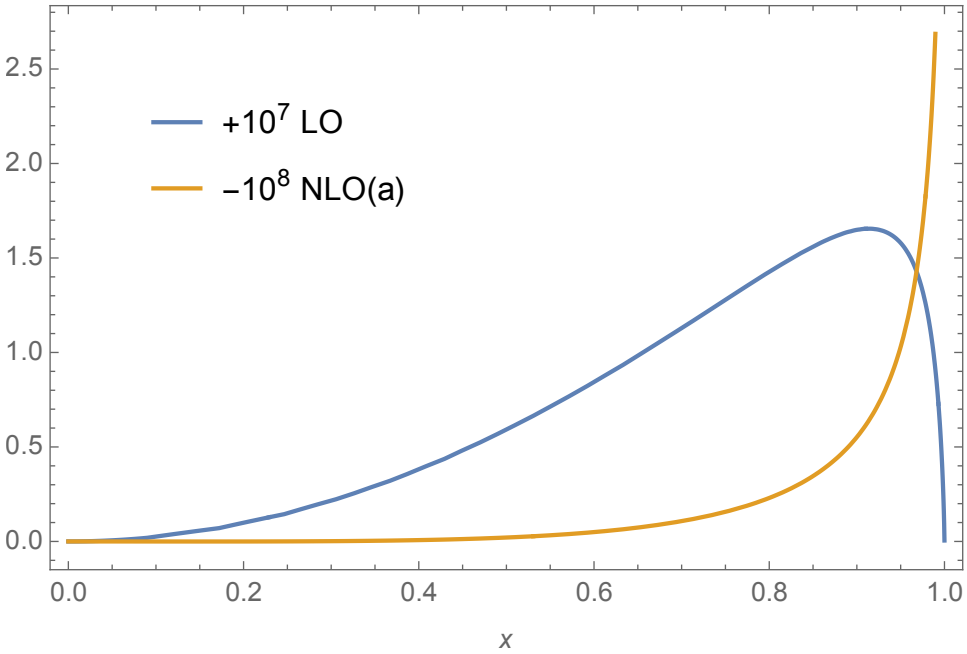

Figure 3.5: The integrands $(\alpha/\pi)\kappa^{(2)}(x)\Delta\alpha_{\rm h}(t(x))$ (blue) and $(\alpha/\pi)^2\kappa^{(4)}(x)\Delta\alpha_{\rm h}(t(x))$ (orange) of Eqs.(3.28) and (3.37), multiplied by 10^7 and -10^8, respectively. Figure taken from [46].

In Ref. [24], an approximate expression for the space-like formula in Eq. (3.37) was derived. The authors obtained this approximation by considering the fourth-order series expansion of the time-like function $K^{(4)}(s/m^2)$ from Ref. [113], which is valid for small values of the parameter $r = m^2/s$. This series expansion only contains powers r^n of degree $n = 1, 2, 3, 4$, multiplied by constants, $\ln r$, and $(\ln r)^2$ terms. Then, as suggested in [126], they exploited generating integral representations to fit the r^n and $r^n \ln r$ terms of the approximate fourth-order series expansion for $K^{(4)}(1/r)$, but not the $r^n(\ln r)^2$ ones, and used the usual dispersion relation satisfied by $\Pi_{\rm h}(q^2)$ to perform the integral over s. By making simple changes of variables, their approximation can be compared with our exact function $\kappa^{(4)}(x)$. We repeated the analysis of Ref. [24] confirming their approximate result (in particular, their Eqs. (A1,A2)) which, translated in our notation, will be called here $\tilde{\kappa}^{(4)}(x)$.

The approximate function $\tilde{\kappa}^{(4)}(x)$ is shown in Fig. 3.4 (indicated by the green line). While the exact function $\kappa^{(4)}(x)$ exhibits a smooth variation across the entire range of $0 \le x \le 1$, $\tilde{\kappa}^{(4)}(x)$ displays strong oscillations. This oscillatory behavior can lead to significant numerical cancellations when $\tilde{\kappa}^{(4)}(x)$ is used in the integral of Eq. (3.37) instead of the exact function $\kappa^{(4)}(x)$. Using the Fortran libraries KNT18VP [8], [108], [122]-[125] for the numerical implementation of $\Delta\alpha_{\rm h}(t(x))$ in the space-like region, we computed two numerical values for $a_\mu^{(4a)}$ in Eq. (3.37): one obtained using the exact function $\kappa^{(4)}(x)$ and a second one obtained replacing $\kappa^{(4)}(x)$ with the approximate $\tilde{\kappa}^{(4)}(x)$. The two values differ by about 3%. Adding to $a_\mu^{(4a)}$ the contributions $a_\mu^{(4b)}$ and $a_\mu^{(4c)}$ (discussed later), the total $a_\mu^{\rm HVP}({\rm NLO})$ contribution computed using the $\tilde{\kappa}^{(4)}(x)$ approximation differs from the one computed via our exact function $\kappa^{(4)}(x)$ by about 6%.

It is interesting to investigate the source of the above $\sim 6\%$ discrepancy. To improve the $\tilde{\kappa}^{(4)}(x)$ approximation, we proceeded in two directions. Firstly, we repeated the analysis of Ref. [24], starting however from higher-order series expansions for the exact $K^{(4)}(s/m^2)$ function of Barbieri and Remiddi [117] (we considered n up to $n_{\rm max} = 24$), rather than from the fourth-order (i.e. $n_{\rm max} = 4$) series expansion for $K^{(4)}(s/m^2)$ of Ref. [113]. Secondly, we improved the approximation by incorporating generating integral representations to fit not only the r^n and $r^n \ln r$ terms but also the $r^n(\ln r)^2$ terms, which were omitted in the previous analysis. The inclusion of these additional terms significantly improved the $\kappa^{(4)}(x)$ approximations, even without increasing the order $n_{\rm max}$ of the series expansion for $K^{(4)}(s/m^2)$ beyond four. Calling $\bar{\kappa}^{(4)}(x, n_{\rm max})$ our improved approximation to $\kappa^{(4)}(x)$, obtained including $r^n(\ln r)^2$ terms and starting from the series expansion for $K^{(4)}(s/m^2)$ up to order $n_{\rm max}$, we verified that the total $a_\mu^{\rm HVP}({\rm NLO})$ contribution computed using our $\bar{\kappa}^{(4)}(x, 4)$ differs by less than one per mille from the one computed via our exact function $\kappa^{(4)}(x)$. Even better agreements were reached increasing the order $n_{\rm max}$.

In Ref. [24], the authors added an $O(10\%)$ uncertainty to their final result to account for the error arising from neglecting the $r^n(\ln r)^2$ terms in their approximation. This uncertainty, which dominates the error of their final result, can be eliminated using the exact formula for $\kappa^{(4)}(x)$ provided above.

3.4.2 Classes (4*b*) and (4*c*)

The space-like expressions for the contributions of classes (4*b*) and (4*c*) to the muon g-2 are [6, 24]

$$a_\mu^{(4b)} = \frac{\alpha}{\pi}\int_0^1 \mathrm{d}x\,\kappa^{(2)}(x)\,\Delta\alpha_{\rm h}(t(x)) \times 2\left[\Delta\alpha_e^{(2)}(t(x)) + \Delta\alpha_\tau^{(2)}(t(x))\right], \tag{3.39}$$

$$a_\mu^{(4c)} = \frac{\alpha}{\pi}\int_0^1 \mathrm{d}x\,\kappa^{(2)}(x)\,\left[\Delta\alpha_{\rm h}(t(x))\right]^2, \tag{3.40}$$

where $\Pi_\ell^{(2)}(t) = -\Delta\alpha_\ell^{(2)}(t)$ is the renormalized one-loop QED vacuum polarization function in the space-like region, with a lepton $\ell = e, \tau$ in the loop,

$$\Pi_\ell^{(2)}(t) = \frac{\alpha}{\pi}\left[\frac{8}{9} - \frac{\beta_\ell^2}{3} + \beta_\ell\left(\frac{1}{2} - \frac{\beta_\ell^2}{6}\right)\ln\frac{\beta_\ell - 1}{\beta_\ell + 1}\right] \tag{3.41}$$

and $\beta_\ell = \sqrt{1 - 4m_\ell^2/t}$. Equations (3.39,3.40) can be immediately obtained from the time-like formulae of Ref. [113] using the usual dispersion relation satisfied by $\Pi_{\rm h}(t)$ and $\Pi_\ell^{(2)}(t)$ to perform the integrals over s [24, 118].

Figure 3.6 shows the NLO integrands of Eqs. (3.37), (3.39), and (3.40), multiplied by -10^8, 10^8, and 10^8, respectively. Once again, the Fortran libraries KNT18VP [8], [108], [122]-[125] were used for $\Delta\alpha_{\rm h}(t(x))$.

3.5 The HVP contribution at NNLO

The hadronic vacuum polarization contribution to the muon g-2 at NNLO, $a_\mu^{\rm HVP}$(NNLO), is due to several diagrams of order $\mathcal{O}(\alpha^4)$. We divide them into following classes (see Fig. 3.7)[5]: class (6*a*) contains diagrams with one HVP insertion and up to two photons added to the LO QED Feynman graph; it also includes diagrams with one or two muon VP loops and the light-by-light graph with a muon loop. Class (6*b*) comprises diagrams with one HVP insertion and one or two electron VP loops and additional photonic or muon VP corrections; it also includes diagrams with one electron VP loop with an HVP insertion inside it. Class (6*bll*) diagrams have one HVP insertion and light-by-light graphs with an electron loop; in these diagrams, the external photon couples to the electron. Class (6*c*) contains diagrams with two HVP insertions and additional photonic corrections and/or electron or muon VP loops. Class (6*d*) consists of the diagram with three HVP insertions. All of these classes were studied in Ref. [14] in the time-like approach.

Class (6*e*) diagrams are obtained by adding to those of classes (4*a*), (4*b*) and (4*c*) a virtual photon emitted and reabsorbed by an HVP insertion. As discussed in the previous section, their contribution should not be considered as part of $a_\mu^{\rm HVP}$(NNLO), although of the same order in α, because it is already incorporated into $a_\mu^{\rm HVP}$(NLO) via the R-ratio

[5] At NNLO we neglect the contribution of tau loops as it is estimated to be smaller than $O(10^{-12})$ [14]

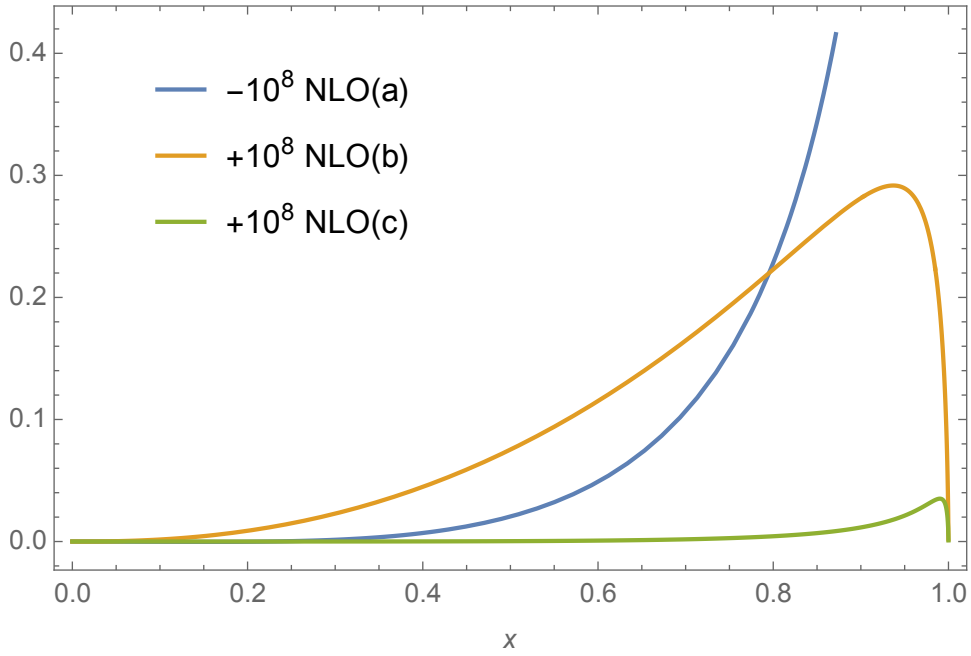

Figure 3.6: The NLO integrands of Eqs. (3.37) (blue), (3.39) (orange), and (3.40) (green), multiplied by -10^8, 10^8, and 10^8, respectively. Figure taken from [46].

(in the time-like approach) or via $\Delta\alpha_{\rm h}(t)$ (in the space-like one). The impact of class $(6e)$ can be roughly estimated considering the corresponding class of diagrams where the HVP insertion is replaced by a muon VP; that four-loop QED contribution to the muon g-2 is -1.63×10^{-12} [80]. The effect of class $(6e)$ can thus be estimated to be of $O(10^{-12})$. Similarly, the corrections of class $(6f)$, where two photons are emitted and reabsorbed by the HVP insertion of the LO diagram, should be already included in $a_\mu^{\rm HVP}({\rm LO})$. Once again, this contribution can be estimated replacing the HVP insertion by a muon VP: 1.44×10^{-12} [80]. Also the effect of class $(6f)$ can thus be estimated to be of $O(10^{-12})$. The contribution of class $(6g1)$ was recently studied in Ref. [127], where it was estimated to be $\lesssim 1 \times 10^{-11}$. The impact of classes $(6g2)$ and $(6h)$ can be estimated, once more, via the four-loop QED contribution obtained replacing the HVPs by muon VPs: 3.24×10^{-13} [80]. Classes $(6f)$, $(6g1)$, $(6g2)$ and $(6h)$ should be incorporated into $a_\mu^{\rm HVP}({\rm LO})$.

The sum of the NNLO contributions is, therefore,

$$a_\mu^{\rm HVP}({\rm NNLO}) = a_\mu^{(6a)} + a_\mu^{(6b)} + a_\mu^{(6bll)} + a_\mu^{(6c)} + a_\mu^{(6d)}. \tag{3.42}$$

It is positive and of $\mathcal{O}(10^{-10})$ [14].

3.5.1 Class $(6a)$

The contribution of class $(6a)$ can be written in the time-like form [14]

$$a_\mu^{(6a)} = \frac{\alpha^3}{\pi^4} \int_{s_0}^{\infty} \frac{{\rm d}s}{s}\, K^{(6a)}(s/m^2)\, {\rm Im}\Pi_{\rm h}(s). \tag{3.43}$$

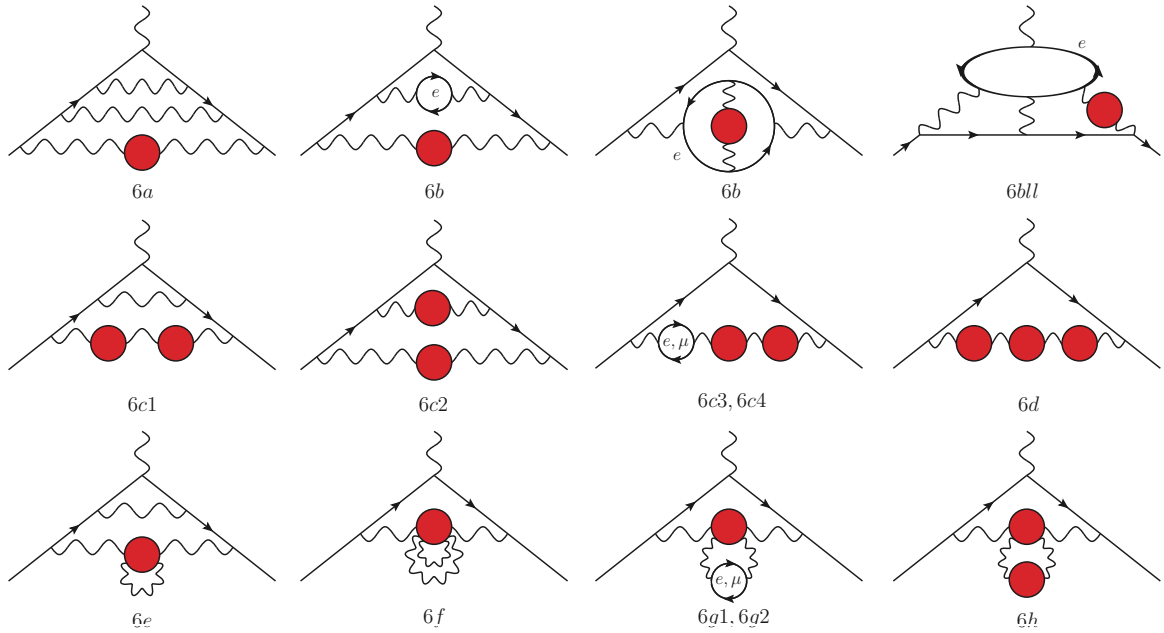

Figure 3.7: Sample $\mathcal{O}(\alpha^4)$ diagrams contributing to the HVP correction to the muon g-2.

In the study presented in [14], an approximated series expansion of the sixth-order function $K^{(6a)}(z)$ in terms of the parameter $r = m^2/s$ was computed. This expansion includes terms up to fourth order, involving powers r^n with $n = 1, 2, 3, 4$, multiplied by constants, $\ln r$, $(\ln r)^2$ and $(\ln r)^3$ terms. Following a procedure similar to that described at NLO, we exploited generating integral representations to fit all the r^n, $r^n \ln r$, $r^n (\ln r)^2$, and $r^n (\ln r)^3$ terms of the $K^{(6a)}(s/m^2)$ expansion,

$$K^{(6a)}\left(s/m^2\right) = r \int_0^1 \mathrm{d}\xi \left[\frac{L^{(6a)}(\xi)}{\xi + r} + \frac{P^{(6a)}(\xi)}{1 + r\xi} \right] \tag{3.44}$$

where

$$L^{(6a)}(\xi) = G^{(6a)}(\xi) + H^{(6a)}(\xi) \ln \xi + J^{(6a)}(\xi) \ln^2 \xi \tag{3.45}$$

and

$$G^{(6a)}(\xi) = g_0^{(6a)} + g_1^{(6a)} \xi + g_2^{(6a)} \xi^2 + g_3^{(6a)} \xi^3, \tag{3.46}$$
$$H^{(6a)}(\xi) = h_0^{(6a)} + h_1^{(6a)} \xi + h_2^{(6a)} \xi^2 + h_3^{(6a)} \xi^3, \tag{3.47}$$
$$J^{(6a)}(\xi) = j_0^{(6a)} + j_1^{(6a)} \xi + j_2^{(6a)} \xi^2 + j_3^{(6a)} \xi^3, \tag{3.48}$$
$$P^{(6a)}(\xi) = p_0^{(6a)} + p_1^{(6a)} \xi + p_2^{(6a)} \xi^2 + p_3^{(6a)} \xi^3, \tag{3.49}$$

Obtaining the coefficients $g_i^{(6a)}$,$h_i^{(6a)}$, $j_i^{(6a)}$ and $p_i^{(6a)}$ $(i = 0, 1, 2, 3)$ are reported in Table A.1 (from [46]) in Appendix A.

Inserting the integral representation of Eq. (3.44) in Eq. (3.43) and using the dispersion relation satisfied by $\Pi_{\rm h}(q^2)$, one can perform the integral over s. With simple changes of variables we obtain [46]

$$a_\mu^{(6a)} = \left(\frac{\alpha}{\pi}\right)^3 \int_0^1 \mathrm{d}x\, \bar{\kappa}^{(6a)}(x)\, \Delta\alpha_{\rm h}(t(x)), \tag{3.50}$$

where, for $0 < x < x_\mu = (\sqrt{5}-1)/2 = 0.618...$,

$$\bar{\kappa}^{(6a)}(x) = \frac{2-x}{x\,(1-x)}\, P^{(6a)}\!\left(\frac{x^2}{1-x}\right), \tag{3.51}$$

whereas, for $x_\mu < x < 1$,

$$\bar{\kappa}^{(6a)}(x) = \frac{2-x}{x^3} L^{(6a)}\left(\frac{1-x}{x^2}\right). \tag{3.52}$$

We note that for $x = x_\mu$, $t = -m^2$. The uncertainty of Eq. (3.50) due to the series approximation of $K^{(6a)}$ is estimated to be less than $O(10^{-12})$.

3.5.2 Classes (6*b*) and (6*bll*)

The contributions of classes (6b) and (6bll) can be calculated using a similar approach as class (6a). Indeed, in the time-like region, $a_\mu^{(6b)}$ and $a_\mu^{(6bll)}$ can be computed via Eq. (3.43) replacing $K^{(6a)}$ with $K^{(6b)}$ and $K^{(6bll)}$, respectively. For these sixth-order kernel functions, approximate series expansions in the parameters $r = m^2/s$ and $\rho = m_e/m$ were computed in [14]. The highest order expansion terms provided are of $O(\rho^2 r^4)$. By following a similar procedure as described in Subsection 3.5.1, the expansions were fitted to obtain integral representations analogous to that of Eq. (3.44) with the coefficients $g_i^{(6b)}$, $h_i^{(6b)}$, $j_i^{(6b)}$, $p_i^{(6b)}$ and $g_i^{(6bll)}$, $h_i^{(6bll)}$, $j_i^{(6bll)}$, $p_i^{(6bll)}$ reported in Table A.2 and A.3, respectively (from [46]). Using these integral representations, the contributions $a_\mu^{(6b)}$ and $a_\mu^{(6bll)}$ can be calculated in the space-like region, following the equations (3.50)-(3.52) with appropriate modifications already given above. The estimated uncertainties of these contributions, due to the series approximations, are reported to be less than $O(10^{-12})$.

3.5.3 Class (6*c*)

The contribution of class (6c) in the time-like region is given by [14]

$$a_\mu^{(6c)} = \frac{\alpha^2}{\pi^4} \int_{s_0}^\infty \frac{\mathrm{d}s}{s} \frac{\mathrm{d}s'}{s'} K^{(6c)}\left(s/m^2, s'/m^2\right)\ \mathrm{Im}\,\Pi_{\rm h}(s)\,\mathrm{Im}\,\Pi_{\rm h}\left(s'\right). \tag{3.53}$$

In the case of class (6c) diagrams, which involve two HVP insertions, the time-like formula (3.53) for $a_\mu^{(6c)}$ requires two dispersive integrations of $\mathrm{Im}\,\Pi_{\rm h}(s)$. In Ref. [14], asymptotic expansions were provided for the function $K^{(6c)}\left(s/m^2, s'/m^2\right)$ in the limits $s' \approx s \gg m^2$ and $s' \gg s \gg m^2$. These expansions allow for an approximation of $K^{(6c)}\left(s/m^2, s'/m^2\right)$ that is valid for all values of s' and s that are much larger than m^2.

In the time-like approach, the number of dispersive integrations of $\mathrm{Im}\,\Pi_{\rm h}(s)$ needed to calculate the contribution of a diagram to the muon g-2 is determined by the number of HVP insertions in the diagram. On the other hand, the required dimension of the space-like integral of $\Delta\alpha_{\rm h}(t)$ (or powers of it) equals the number of photon lines with different momenta containing HVP insertions. To obtain a space-like formula for $a_\mu^{(6c)}$, it is therefore convenient to separate the diagrams of class $(6c)$ into the following four sub-classes $(6c1)$, $(6c2)$, $(6c3)$, and $(6c4)$ (see Fig. 3.7).

The diagrams of subclass $(6c1)$ contain two HVP insertions in the same photon line and no other electron or muon loop. The exact space-like expression for their contribution to the muon g-2 is therefore given by the one-dimensional integral [46]

$$a_\mu^{(6c1)} = \left(\frac{\alpha}{\pi}\right)^2 \int_0^1 \mathrm{d}x \lambda^{(4)}(x) \left[\Delta\alpha_{\rm h}(t(x))\right]^2 \tag{3.54}$$

where the kernel function is

$$\lambda^{(4)}(x) = \kappa^{(4)}(x) - \frac{2\pi}{\alpha}\kappa^{(2)}(x)\Delta\alpha_\mu^{(2)}(t(x)) \tag{3.55}$$

$\kappa^{(4)}(x)$ is the exact fourth-order space-like kernel of Eq. (3.38) and $\kappa^{(2)}(x)$ is the lowest-order one of Eq. (3.29). In Eq. (3.54), the use of the subtracted kernel $\lambda^{(4)}(x)$ instead of $\kappa^{(4)}(x)$ guarantees the subtraction of the contribution, induced by $\kappa^{(4)}(x)$, of two diagrams containing two HVP and one muon VP in the same photon line.

The contribution of the three diagrams of subclass $(6c3)$, containing two HVP and one electron VP insertion in the same photon line, can be cast in the exact space-like one-dimensional integral form [46]

$$a_\mu^{(6c3)} = \frac{3\alpha}{\pi} \int_0^1 \mathrm{d}x\ \kappa^{(2)}(x) \left[\Delta\alpha_{\rm h}(t(x))\right]^2 \Delta\alpha_e^{(2)}(t(x)). \tag{3.56}$$

Analogously, the exact contribution of subclass $(6c4)$, comprising three diagrams with two HVP and one muon VP insertion in the same photon, can be simply obtained replacing $\Delta\alpha_e^{(2)}(t)$ with $\Delta\alpha_\mu^{(2)}(t)$ in Eq. (3.56).

Subclass $(6c2)$ includes diagrams with two HVP insertions in two different photon lines. Unlike the simple one-dimensional integral form seen in the previous expressions for the contributions to the muon g-2, the presence of two different photon lines with HVP insertions in $(6c2)$ necessitates a double space-like integration. In [46] we therefore proceeded in two steps. First, we computed the approximate time-like kernel $K^{(6c2)}\left(s/m^2, s'/m^2\right)$ for the subclass $(6c2)$. This was obtained by calculating the exact time-like kernels $K^{(6c1)}\left(s/m^2, s'/m^2\right)$, $K^{(6c3)}\left(s/m^2, s'/m^2\right)$ and $K^{(6c4)}\left(s/m^2, s'/m^2\right)$ from the exact space-like expressions of Eqs. (3.54, 3.56), computing the series expansion of these kernels in the limits $s' \approx s \gg m^2$ and $s' \gg s \gg m^2$. The obtained results from these series expansions were then subtracted from the $K^{(6c)}\left(s/m^2, s'/m^2\right)$ approximation available in Ref. [14]. In the second step, we performed a matching process where we compared the LO terms of the approximate time-like kernel $K^{(6c2)}\left(s/m^2, s'/m^2\right)$ with those obtained from a series expansion of a two-dimensional generating integral representation, generalising to two-dimensions the method used earlier to fit the $K^{(6a)}\left(s/m^2\right)$ expansion.

Our result for the space-like expression of the contribution of subclass $(6c2)$ to the muon g-2 is [46]

$$a_\mu^{(6c2)} = \left(\frac{\alpha}{\pi}\right)^2 \int_{x_\mu}^1 \mathrm{d}x \int_{x_\mu}^1 \mathrm{d}x' \; \bar{\kappa}^{(6c2)}\left(x,x'\right) \Delta\alpha_{\mathrm{h}}(t(x)) \Delta\alpha_{\mathrm{h}}\left(t\left(x'\right)\right), \tag{3.57}$$

where for $x_\mu < \{x, x'\} < 1$,

$$\bar{\kappa}^{(6c2)}\left(x,x'\right) = \frac{2-x}{x^3}\frac{2-x'}{x'^3} G^{(6c2)}\left(\frac{1-x}{x^2}, \frac{1-x'}{x'^2}\right) \tag{3.58}$$

and

$$\begin{aligned} G^{(6c2)}\left(\xi,\xi'\right) = {} & \frac{1}{4\left(32\pi^2-315\right)} \times \\ & \times \left[\left(1855-188\pi^2\right)\frac{\min\left(\xi,\xi'\right)}{\max\left(\xi,\xi'\right)^2} + \right. \\ & + \left(988\pi^2-9765\right)\frac{\min\left(\xi,\xi'\right)^2}{\max\left(\xi,\xi'\right)^3} + \\ & \left. +24\left(435-44\pi^2\right)\frac{\min\left(\xi,\xi'\right)^3}{\max\left(\xi,\xi'\right)^4}\right]. \end{aligned} \tag{3.59}$$

This contribution is of $O(10^{-12})$. We note that the limits of integration in Eq. (3.57) are x_μ and 1, corresponding to values of t between $-m^2$ and $-\infty$, respectively.

Equation (3.57) completes the list of space-like expressions for the contributions of class $(6c)$,

$$a_\mu^{(6c)} = a_\mu^{(6c1)} + a_\mu^{(6c2)} + a_\mu^{(6c3)} + a_\mu^{(6c4)}. \tag{3.60}$$

The uncertainty of Eq. (3.60) due to the approximations of subclass $(6c2)$ is less than $O(10^{-12})$.

3.5.4 Class $(6d)$

The correction due to the single diagram of class $(6d)$ can be written in the time-like form [14]

$$a_\mu^{(6d)} = \frac{\alpha}{\pi^4}\int_{s_0}^\infty \frac{\mathrm{d}s}{s}\frac{\mathrm{d}s'}{s'}\frac{\mathrm{d}s''}{s''} K^{(6d)}\left(s,s',s''\right) \mathrm{Im}\,\Pi_{\mathrm{h}}(s)\,\mathrm{Im}\,\Pi_{\mathrm{h}}\left(s'\right)\mathrm{Im}\,\Pi_{\mathrm{h}}\left(s''\right). \tag{3.61}$$

The kernel $K^{(6d)}\left(s,s',s''\right)$ for the triple hadronic insertion is given in integral form in [14]. On the other hand, the space-like expression for $a_\mu^{(6d)}$ can be expressed in a simple exact form, as provided in Ref. [6].

$$a_\mu^{(6d)} = \frac{\alpha}{\pi}\int_0^1 \mathrm{d}x \; \kappa^{(2)}(x)\left[\Delta\alpha_{\mathrm{h}}(t(x))\right]^3. \tag{3.62}$$

It is worth noting that to compute $a_\mu^{(6d)}$ in the time-like approach, three dispersive integrations of $\mathrm{Im}\,\Pi_{\mathrm{h}}\left(s\right)$ are required, while in the space-like approach, as given in Eq. (3.62), only a one-dimensional integral is involved. Numerically, $a_\mu^{(6d)}$ is very small, of $O(10^{-13})$.

Chapter 4

Time-kernel for Lattice Determinations of Computing Hadronic Vacuum Polarization Contributions to the Muon g-2

In this Chapter, following [128], we present approximations for the euclidean-time kernels obtained from the HVP contributions to the muon g-2 in the space-like region up to next-to-leading order. The series expansions presented overcome the problems given by their asymptotic behaviour for large value of the time. These results can be employed in lattice QCD determination of the HVP contribution to the muon g-2 up to NLO.

4.1 The time-kernel at LO

In the so-called time-momentum representation (TMR) discussed in [129]-[131] the subtracted hadronic vacuum polarization function $\hat{\Pi}_{\rm h}\left(\omega^2\right)$ is directly obtained from the spatially summed two-point correlator $G(t)$ of the electromagnetic current, i.e.

$$\hat{\Pi}_{\rm h}\left(\omega^2\right) = -\frac{\pi}{\alpha}\Pi_{\rm h}\left(-\omega^2\right) = 4\pi^2\int_0^\infty dt\ G(t)\left[t^2 - \frac{4}{\omega^2}\sin^2\left(\frac{t\omega}{2}\right)\right], \tag{4.1}$$

with

$$G(t)\delta_{kl} = -\int d^3x\ \langle J_k(x)J_l(0)\rangle, \tag{4.2}$$

where $J_\mu(x)$ is the electromagnetic current, ω^2 is the Euclidean momentum and t is the Euclidean time (note that in this Chapter t in not the Mandelstam variable). Therefore, according to [132], the hadronic vacuum polarization $a_\mu^{\rm HVP}$ at LO is given by

$$a_\mu^{\rm HVP}({\rm LO}) = \left(\frac{\alpha}{\pi}\right)^2\int_0^\infty dt\ G(t)\ \tilde{K}^{(2)}(t, m_\mu)\ , \tag{4.3}$$

where $\tilde{K}^{(2)}(t, m_\mu)$ is the leading order time-kernel. The t-dependent kernel function is obtained by performing the integral

$$\tilde{K}^{(2)}(t, m_\mu) = \tilde{f}_2(t) = 8\pi^2 \int_0^\infty \frac{d\omega}{\omega} f_2(\omega^2) g(\omega t), \tag{4.4}$$

where

$$g(w) = w^2 - 4\sin^2\left(\frac{w}{2}\right). \tag{4.5}$$

In the following, we will use extensively the adimensional momentum and time

$$\hat{\omega} = \frac{\omega}{m_\mu}, \quad \hat{t} = m_\mu t. \tag{4.6}$$

The function $f_2(\omega^2)$ can be written by using the space-like kernel $F^{(2)}(1/y(z))$ from Eq. (3.26)

$$f_2(\omega^2) = \frac{1}{m_\mu^2} \frac{F^{(2)}(1/y(-\hat{\omega}^2))}{-\hat{\omega}^2}, \tag{4.7}$$

where $y(z)$ is rationalizing variable

$$y(z) = \frac{z - \sqrt{z(z-4)}}{z + \sqrt{z(z-4)}}. \tag{4.8}$$

Therefore, substituting the expression of $F^{(2)}(1/y(z))$ from Eq. (3.26) one obtains

$$f_2(\omega^2) = \frac{1}{m_\mu^2} \frac{1}{y(-\hat{\omega}^2)(1 - y^2(-\hat{\omega}^2))}. \tag{4.9}$$

The integration over ω is complicated and reported in Ref. [132], the result contains a Miejer G-function and a modified Bessel function:

$$\frac{m_\mu^2}{8\pi^2}\tilde{f}_2(t) = \frac{1}{4} G^{2,1}_{1,3}\left(\begin{matrix} \frac{3}{2} \\ 0, 1, \frac{1}{2} \end{matrix} \middle| \hat{t}^2 \right) + \frac{\hat{t}^2}{4} + \frac{1}{\hat{t}^2} + 2\ln(\hat{t}) - \frac{2}{\hat{t}} K_1(2\hat{t}) + 2\gamma - \frac{1}{2}. \tag{4.10}$$

This expression can be also written in terms of integrals of the Bessel functions instead of the Meijer G-function (see a similar integral in Ref. [133]). This can be done by applying to Eq. (4.10) the identity

$$\begin{aligned} G^{2,1}_{1,3}\left(\begin{matrix} \frac{3}{2} \\ 0, 1, \frac{1}{2} \end{matrix} \middle| \hat{t}^2 \right) &= -2 + 8\int_0^{\hat{t}} dv (v - \hat{t}) K_0(2v) \\ &= -4\hat{t}K_1(2\hat{t}) - 4\pi\hat{t}^2 \left(K_0(2\hat{t})\mathbf{L}_{-1}(2\hat{t}) + K_1(2\hat{t})\mathbf{L}_0(2\hat{t}) \right), \end{aligned} \tag{4.11}$$

where $\mathbf{L}_{-1}$ and $\mathbf{L}_0$ are Struve functions.

4.2 The time-kernel at NLO

Similarly to the LO, the hadronic vacuum polarization contribution at NLO ($4a$) in the TMR can be written as follows

$$a_\mu^{\rm HVP}({\rm NLO}) = \left(\frac{\alpha}{\pi}\right)^3 \int_0^\infty dt\; G(t)\; \tilde{K}^{(4)}(t, m_\mu), \tag{4.12}$$

where $\tilde{K}^{(4)}(t, m_\mu)$ is the NLO time-kernel. The t-dependent kernel function is obtained by performing the integral

$$\tilde{K}^{(4)}(t, m_\mu) = \tilde{f}_4(t) = 8\pi^2 \int_0^\infty \frac{d\omega}{\omega} f_4(\omega^2) g(\omega t). \tag{4.13}$$

For convenience we define an adimensional $\hat{f}_4(\hat{\omega}^2)$:

$$f_4(\omega^2) = \frac{1}{m_\mu^2} \hat{f}_4(\hat{\omega}^2). \tag{4.14}$$

As in the previous section, the function $\hat{f}_4(\hat{\omega}^2)$ is related to the NLO space-like kernel $F^{(4)}(1/y(z))$ from Eq. (3.35)

$$\hat{f}_4(\hat{\omega}^2) = \frac{2F^{(4)}(1/y(-\hat{\omega}^2))}{-\hat{\omega}^2}. \tag{4.15}$$

In order to simplify the computation, by splitting the function $g(\omega t)$, we divided the integral (4.13) into two parts

$$\tilde{f}_4(t) = \tilde{f}_4^{(a)}(t) + \tilde{f}_4^{(b)}(t). \tag{4.16}$$

The first part is

$$\frac{m_\mu^2}{8\pi^2} \tilde{f}_4^{(a)}(t) = \int_0^\infty \frac{d\hat{\omega}}{\hat{\omega}} \hat{f}_4(\hat{\omega}^2)(\hat{\omega}^2 \hat{t}^2). \tag{4.17}$$

This integral can be calculated in an analytical form. In fact, by substituting the expression given in Eq. (4.15), changing the variable $\hat{\omega}^2 \to y$, taking into account that $F^{(4)}(z)$ represents the imaginary part of the time-like kernel function $K^{(4)}(z)$ as in Eq. (3.34) and employing the dispersive integral for $K^{(4)}(z)$, we arrived at the following result [128]:

$$\begin{aligned} \frac{m_\mu^2}{16\pi^2} \tilde{f}_4^{(a)}(t) &= \frac{\hat{t}^2}{2} \int_{-\infty}^0 \frac{dz}{z} F^{(4)}(1/y(z)) \\ &= \frac{\hat{t}^2}{2} \int_{-\infty}^0 \frac{dz}{z} \frac{1}{\pi} {\rm Im}\, K^{(4)}(z) = \frac{\hat{t}^2}{2} K^{(4)}(0) \\ &= \frac{\hat{t}^2}{2} \left(\frac{197}{144} + \frac{\pi^2}{12} - \frac{1}{2}\pi^2 \ln 2 + \frac{3}{4}\zeta(3) \right). \end{aligned} \tag{4.18}$$

In the above expression $K^{(4)}(0)$ is the value of the two-loop QED contribution to g-2 [5]. Notice that we have incorporated the factor 2 from Eq. (4.15) in the denominator $16\pi^2$.

The second part of the Eq. (4.16) is

$$\frac{m_\mu^2}{8\pi^2}\tilde{f}_4^{(b)}(t) = \int_0^\infty \frac{d\hat{\omega}}{\hat{\omega}}\hat{f}_4(\hat{\omega}^2)\left(-4\sin^2\left(\frac{\hat{\omega}\hat{t}}{2}\right)\right). \tag{4.19}$$

Substituting the expression (4.15) in Eq. (4.19), it becomes apparent that the integrand involves terms like $\ln(y)$, $\ln(1\pm y)$, $\mathrm{Li}_2(\pm y)$. While we could integrate analytically individual logarithmic terms and products of logarithms, yielding intricate expressions involving various Bessel functions, exponential integrals, and Meijer G-functions, we encountered challenges in analytically calculating the integrals involving dilogarithms of y. As an alternative, in the next sections we will work out some series expansions for $\tilde{f}_4(t)$.

4.3 Expansion for small $\hat{t}$

In this section we will work out the expansion of the NLO time-kernel (4.13) for $\hat{t} \ll 1$. We splitted the interval of integration using an intermediate point $\hat{\omega}_0(\hat{t})$:

$$\int_0^\infty \frac{d\hat{\omega}}{\hat{\omega}}\hat{f}_4(\hat{\omega}^2)g(\hat{\omega}\hat{t}) = \int_0^{\hat{\omega}_0(\hat{t})} \frac{d\hat{\omega}}{\hat{\omega}}\hat{f}_4(\hat{\omega}^2)g(\hat{\omega}\hat{t}) + \int_{\hat{\omega}_0(\hat{t})}^\infty \frac{d\hat{\omega}}{\hat{\omega}}\hat{f}_4(\hat{\omega}^2)g(\hat{\omega}\hat{t}). \tag{4.20}$$

Since the value of the integral is independent of the point of splitting $\hat{\omega}_0(\hat{t})$, a convenient choice is

$$\hat{\omega}_0(\hat{t}) = \frac{1-\hat{t}}{\sqrt{\hat{t}}} \gg 1. \tag{4.21}$$

For the first integral, we expanded in series $g(\hat{\omega}\hat{t})$ for $\hat{t} \ll 1$, then we made the convenient change of variable $\hat{\omega} \to y = y(-\hat{\omega}^2)$ (see Eq. (4.15)) and we integrated over the interval $-1 \le y \le y(-\hat{\omega}_0^2) = -\hat{t}$. In the second integral, we expanded in series $\hat{f}_4(\hat{\omega}^2)$ for $\hat{\omega} \gg 1$ and integrated over $\hat{\omega}$. The whole $\tilde{f}_4(t)$ is obtained summing up the results of the two integrals. The expansion has the form

$$\frac{m_\mu^2}{16\pi^2}\tilde{f}_4(t) = \sum_{\substack{n\ge 4\\ n\ \text{even}}} \frac{\hat{t}^n}{n!}\left(a_n + b_n\pi^2 + c_n\left(\ln(\hat{t}) + \gamma\right) + d_n\left(\ln(\hat{t}) + \gamma\right)^2\right). \tag{4.22}$$

The coefficients a_n, b_n, c_n and d_n of the expansion up to $\hat{t}^{30}$ are available in Table B.1 in Appendix B (from [128]).

4.4 Asymptotic expansions for large $\hat{t}$

According to the different behaviour of the function $\tilde{f}_4^{(b)}$ for $t \to \infty$, we decomposed it into two parts:

$$\tilde{f}_4^{(b)}(t) = \tilde{f}_4^{(b;1)}(t) + \tilde{f}_4^{(b;2)}(t). \tag{4.23}$$

4.4.1 Main contribution

The dominant contribution is the non-exponential part $\tilde{f}_4^{(b;1)}$, and its asymptotic expansion contains power of $1/\hat{t}$

$$\tilde{f}_4^{(b;1)}(t) = A_0 + A_1\hat{t} + B_0 \ln(\hat{t}) + B_2\frac{\ln(\hat{t})}{\hat{t}^2} + \sum_{n=1}^{\infty}\frac{C_n}{\hat{t}^n}. \tag{4.24}$$

Using the relation $\sin(u)^2 = \frac{1}{2}(1-\cos(2u))$, we splitted the integrand of Eq. (4.19)

$$\frac{m_\mu^2}{8\pi^2}\tilde{f}_4^{(b;1)}(t) = 2\lim_{\epsilon\to 0}\left[\int_\epsilon^\infty \frac{d\hat{\omega}}{\hat{\omega}}\hat{f}_4(\hat{\omega}^2) - \int_\epsilon^\infty \frac{d\hat{\omega}}{\hat{\omega}}\hat{f}_4(\hat{\omega}^2)\cos(\hat{\omega}\hat{t})\right], \tag{4.25}$$

where ϵ serves as a regulator for the divergence in $\hat{\omega}=0$. The coefficients A_n, B_n, C_n can be obtained by expanding in series $\hat{f}_4(\hat{\omega}^2)$ around $\hat{\omega}=0$,

$$\hat{f}_4(\hat{\omega}^2) = \frac{1}{8\hat{\omega}} - \frac{1}{2} + \left(\frac{\ln(\hat{\omega})}{2} + \frac{251}{2880} + \ln 2\right)\hat{\omega} + \dots, \tag{4.26}$$

substituting it in the second integral of Eq. (4.25) and formally integrating term by term over $\hat{\omega}$ using

$$\int d\hat{\omega}\,\hat{\omega}^n\cos(\hat{\omega}\,\hat{t}) = -n!\sin(n\pi/2)\,\hat{t}^{-1-n}\,. \tag{4.27}$$

The first terms of the asymptotic expansion are [128]:

$$\begin{aligned}\frac{m_\mu^2}{16\pi^2}\tilde{f}_4^{(b;1)}(t) = &-\frac{\pi\hat{t}}{8} + \ln\hat{t} - \frac{7\zeta(3)}{4} + \frac{7}{6}\pi^2\ln(2) - \frac{127\pi^2}{144} + \gamma + \\ &+ \frac{653}{216} - \frac{5(\ln\hat{t}+\gamma)}{12\hat{t}^2} - \frac{\pi}{2\hat{t}} + \frac{209}{180\hat{t}^2} + \frac{277\pi}{360\hat{t}^3} + O\left(\frac{1}{\hat{t}^4}\right).\end{aligned} \tag{4.28}$$

4.4.2 Exponentially suppressed contribution

The contribution exponentially suppressed is denoted by $\tilde{f}_4^{(b;2)}$. Indeed, its asymptotic expansion contains the factor $e^{-2\hat{t}}$

$$\tilde{f}_4^{(b;2)}(t) = e^{-2\hat{t}}\sum_{n=0}^{\infty}\left(D_n + \frac{E_n\ln(\hat{t})+F_n}{\sqrt{\hat{t}}}\right)\frac{1}{\hat{t}^n}\,, \tag{4.29}$$

where D_n, E_n and F_n are constants.

The function $\tilde{f}_4^{(b;2)}(t)$ could also be represented as the integral over the contour $\mathcal{C}$ shown in Fig. 4.1:

$$\frac{m_\mu^2}{8\pi^2}\tilde{f}_4^{(b;2)}(t) = \int_{\mathcal{C}}\frac{d\hat{\omega}}{\hat{\omega}}\hat{f}_4(\hat{\omega}^2)2\cos\left(\hat{\omega}\hat{t}\right). \tag{4.30}$$

The appearance of the exponential factor is due to the singularities of the integrand in $\hat{\omega}=\pm 2i$, which come from the terms containing $\sqrt{\hat{\omega}^2+4}$ in $\hat{f}_4(\hat{\omega})$.

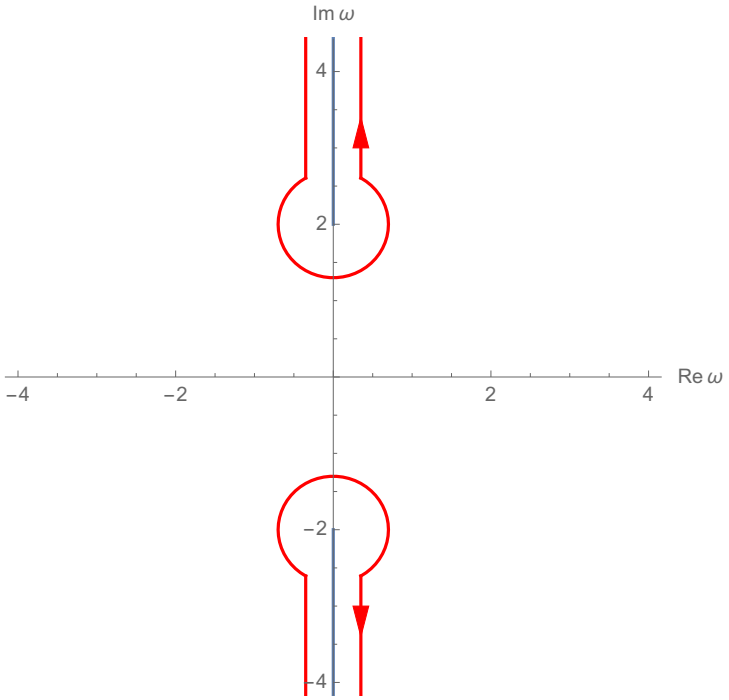

Figure 4.1: In red, the path of integration around the discontinuities (in blue) giving the exponentially suppressed contribution.

Since the coefficients of the expansions (4.24) and (4.29) grows factorially, for a given value of $\hat{t}$, one needs to truncate the series, nevertheless the error due to the truncation of the first series is of the same order of magnitude of the value of the second series. This means that the asymptotic expansions (4.24) and (4.29) have a limited use for numerical evaluations.

Due to this fact, in the next sections we will explore a different approach, able to find expansions around a *finite* point $\hat{t} = \hat{t}_0$ converging for $\hat{t} \to \infty$.

4.5 w-Integral representation for $\hat{f}_4^{(b)}$

We started from the definition (4.19), adding and subtracting to the integrand $\hat{f}_4(\hat{\omega}^2)/\hat{\omega}$ a piece $h_0(\hat{\omega})$, which contains the terms non-integrable in $\hat{\omega} = 0$ or $\hat{\omega} = \pm 2i$,

$$h_0(\hat{\omega}) = \frac{1}{8\hat{\omega}^2} + \frac{\hat{\omega}\pi}{16(4+\hat{\omega}^2)^{3/2}} - \frac{\pi}{2(4+\hat{\omega}^2)} \ . \tag{4.31}$$

Defining

$$g_b(\hat{\omega}) = \frac{\hat{f}_4(\hat{\omega}^2)}{\hat{\omega}} - h_0(\hat{\omega}), \tag{4.32}$$

and

$$\begin{aligned}\tilde{h}_0(\hat{t}) &= \int_0^\infty 2\left(\cos(\hat{\omega}\hat{t})-1\right)h_0(\hat{\omega})\,d\hat{\omega} \\ &= \frac{\pi\hat{t}}{16}+\frac{\pi^2}{8}\left(e^{-2\hat{t}}-1\right)+\frac{1}{32}\pi^2\hat{t}\left(K_0(2\hat{t})-\mathbf{L}_0(2\hat{t})\right),\end{aligned} \tag{4.33}$$

we wrote

$$\frac{m_\mu^2}{16\pi^2}\tilde{f}_4^{(b)}(t)=\tilde{h}_0(\hat{t})+\int_0^\infty d\hat{\omega}\;2\left(\cos(\hat{\omega}\hat{t})-1\right)g_b(\hat{\omega}). \tag{4.34}$$

At this point we focused only on the integral with the cosine, decomposing the cosine in exponentials

$$\int_0^\infty d\hat{\omega}\;g_b(\hat{\omega})\cos\left(\hat{\omega}\hat{t}\right)=\int_0^\infty d\hat{\omega}\;g_b(\hat{\omega})\frac{e^{i\hat{\omega}\hat{t}}+e^{-i\hat{\omega}\hat{t}}}{2}, \tag{4.35}$$

then splitting the integral. For the first exponential we rotated of $\pi/2$ the integration path in the complex-$\hat{\omega}$ plane and made the change of variable $\hat{\omega}\to iw$. Similarly, for the second one, we rotated of $-\pi/2$ the integration path and made the change $\hat{\omega}\to -iw$. Therefore:

$$\int_0^{i\infty} d\hat{\omega}\;g_b(\hat{\omega})\frac{e^{i\hat{\omega}\hat{t}}}{2}+\int_0^{-i\infty} d\hat{\omega}\;g_b(\hat{\omega})\frac{e^{-i\hat{\omega}\hat{t}}}{2}=\int_0^\infty dw\;F_{0\infty}(w)e^{-w\hat{t}}, \tag{4.36}$$

where $F_{0\infty}(w)$ is

$$F_{0\infty}(w)=\frac{i}{2}\lim_{\epsilon\to 0^+}\left(g_b(\epsilon+iw)-g_b(\epsilon-iw)\right)\;; \tag{4.37}$$

in which we have introduced the regulator ϵ to make sure that the integration path remain in the half-plane $\Re(\hat{\omega})>0$. Due to the presence of the discontinuity, the limit is different if $0<w<2$ or $w>2$

$$F_{0\infty}(w)=\begin{cases}F_{02}(w), & \text{if } 0<w<2\\ F_{2\infty}(w), & \text{if } w>2\end{cases} \tag{4.38}$$

For this reason the total integral becomes [128]

$$\frac{m_\mu^2}{16\pi^2}\tilde{f}_4^{(b)}(t)=\tilde{h}_0(\hat{t})+\int_0^2 dw\;F_{02}(w)2(e^{-w\hat{t}}-1)+\int_2^\infty dw\;F_{2\infty}(w)2(e^{-w\hat{t}}-1), \tag{4.39}$$

where

$$\begin{aligned}F_{02}(w) &= \frac{4}{3w^3}+\frac{w}{16\left(w^2-4\right)} \\ &+\pi\sqrt{4-w^2}\left(\frac{w}{16\left(w^2-4\right)^2}-\frac{1}{8w^2}+\frac{7}{48}\right) \\ &+\left[\sqrt{4-w^2}\left(-\frac{4}{3w^4}-\frac{17}{48w^2}-\frac{5}{16\left(w^2-4\right)}\right.\right. \\ &\left.\left.-\frac{1}{4\left(w^2-4\right)^2}+\frac{1}{8}\right)+\pi\left(\frac{1}{2w^3}+\frac{w}{2}-\frac{7}{6w}\right)\right]\times \\ &\arcsin\left(\frac{w}{2}\right)+\frac{23w}{144}-\frac{37}{144w}+\frac{5}{24}w\ln(w),\end{aligned} \tag{4.40}$$

and

$$\begin{aligned} F_{2\infty}(w) = & \frac{4}{3w^3} + \frac{w}{16\left(w^2-4\right)} \\ & + \left(\frac{7}{24} - \frac{1}{4w^2}\right)\sqrt{w^2-4}\ln\left(w\left(w^2-4\right)\right) \\ & + \sqrt{w^2-4}\left(-\frac{1}{3w^4} + \frac{115}{144w^2} + \frac{23}{144\left(w^2-4\right)} - \frac{23}{144}\right) \\ & + \left[-\frac{4}{3w^5} + \frac{7}{6w^3} + \frac{w}{2\left(w^2-4\right)} - \frac{29w}{24} + \frac{47}{12w}\right. \\ & - \sqrt{w^2-4}\left(-\frac{4}{3w^4} - \frac{17}{48w^2} - \frac{5}{16\left(w^2-4\right)}\right. \\ & \left.\left. - \frac{1}{4\left(w^2-4\right)^2} + \frac{1}{8}\right)\right]\frac{\ln(y(w))}{2} + \frac{23w}{144} - \frac{37}{144w} \\ & + \frac{5}{24}w\ln(w) - \left(\frac{1}{w^3} + w - \frac{7}{3w}\right)L(y(w)), \end{aligned} \tag{4.41}$$

with

$$L(x) = \mathrm{Li}_2(-x) + 2\mathrm{Li}_2(x) + \frac{1}{2}\ln(x)\left(\ln(1+x) + 2\ln(1-x)\right)\ ; \tag{4.42}$$

the function $y(z)$ was defined in Eq. (4.8).

In order to integrate analytically over w the terms of Eq. (4.39), not containing the exponential, we had to add and subtract the pole term of the Laurent expansion of $F_{02}(w)$ in $w = 0$

$$F_{02}(w) = -\frac{1}{2w} + O(1), \tag{4.43}$$

obtaining [128]

$$\frac{m_\mu^2}{16\pi^2}\tilde{f}_4^{(b)}(t) = c_0 + \tilde{h}_0(\hat{t}) + \tilde{h}_3(\hat{t}) + \int_0^2 dw\ 2(F_{02}(w) + \frac{1}{2w})e^{-w\hat{t}} + \int_0^2 dw\ 2F_{2\infty}(w)e^{-w\hat{t}}, \tag{4.44}$$

where

$$\begin{aligned} c_0 &= -2\int_0^2 dw\left(F_{02}(w) + \frac{1}{2w}\right) - 2\int_2^\infty dw\ F_{2\infty}(w) \\ &= \frac{653}{216} + \frac{\pi}{16} - \ln(2) - \frac{163}{144}\pi^2 + \frac{7}{6}\pi^2\ln(2) - \frac{7\zeta(3)}{4}, \end{aligned} \tag{4.45}$$

and

$$\tilde{h}_3(\hat{t}) = \int_0^2 dw\ \frac{1-e^{-w\hat{t}}}{w} = -\mathrm{Ei}(-2\hat{t}) + \ln(2\hat{t}) + \gamma. \tag{4.46}$$

4.6 w-integral for exponentially suppressed contribution $\tilde{f}_4^{(b;2)}(t)$

For the exponentially suppressed contribution $\tilde{f}_4^{(b;2)}(t)$, we proceed similarly to the previous section. Starting from the equation (4.30), we added and subtracted the pole term

$h_2(\hat{\omega})$ of the Laurent expansion of $\hat{f}_4(\hat{\omega^2})/\hat{\omega}$ in $\hat{\omega} = \pm 2i$, obtaining

$$\frac{m_\mu^2}{16\pi^2}\tilde{f}_4^{(b;2)}(t) = \tilde{h}_2(\hat{t}) + \int_{\mathcal{C}} d\hat{\omega}\; g_5(\hat{\omega}) 2\cos(\hat{\omega}\hat{t}), \tag{4.47}$$

with

$$g_5(\hat{\omega}) = \frac{\hat{f}_4(\hat{\omega}^2)}{\hat{\omega}} - h_2(\hat{\omega})\;, \tag{4.48}$$

$$h_2(\hat{\omega}) = -\frac{\pi}{2(4+\hat{\omega}^2)}\;, \tag{4.49}$$

$$\tilde{h}_2(\hat{t}) = \int_0^\infty d\hat{\omega}\; 2\cos(\hat{\omega}\hat{t}) h_2(\hat{\omega}) = -\frac{\pi^2}{4} e^{-2\hat{t}}\;. \tag{4.50}$$

Considering a path $\mathcal{C}$ infinitesimally near the cuts (see Fig. 4.1), we decomposed the cosine and made a suitable change of variables in order to parameterize $\mathcal{C}$ with the same w. In particular, we needed to take the difference between the values of g_5 between the two cuts, and on the left and the right of each cut:

$$F_5(w) = \frac{i}{2}\left[\lim_{\epsilon\to 0^+} g_5(\epsilon + iw) - \lim_{\epsilon\to 0^-} g_5(\epsilon + iw) - \lim_{\epsilon\to 0^+} g_5(\epsilon - iw) + \lim_{\epsilon\to 0^-} g_5(\epsilon - iw)\right]. \tag{4.51}$$

Finally, we obtained [128]

$$\frac{m_\mu^2}{16\pi^2}\tilde{f}_4^{(b;2)}(t) = \tilde{h}_2(\hat{t}) + \int_0^2 dw\; F_5(w) 2e^{-w\hat{t}}, \tag{4.52}$$

where

$$\begin{aligned} F_5(w) = {} & \frac{-23w^6 + 230w^4 - 508w^2 + 192}{144w^4\sqrt{w^2-4}} \\ & - \frac{-29w^8 + 222w^6 - 348w^4 - 144w^2 + 128}{48w^5\left(w^2-4\right)} \ln\left(y\left(w^2\right)\right) \\ & - \left(\frac{1}{w^3} + w - \frac{7}{3w}\right)\left(L\left(y\left(w^2\right)\right) + \frac{\pi^2}{4}\right) \\ & + \left(\frac{7}{24} - \frac{1}{4w^2}\right)\sqrt{w^2-4}\ln\left(w\left(w^2-4\right)\right). \end{aligned} \tag{4.53}$$

The asymptotic expansion of Eq. (4.29) could also be obtained from the integral representation of Eq. (4.52), by expanding $F_5(w)$ and $e^{-w\hat{t}}$ in $w = 2$ and by integrating term-by-term over w. Additionally, we noted that $F_{2\infty}(w)$ also generates all the exponentially suppressed contributions generated by $F_5(w)$. In fact, we checked that the difference $F_{2\infty}(w) - F_5(w)$ is a function regular in $w = 2$[1].

[1]Not all the parts of $\hat{f}_4(\hat{\omega}^2)/\hat{\omega}$, which have a discontinuity for $\hat{\omega}^2 < -4$, once integrated over $\hat{\omega}$, give contributions whose asymptotic behaviour contains $e^{-2\hat{t}}$ terms. An example comes from second term of $h_0(\hat{\omega})$, its asymptotic expansion $\int_0^\infty d\hat{\omega}\; \frac{2\hat{\omega}\cos(\hat{\omega}\hat{t})}{(\hat{\omega}^2+4)^{3/2}} = -\frac{1}{4\hat{t}^2} - \frac{9}{16\hat{t}^4} - \frac{225}{64\hat{t}^6} + O\left(\frac{1}{\hat{t}^8}\right)$ does not contain $e^{-2\hat{t}}$.

4.7 Further subdivisions of $f_4^{(b)}(t)$

In the previous sections we obtained the w-integral representation for $f_4^{(b)}(t) = f_4^{(b;1)}(t) + f_4^{(b;2)}(t)$ in Eq. (4.44) and for the exponentially suppressed part of $f_4^{(b;2)}(t)$ in Eq. (4.52). In particular, in Eq. (4.24) and (4.29) we have shown also the general form of their asymptotic expansions. Each of these expressions contains contributions with slightly different behaviour. In order to obtain numerically efficient expansions around finite $\hat{t}$, we have to introduce further splitting, separating even and odd powers in $f_4^{(b;1)}(t)$ and integer, half-integer powers, and logarithms in $f_4^{(b;2)}(t)$. Therefore, we subdivided $f_4^{(b;1)}(t)$ and $f_4^{(b;2)}(t)$ in three parts, according their asymptotic behaviour:

$$\begin{aligned} \tilde{f}_4^{(b;1)}(t) &= \tilde{f}_4^{(b;1;1)}(t) + \tilde{f}_4^{(b;1;2)}(t) + \tilde{f}_4^{(b;1;3)}(t) \\ \tilde{f}_4^{(b;2)}(t) &= \tilde{f}_4^{(b;2;1)}(t) + \tilde{f}_4^{(b;2;2)}(t) + \tilde{f}_4^{(b;2;3)}(t) \end{aligned} \tag{4.54}$$

where

$$\begin{aligned} \frac{m_\mu^2}{16\pi^2}\tilde{f}_4^{(b;1;1)}(t) &\sim \frac{1}{\hat{t}} + O\left(\frac{1}{\hat{t}^3}\right), \\ \frac{m_\mu^2}{16\pi^2}\tilde{f}_4^{(b;1;2)}(t) &\sim \frac{1}{\hat{t}^2} + O\left(\frac{1}{\hat{t}^4}\right), \\ \frac{m_\mu^2}{16\pi^2}\tilde{f}_4^{(b;2;1)}(t) &\sim e^{-2\hat{t}}\left[1 + O\left(\frac{1}{\hat{t}^2}\right)\right], \\ \frac{m_\mu^2}{16\pi^2}\tilde{f}_4^{(b;2;2)}(t) &\sim e^{-2\hat{t}}\frac{\ln(\hat{t})}{\sqrt{\hat{t}}}\left[1 + O\left(\frac{1}{\hat{t}}\right)\right], \\ \frac{m_\mu^2}{16\pi^2}\tilde{f}_4^{(b;2;3)}(t) &\sim e^{-2\hat{t}}\frac{1}{\sqrt{\hat{t}}}\left[1 + O\left(\frac{1}{\hat{t}}\right)\right]. \end{aligned} \tag{4.55}$$

The remain function $\tilde{f}_4^{(b;1;3)}(t)$ contains the part not included in the above asymptotic expansions:

$$\frac{m_\mu^2}{16\pi^2}\tilde{f}_4^{(b;1;3)}(t) = \frac{653}{216} - \frac{127\pi^2}{144} - \frac{7\zeta(3)}{4} + \frac{7}{6}\pi^2\ln(2) + \left(\ln\hat{t} + \gamma\right)\left(1 - \frac{5}{12\hat{t}^2}\right) - \frac{\pi\hat{t}}{8}\,. \tag{4.56}$$

4.7.1 Subdivision of the exponentially suppressed contribution

Analyzing the asymptotic expansions due to each term of $F_5(w)$, it is possible to isolate and regroup the terms with same asymptotic behaviour. We found that [128]

$$\frac{m_\mu^2}{16\pi^2}\tilde{f}_4^{(b;2;1)}(t) = \tilde{h}_2(\hat{t}) + \int_2^\infty dw\; 2F_5^{(1)}(w)e^{-w\hat{t}}\,, \tag{4.57}$$

$$\frac{m_\mu^2}{16\pi^2}\tilde{f}_4^{(b;2;2)}(t) = \ln(\hat{t})\int_2^\infty dw\; 2F_5^{(2)}(w)e^{-w\hat{t}}\,, \tag{4.58}$$

$$\frac{m_\mu^2}{16\pi^2}\tilde{f}_4^{(b;2;3)}(t) = \int_2^\infty dw\; 2F_5^{(3)}(w)e^{-w\hat{t}}\,, \tag{4.59}$$

where

$$F_5^{(1)}(w) = \frac{\pi^2}{4}\left(+\frac{7}{3w} - w - \frac{1}{w^3}\right) , \tag{4.60}$$

$$F_5^{(2)}(w) = \frac{1}{2}\left(\sqrt{w^2-4}\left(\frac{1}{4w^2} - \frac{7}{24}\right) - \frac{1}{2}\left(\frac{1}{w^3} + w - \frac{7}{3w}\right)\ln(y(w^2))\right) , \tag{4.61}$$

$$F_5^{(3)}(w) = F_5(w) - F_5^{(1)}(w) - F_5^{(2)}(w)\ln\hat{t} . \tag{4.62}$$

4.7.2 Subdivision of the main asymptotic contribution

As before, we were able to separate the parts of $F_{02}(w)$ and $F_{2\infty}(w)$ which generate the contributions containing the odd and the even powers of $1/\hat{t}$, $\tilde{f}_4^{(b;1;1)}(t)$ and $\tilde{f}_4^{(b;1;2)}(t)$. Remembering that the odd powers have a factor π (see Eq. (4.28)), we obtained [128]

$$\frac{m_\mu^2}{16\pi^2}\tilde{f}_4^{(b;1;1)}(t) = \int_0^2 dw\; 2F_{02}^{\text{odd}}(w)e^{-w\hat{t}} + \int_2^\infty dw\; 2F_{2\infty}^{\text{odd}}(w)e^{-w\hat{t}} , \tag{4.63}$$

where

$$F_{02}^{\text{odd}}(w) = \frac{\pi}{2}\left(\sqrt{4-w^2}\left(\frac{7}{24} - \frac{1}{4w^2}\right) + \left(\frac{1}{w^3} + w - \frac{7}{3w}\right)\arcsin\left(\frac{w}{2}\right)\right) , \tag{4.64}$$

$$F_{2\infty}^{\text{odd}}(w) = \frac{\pi^2}{4}\left(\frac{1}{w^3} + w - \frac{7}{3w}\right) . \tag{4.65}$$

The part with even powers of $1/\hat{t}$ can be found subtracting everything from the whole integral

$$\begin{aligned}\frac{m_\mu^2}{16\pi^2}\tilde{f}_4^{(b;1;2)}(t) = {} & c_0 - \hat{f}_4^{(b;1;3)}(t) - \tilde{h}_2(\hat{t}) + \tilde{h}_0(\hat{t}) + \tilde{h}_3(\hat{t}) \\ & + \int_0^2 dw\; 2\left(F_{02}(w) + \frac{1}{2w} - F_{02}^{\text{odd}}(w)\right)e^{-w\hat{t}} \\ & + \int_2^\infty dw\; 2\left(F_{2\infty}(w) - F_5(w) - F_{2\infty}^{\text{odd}}(w)\right)e^{-w\hat{t}} .\end{aligned} \tag{4.66}$$

4.8 Expansion in a finite point $\hat{t} = \hat{t}_0$

First, we started defining the series removed of any leading factor,

$$\bar{f}_4^{(b;2;1)}(t) = \tilde{f}_4^{(b;2;1)}(t)\; e^{2\hat{t}} , \tag{4.67}$$

$$\bar{f}_4^{(b;2;2)}(t) = \tilde{f}_4^{(b;2;2)}(t)\; e^{2\hat{t}}\sqrt{\hat{t}}/\ln\hat{t} , \tag{4.68}$$

$$\bar{f}_4^{(b;2;3)}(t) = \tilde{f}_4^{(b;2;3)}(t)\; e^{2\hat{t}}\sqrt{\hat{t}} , \tag{4.69}$$

$$\bar{f}_4^{(b;1;1)}(t) = \tilde{f}_4^{(b;1;1)}(t)\; \hat{t} , \tag{4.70}$$

$$\bar{f}_4^{(b;1;2)}(t) = \tilde{f}_4^{(b;1;2)}(t)\; \hat{t}^2 . \tag{4.71}$$

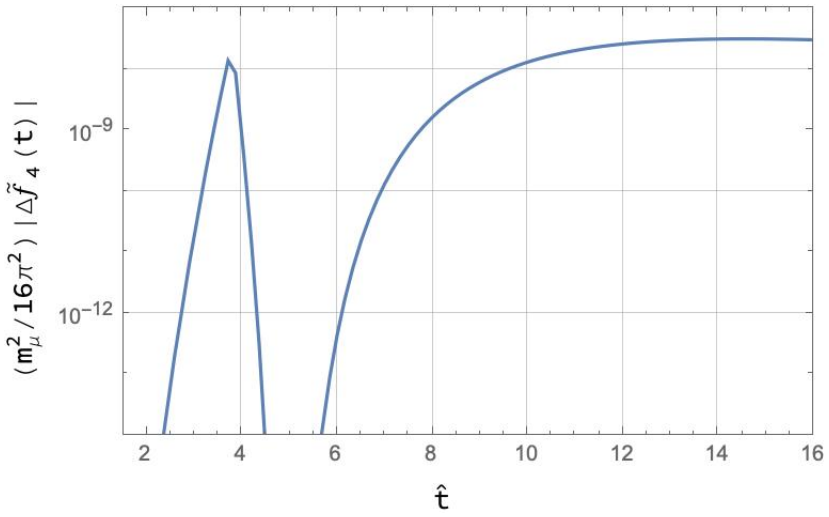

Figure 4.2: Absolute value of the difference between the approximate value of $\tilde{f}_4(t)$ obtained from the series expansions and the value obtained by direct numerical integration.

Then, we expanded around a finite point $\hat{t} = \hat{t}_0$ by substituting t with $\hat{t}_0/(1+v)^{1/2}$ in $\hat{f}_4^{(b;1;x)}(t)$ and with $\hat{t}_0/(1+v)$ in $\hat{f}_4^{(b;2;x)}(t)$, and expanding in v

$$\frac{m_\mu^2}{16\pi^2}\bar{f}_4^{(b;1;1)}\left(\frac{\hat{t}_0}{\sqrt{1+v}}\right) = \sum_{n=0}^{\infty} a_n^{(b;1;1)} v^n, \tag{4.72}$$

$$\frac{m_\mu^2}{16\pi^2}\bar{f}_4^{(b;1;2)}\left(\frac{\hat{t}_0}{\sqrt{1+v}}\right) = \sum_{n=0}^{\infty} a_n^{(b;1;2)} v^n, \tag{4.73}$$

$$\frac{m_\mu^2}{16\pi^2}\bar{f}_4^{(b;2;1)}\left(\frac{\hat{t}_0}{1+v}\right) = \sum_{n=0}^{\infty} a_n^{(b;2;1)} v^n, \tag{4.74}$$

$$\frac{m_\mu^2}{16\pi^2}\bar{f}_4^{(b;2;2)}\left(\frac{\hat{t}_0}{1+v}\right) = \sum_{n=0}^{\infty} a_n^{(b;2;2)} v^n, \tag{4.75}$$

$$\frac{m_\mu^2}{16\pi^2}\bar{f}_4^{(b;2;3)}\left(\frac{\hat{t}_0}{1+v}\right) = \sum_{n=0}^{\infty} a_n^{(b;2;3)} v^n. \tag{4.76}$$

These particular substitutions $\hat{t} \to v$ are chosen to improve the convergence of the series in v for $\hat{t} \to \infty$, corresponding to $v \to -1$. The series converge if $|v| \leq 1$ corresponding to $\hat{t} \geq \hat{t}_0/2$.

The coefficients $a_n^{(b;x;y)}$ can be obtained from the w-integral representations (4.63), (4.66), (4.57), (4.58), (4.59), by expanding the integrands in v and integrating numerically term by term in w. Finally, we derived $\tilde{f}_4^{(b)}(t)$ summing up all the six contributions, and

the whole time-kernel $\tilde{f}_4(t)$ is recovered adding also $\tilde{f}_4^{(a)}(t)$:

$$\begin{aligned}\frac{m_\mu^2}{16\pi^2}\tilde{f}_4(t) = &\frac{m_\mu^2}{16\pi^2}\tilde{f}_4^{(a)}(t) + \frac{m_\mu^2}{16\pi^2}\tilde{f}_4^{(b;1;3)}(t) \\ &+ \frac{1}{\hat{t}}\sum_{n=0}^{\infty} a_n^{(b;1;1)}\left(\frac{\hat{t}_0^2}{\hat{t}^2}-1\right)^n + \frac{1}{\hat{t}^2}\sum_{n=0}^{\infty} a_n^{(b;1;2)}\left(\frac{\hat{t}_0^2}{\hat{t}^2}-1\right)^n \\ &+ e^{-2\hat{t}}\sum_{n=0}^{\infty} a_n^{(b;2;1)}\left(\frac{\hat{t}_0}{\hat{t}}-1\right)^n + \frac{e^{-2\hat{t}}}{\sqrt{\hat{t}}}\ln(\hat{t})\sum_{n=0}^{\infty} a_n^{(b;2;2)}\left(\frac{\hat{t}_0}{\hat{t}}-1\right)^n \\ &+ \frac{e^{-2\hat{t}}}{\sqrt{\hat{t}}}\sum_{n=0}^{\hat{t}} a_n^{(b;2;3)}\left(\frac{\hat{t}_0}{\hat{t}}-1\right)^n .\end{aligned} \tag{4.77}$$

At this point we could use the expansions for small and for large $\hat{t}$ to derive the values of $\tilde{f}_4(t)$ for any value of $\hat{t}$.

We chose a point of separation $\hat{t} = \hat{t}_s$. In the region $\hat{t} \leq \hat{t}_s$ we computed $\tilde{f}_4(t)$ from the small-t expansion (4.22). In the region $\hat{t} > \hat{t}_s$, we chose a suitable value of $\hat{t}_0$ and used (4.77) to compute $\tilde{f}_4(t)$.

The choice of the optimal $\hat{t}_s$, $\hat{t}_0$, and the numbers of terms of the expansion depend on the level of precision required. We selected $\hat{t}_s = 3.82$ and $\hat{t}_0 = 5$. In table B.2 (from [128]) in appendix B we list the coefficients of the expansion (4.77) up to $n = 12$. These values allow to obtain $\tilde{f}_4(t)$ with a precision $< 3 \times 10^{-8}$ for any value of $\hat{t} \geq 0$. In Fig.4.2 we show the error of this approximation.

Chapter 5

Light-quark Yukawa couplings from off-shell Higgs production

In this chapter, we address the challenge of constraining the Yukawa couplings of the first quark generation, which are notoriously difficult to determine due to their small values within the Standard Model. To overcome this difficulty, we propose a novel approach using Higgs off-shell production, where the Higgs boson decays into four leptons.

5.1 The Higgs boson in the Standard Model

The discovery of the Higgs boson in 2012 [55, 56] marked a significant milestone in particle physics. Its existence had been predicted decades earlier, and its discovery confirmed the Standard Model (SM) of particle physics as a remarkably successful theory in describing the fundamental building blocks of our universe. The ATLAS and CMS experiments extensively studied the Higgs characterization including its general properties [134]-[141], cross-sections [142]-[145], and couplings to electroweak and heavier fermions [146, 147].

The SM is a gauge theory characterized by a local $\mathrm{SU(3)_C} \times \mathrm{SU(2)_L} \times \mathrm{U(1)_Y}$ gauge group [57]-[60]. The $\mathrm{SU(3)_C}$ symmetry governs Quantum Chromodynamics (QCD), giving rise to gluons as the associated gauge bosons. On the other hand, the electroweak (EW) gauge group $\mathrm{SU(2)_L} \times \mathrm{U(1)_Y}$ unifies the weak and electromagnetic forces. The theoretical foundation of the SM involves the construction of a Lagrangian based on fundamental symmetry principles. For instance gauge invariance forbids explicit mass terms for gauge bosons. Experimental observations have though confirmed that three of the electroweak gauge bosons acquire mass, despite being theoretical forbidden. The solution lies in the Higgs mechanism, which introduces a complex $\mathrm{SU(2)_L}$ doublet ϕ characterized by a potential expressed as follows:

$$-V = \mu^2 \phi^\dagger \phi - \lambda \left(\phi^\dagger \phi\right)^2 . \tag{5.1}$$

A non-zero minimum of the potential can occur at $\langle \phi^\dagger \phi \rangle = v^2/2 = \mu^2/(2\lambda)$ for $\lambda > 0$ and $\mu^2 > 0$. The VEV, denoted as v, induces spontaneous symmetry breaking within the

framework of $\mathrm{SU(2)_L \times U(1)_Y}$ symmetry to the $\mathrm{U(1)_{em}}$ symmetry of quantum electrodynamics (QED). The VEV v, can be intentionally oriented in a manner that permits the expansion of the Higgs doublet ϕ, and this expansion can be expressed as follows

$$\phi = \begin{pmatrix} \theta_2 + i\theta_1 \\ \frac{1}{\sqrt{2}}(v+h) - i\theta_3 \end{pmatrix} = e^{i\theta_a \frac{\tau_a}{v}} \frac{1}{\sqrt{2}} \begin{pmatrix} 0 \\ v+h \end{pmatrix}, \tag{5.2}$$

where θ_1, θ_2, θ_3 and h denote four real fields and τ_a are the $\mathrm{SU(2)_L}$ generators. The three degrees of freedom θ_a with $a = 1, ..., 3$ play the role of Goldstone bosons and can be reabsorbed by an unitary transformation. In the unitary gauge, they will correspond to the longitudinal degrees of freedom of the massive gauge bosons. Thus, the field becomes

$$\phi = \frac{1}{\sqrt{2}} \begin{pmatrix} 0 \\ v+h \end{pmatrix}. \tag{5.3}$$

Only one physical degree of freedom is left over: the Higgs boson h. In the unitary gauge, the Higgs Lagrangian is

$$\mathcal{L}_h = (D_\mu \phi)^\dagger (D^\mu \phi) - V, \tag{5.4}$$

where

$$D_\mu \phi = \left(\partial_\mu - i g_2 W_\mu^a \tau^a - i \frac{1}{2} g_1 B_\mu \right) \phi, \tag{5.5}$$

which is characterized by the $\mathrm{U(1)_Y}$ gauge field B_μ and the $\mathrm{SU(2)_L}$ gauge fields W_μ^a with $a = 1, ..., 3$. The corresponding gauge couplings are denoted by g_1 and g_2, respectively. Substituting ϕ with the expression from Eq. (5.3) in $\mathcal{L}_h$, we observe the emergence of bilinear terms in the gauge fields. These terms are characterized by coefficients corresponding to the gauge boson mass squared. Furthermore, in Eq. (5.4), interaction terms between vector bosons and Higgs bosons become apparent. These interaction terms are directly proportional to the mass of the gauge boson.

Explicit mass terms for the fermions in the Lagrangian can be generated by Yukawa couplings

$$\mathcal{L}_y = -y_{ij}^u \bar{Q}_L^i \tilde{\phi} u_R^j - y_{ij}^d \bar{Q}_L^i \phi d_R^j - y_{ij}^e \bar{L}_L^i \phi e_R^j + \text{ h.c. }, \tag{5.6}$$

once ϕ acquires a non-zero VEV. The $\mathrm{SU(2)_L}$ quark doublet is referred to as Q_L, the $\mathrm{SU(2)_L}$ lepton doublet as L_L, the right-handed up-type fermions as u_R, the down-type fermions as d_R, and the right-handed leptons as e_R. The Higgs boson h itself possesses mass, and its mass is uniquely related to the parameter λ of the Higgs potential through the equation $M_h^2 = 2\lambda v^2$. Consequently, by measuring M_h, all previously unknown parameters of the SM Higgs potential become determined. Presently, the ATLAS collaboration has measured the Higgs boson mass as $125.5 \pm 0.2 \pm 0.6$ GeV [148], and CMS has reported a mass of $125.7 \pm 0.3 \pm 0.3$ GeV [149].

One decade after the discovery of the Higgs boson, several challenges must still be addressed in order to fully understand the properties of this particle. As we already said in Chapter 1, the measurements of the couplings between the Higgs boson and vector boson, or third generation fermions, are in a good agreement with their SM prediction. This is not the case for the Yukawa couplings to the first and second generation quarks.

We have seen that the determination of the light-quark Yukawa couplings is based on a model-dependent global fit on the Higgs untagged branching ratio [71].

There exist various proposals on how to constrain the light Yukawa couplings from measurements of specific processes. For instance, the Higgs boson coupling to the charm quark has been constrained to be smaller than 8.5 times its SM value [150, 151] by looking at associated Vh production[1] with subsequent decay of the Higgs boson to charm quarks [153]. Also exclusive Higgs decays to vector mesons [154]-[157] have been used to constrain the charm Yukawa coupling [158, 159]. Other proposals include Higgs+charm production [160], using the change in the Higgs p_T-spectrum from enhanced charm-quark loops [161] or $VVcj$ production [162]. Constraining the strange Yukawa coupling is extremely challenging, but at a future e^+e^- collider one might reach SM sensitivity if strange tagging is employed [163].

These ideas are mostly based on the Higgs decays. Since Higgs decays to light quarks cannot be measured directly, for the first quark generation one needs to proceed in a different manner. For enhanced light quark Yukawa couplings we can use the fact that a significant contribution of Higgs production can come from diagrams where the Higgs boson couples directly to the quark content of the parton distributions. Interesting processes that can be used to constrain the light quark Yukawa couplings in this way are Higgs+photon [164], Higgs+jet [165, 166], Higgs pair production [167, 168], tri-vector boson production in the high-energy limit [160, 169] and the charge asymmetry in $W^{\pm}h$ [170, 171].

A direct determination of the Higgs total width [172]-[174] is not possible at the LHC, therefore, as a probe, the off-shell Higgs measurement is usually considered in combination with an on-shell measurement. In particular, the Higgs width can be indirectly constrained by the ratio of on- and off-shell signal strengths

$$\begin{aligned} \mu_{\rm on} &\equiv \frac{\sigma_h \times {\rm BR}(h \to ZZ \to 4\ell)}{[\sigma_h \times {\rm BR}(h \to ZZ \to 4\ell)]_{\rm SM}} \sim \frac{\kappa_{ggh}^2 \kappa_{hZZ}^2}{\Gamma_h/\Gamma_h^{\rm SM}} \\ \mu_{\rm off} &\equiv \frac{{\rm d}\bar{\sigma}_h}{[\,{\rm d}\bar{\sigma}_h]_{\rm SM}} \sim \kappa_{ggh}^2(\hat{s}) \kappa_{hZZ}^2(\hat{s}) \end{aligned} \tag{5.7}$$

$$\frac{\mu_{\rm on}}{\mu_{\rm off}} \propto \frac{\kappa_{ggh}^2(m_h)\kappa_{hZZ}^2(m_h)}{\Gamma_h/\Gamma_h^{\rm SM}} \frac{1}{\kappa_{ggh}^2(m_{4\ell})\kappa_{hZZ}^2(m_{4\ell})}\,, \tag{5.8}$$

where κ_i with $i = ggh, hZZ$ are the coupling modifiers with respect to the SM value and Γ_h is the Higgs width. The invariant mass of the four-lepton pair is denoted by $m_{4\ell}$, the Higgs mass by m_h. Under the limitation that, the effective coupling of the Higgs to gluons and the coupling of the Higgs to Z bosons at different energy scales are correlated in a predictable way [175, 176], the Higgs width can be extracted. The CMS collaboration has recently measured Γ_h to be $3.2^{+2.4}_{-1.7}$ MeV [73] employing this method; ATLAS obtained $4.5^{+3.3}_{-2.5}$ MeV [74]. Both measurements are in agreement with the SM value.

In the presence of enhanced light-quark Yukawa couplings, the previous method of constraining the Higgs width becomes more complicated. The enhanced couplings lead

[1] Vh production followed by the Higgs decay to two jets has been studied as a probe of light Yukawa couplings in Ref. [152].

to an increase in the Higgs total width, and an additional factor needs to be considered: the production of a Higgs boson directly from light-quark fusion. The introduction of this extra production channel raises questions about the assumption made in the ratio of the on- and off-shell signal strengths in Eq. (5.8), and hence its interpretation in terms of a measurement of the Higgs total width. In this work, we will instead make use of the kinematic properties of the off-shell Higgs measurement to set bounds on the light-quark Yukawa couplings.

5.2 Light Yukawa couplings in Effective Field Theory

The Higgs couplings to quarks in the SM are described by the Lagrangian in Eq. (5.6). New physics beyond the SM may be hidden in the experimental errors of measurements that are becoming increasingly accurate at the LHC. Such phenomena can be parametrized in terms of the so-called SM Effective Field Theory (SMEFT) [177]-[179], where, assuming Λ to be the typical energy scale of the SM extension, the observable effects are suppressed by powers of the expansion parameter v/Λ and the Higgs field transforms as a SM doublet. A complete basis of higher-dimensional operators has been given in Refs. [180, 181]. In this work we are interested only in an enhancement of the light-quark Yukawa couplings. We hence do not consider operators that require a redefinition of the Higgs field and that lead to a general shift of the Higgs couplings, as they cannot render the light-quark Yukawa couplings sufficiently larger and at the same time obey the limits on other Higgs couplings.

In the SMEFT, new flavour structures can be introduced through dimension-six operators that contain flavour indices. Especially, the couplings of the quarks are modified by the operator

$$\Delta\mathcal{L}_y = \frac{\phi^\dagger\phi}{\Lambda^2}\left((C_{u\phi})_{ij}\bar{Q}_L^i\tilde{\phi}u_R^j + (C_{d\phi})_{ij}\bar{Q}_L^i\phi d_R^j + \text{ h.c. }\right), \tag{5.9}$$

with $i,j = 1,...,3$ and Λ denotes the cut-off of the effective field theory (EFT). Here u and d refer to the up- and down-type sectors respectively, and not the quarks themselves. Therefore the mass matrices of the up-type and down-type quarks obtained from the Yukawa and the new SMEFT couplings are

$$\begin{aligned} M_{ij}^u &= \frac{v}{\sqrt{2}}\left(y_{ij}^u - \frac{1}{2}(C_{u\phi})_{ij}\frac{v^2}{\Lambda^2}\right), \\ M_{ij}^d &= \frac{v}{\sqrt{2}}\left(y_{ij}^d - \frac{1}{2}(C_{d\phi})_{ij}\frac{v^2}{\Lambda^2}\right). \end{aligned} \tag{5.10}$$

Due to the modification of the mass matrix, the rotation matrices transforming quark wavefunctions to the mass eigenbasis will be modified with respect to the SM ones. Mass matrices are diagonalized by a new set of bi-unitary transformations

$$m_{q_i} = \left(\left(V_L^{u/d}\right)^\dagger M^{u/d} V_R^{u/d}\right)_{ii}, \tag{5.11}$$

in which the CKM matrix is defined as $V_{\rm CKM} = (V_L^u)^\dagger V_L^d$. We can rewrite $(C_{q\phi})_{ij}$ in terms of $(\tilde{C}_{q\phi})_{ij}$ which are now in the mass eigenbasis

$$(\tilde{C}_{q\phi})_{ij} = (V_L^q)^*_{ni} (C_{q\phi})_{nm} (V_R^q)_{mj} , \qquad \text{with} \quad q = u, d . \tag{5.12}$$

Therefore the Lagrangian containing the couplings of the Higgs boson to quarks is

$$\mathcal{L} \supset g_{hq_i\bar{q}_j} \bar{q}_j q_i h + g_{hhq_i\bar{q}_j} \bar{q}_j q_i h^2 + g_{hhhq_i\bar{q}_j} \bar{q}_j q_i h^3 \tag{5.13}$$

with

$$g_{hq_i\bar{q}_j} = \frac{m_q}{v}\delta_{ij} - \frac{1}{\sqrt{2}}\frac{v^2}{\Lambda^2}(\tilde{C}_{q\phi})_{ij} , \quad g_{hhq_i\bar{q}_j} = -\frac{3}{2\sqrt{2}}\frac{v}{\Lambda^2}(\tilde{C}_{q\phi})_{ij} , \quad g_{hhhq_i\bar{q}_j} = -\frac{1}{2\sqrt{2}}\frac{1}{\Lambda^2}(\tilde{C}_{q\phi})_{ij} , \tag{5.14}$$

where $i, j = 1, \ldots, 3$ are generation indices. An important feature of this parametrisation is that the NP effects encoded in $(\tilde{C}_{q\phi})_{ij}$ are kept separate from the contribution due to the quark mass in the first of Eqs. (5.14). Therefore, the coupling of the Higgs boson to quarks can receive large enhancements even if the quark kinetic masses are small. For later use, we give also the coupling of quarks to two neutral Goldstone bosons

$$g_{G_0G_0q_i\bar{q}_j} = -\frac{1}{2\sqrt{2}}\frac{v}{\Lambda^2}(\tilde{C}_{q\phi})_{ij} . \tag{5.15}$$

As we will see later, employing the Goldstone boson equivalence theorem for the off-shell Higgs measurement we can observe a similar behaviour as in Higgs pair production [167, 168], which motivates the study of light Yukawa couplings in this context.

Finally, we introduce here another convenient notation for the coupling of the Higgs boson to quarks, based on the "kappa"-framework (see e.g. [71]). This notation is valid only for the diagonal couplings and does not allow for new Lorentz structures with respect to the SM ones:

$$g_{hq\bar{q}} = \kappa_q \frac{m_q}{v} . \tag{5.16}$$

We define the reference mass values $m_u = 2.2$ MeV and $m_d = 4.7$ MeV as constant, i.e. not running, values. In the rest of the work, we will often use κ values when quoting sensitivity limits, as this is often more intuitive with respect to the theoretically well-defined SMEFT approach. The given values need though always to be understood with respect to the reference mass values. We remark that the limits on κ_q values can be directly translated to limits on the SMEFT coefficients $\tilde{C}_{q\phi}/\Lambda^2$ $(q = u, d)$ using Eq. (5.14) and Eq. (5.16), and that the two notations that we have introduced are equivalent.

We finally shortly comment on models that can achieve large deviations in the light-quark Yukawa couplings. Large deviations can be implemented using an aligned flavour assumption, as new sources of flavour violation are constrained to the level $|(\tilde{C}_{u\phi/d\phi})_{12}| < 10^{-5}\Lambda^2/v^2$ $|(\tilde{C}_{u\phi/d\phi})_{13}| < 10^{-4}\Lambda^2/v^2$ by $\Delta F = 2$ transitions [182, 183]. From an EFT perspective there is no inherent reason to prohibit the implementation of an aligned flavor structure. The renormalization group flow in EFT can introduce flavor-changing couplings, but these are typically suppressed by several mass insertions, making them strongly suppressed for the first generation of particles [184]. The possibility of implementing an aligned flavor assumption mainly depends on the specific ultraviolet (UV)

model that is being considered. In some concrete UV models, large deviations in the light-quark Yukawa couplings at the electroweak scale can be realized while still preserving the aligned flavor structure. In a simplified model approach, an effective $|\phi|^2\bar{Q}_L\phi d_R$ or $|\phi|^2\bar{Q}_L\tilde{\phi}u_R$ operator can be generated by various fields, e.g. vector-like fermions, new scalars and new vector bosons and combinations thereof. Concrete models have been presented in Refs. [185]-[187]. In the subsequent analysis, we will refrain from using concrete models but note that those models will at the same time generate other effective operators, which possibly can be constrained better than the light-quark Yukawa couplings.

5.3 The on-shell Higgs

As stated in the introduction of this chapter, an indirect determination of the total decay width of the Higgs boson can be extracted from a comparison of off-shell and on-shell measurements. In this section, we will briefly examine the impact of enhanced light Yukawa couplings on the on-shell Higgs production, with a specific focus on the subsequent decay of the Higgs boson into a pair of Z bosons. To simplify the analysis, we will disregard the treatment of the leptonic decays of the Z bosons since these decays are not influenced by the contributions from NP that we are studying. In the case of on-shell Higgs production, we use the narrow width approximation to express the cross section as the product of the Higgs cross section and the $h \to ZZ$ branching ratio

$$\sigma(pp \to h \to ZZ) = \sigma(pp \to h) \cdot \mathrm{BR}_{ZZ}, \tag{5.17}$$

and we consider the effects of modified light-quark Yukawa couplings in each contribution of the r.h.s. of Eq. (5.17).

In the SM, the dominant partonic channel for Higgs boson production at the LHC is the gluon fusion (ggF) process, primarily mediated through quarks of the third generation (the top/bottom interference amounts to about 10%). However, when we allow the light-quark Yukawa couplings to exceed their SM values (as is the case in scenarios with enhanced light-quark Yukawa couplings), new relevant contributions can arise via loops involving first- and second-generation quarks. In addition, a new partonic channel must be considered for Higgs production, namely $q\bar{q}$ annihilation, $q\bar{q} \to h$. In our study we computed the ggF cross section at leading order (LO) and we used a K-factor to account for the N^{3}LO QCD corrections [188, 189] by rescaling the LO result. We observed that the effects of modified first-generation Yukawa couplings, stemming from the top and light-quark interference, are below the level of 0.1% for $|\kappa_d| \lesssim 1200$ and $|\kappa_u| \lesssim 4500$, therefore we consider them negligible[2], both in this section and in the following one.

On the other hand, the $q\bar{q} \to h$ production channel gains increasing significance when dealing with enhanced first-generation Yukawa couplings. In such scenarios, the partonic cross section experiences a quadratic enhancement with a factor κ_q. This enhancement can effectively counterbalance the suppression originating from the lower quark luminosities compared to the ggF channel. By examining Figure 5.1a, it becomes evident that

[2]The modification of the strange Yukawa coupling can reach an effect of 3% on the ggF cross section for $|\kappa_s| = 200$, while an enhancement of the charm Yukawa coupling by $|\kappa_c| = 20$ leads to a change of about 18%.

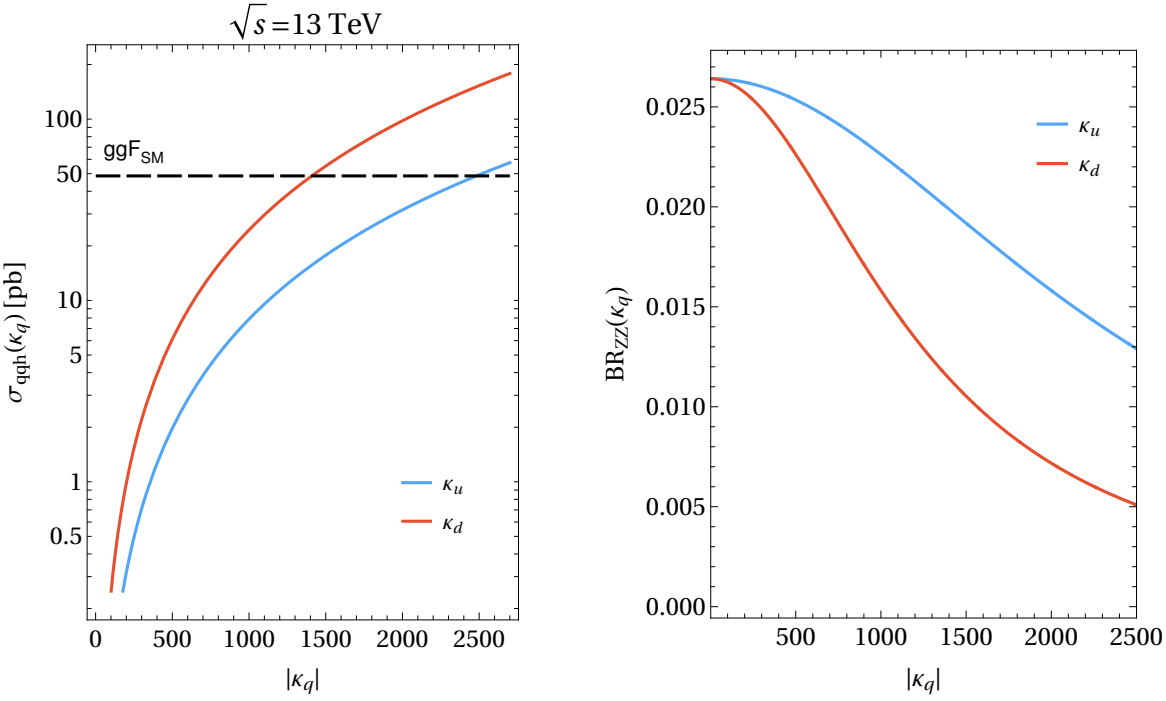

Figure 5.1: (a) Modification of the cross section for resonant $q\bar{q} \to h$ production, as a function of the light-Yukawa coupling modifier κ_q. The cross section for the gluon-fusion channel in the SM [188] is shown as a black dashed line. (b) Branching ratio for the $h \to ZZ$ decay as a function of κ_q for the first quark generation. Figure taken from [190].

for values of κ_d (κ_u) that exceed around 1400 (2500), the $q\bar{q} \to h$ mode becomes the predominant mechanism for Higgs production at the 13 TeV LHC. Parallel to the ggF production, we employed a K-factor to adjust the LO cross section in order to incorporate the NLO QCD corrections. The specific value of $K^{\text{NLO}}_{q\bar{q}h} = 1.4$ was obtained for $q\bar{q}h$ production by adapting the QCD correction calculation applied to $b\bar{b} \to h$, as outlined in Refs. [191]-[193].

Lastly, the final component to be incorporated into our on-shell prediction is the modified ZZ branching ratio, denoted as $\text{BR}_{ZZ}(\kappa_q)$. Since in our scenario we will not consider electroweak corrections, we used `HDECAY` [194, 195] to verify that the impact of large values of κ_q on the partial width $\Gamma(h \to ZZ)$ due to higher-order corrections is negligible. Simultaneously, when considering large values of κ_q, the total decay width, $\Gamma_h^{\text{BSM}}(\kappa_q)$, experiences a significant increase. This effect is particularly pronounced in the case of an enhanced κ_q coupling, as the Higgs decay channels involving the first-generation quarks become more relevant. The partial width of these decay channels can be expressed simply by scaling the corresponding SM width by a factor of κ_q^2. We then have

$$\Gamma_h^{\text{BSM}}(\kappa_q) = \Gamma_h^{\text{SM}} + \kappa_q^2\, \Gamma^{\text{SM}}(h \to q\bar{q}) \qquad (q = u, d), \tag{5.18}$$

with $\Gamma_h^{\text{SM}} = 4.1$ MeV [196]. As a direct outcome of the Eq. (5.18), the branching ratio of $h \to ZZ$ experiences a reduction as the value of κ_q increases. In Figure 5.1b, we

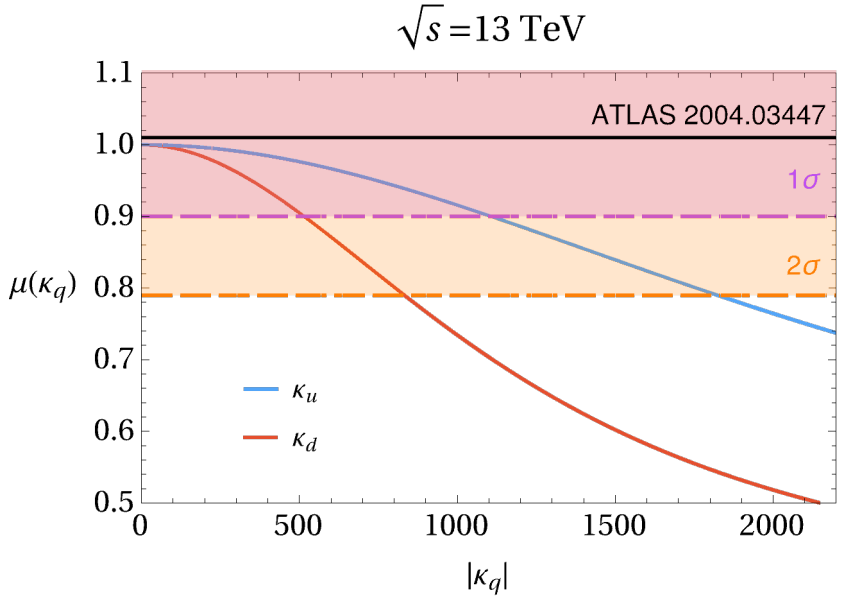

Figure 5.2: Signal strengths for resonant Higgs production as a function of κ_q. The current measurement from ATLAS [197] is shown as a reference (black line), including the 1 and 2 σ uncertainty bands. Figure taken from [190].

present the variations in the $\mathrm{BR}_{ZZ}(\kappa_q)$ branching ratio. The modifications are depicted separately for the enhancement of the down-type Yukawa couplings (illustrated in red) and the up-type Yukawa couplings (depicted in blue).

We can now study the effect of the combination of all the ingredients discussed above for on-shell production, and we compare them to the SM case in fig. 5.2, where we plot the signal strength

$$\mu(\kappa_q) = \frac{[\sigma(gg \to h)(\kappa_q) + \sigma(q\bar{q} \to h)(\kappa_q)] \cdot \mathrm{BR}_{ZZ}(\kappa_q)}{\sigma(gg \to h)_{\mathrm{SM}} \cdot \mathrm{BR}_{ZZ\ \mathrm{SM}}} \tag{5.19}$$

defined as the ratio of the NP on-shell production cross section, multiplied by the modified $h \to ZZ$ branching ratio, over the SM prediction (in which we omit the negligible $q\bar{q}$-initiated contribution). Assuming that the only modification arising from NP is the individual enhancement of the down-type (up-type) Yukawa coupling, we can draw important conclusions from a comparison with the most recent ATLAS on-shell measurement [197]. Specifically, the analysis enables us to exclude certain parameter values. In this case, considering a 2σ confidence level, we find that values of $\kappa_d \gtrsim 850$ ($\kappa_u \gtrsim 1850$) are excluded. It's noteworthy that these constraints are approximately a factor of three weaker compared to the projected limits that can be anticipated from a global fit at a HL-LHC [71]. Furthermore, as the enhancement via κ_q has an impact both on the production cross section and on the decay width of the Higgs boson, the interplay of the two effects spoils the interpretation of Eq. (5.8) as an indirect measurement of Γ_h. In conclusion, it is important to highlight that on-shell measurements present limitations when it comes to serving as a model-independent tool for probing the Yukawa couplings of the first-generation quarks. The limits obtained from on-shell measurements are predicated on a

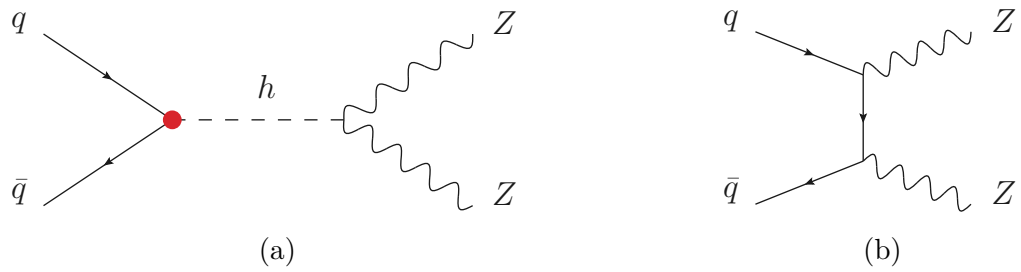

Figure 5.3: Feynman diagrams contributing to $q\bar{q} \to ZZ$: (a) Higgs-mediated process, with the red dot indicating a modified light Yukawa coupling; (b) $\hat{t}$-channel diagram for the dominant production mode.

robust assumption of modifications solely in the light-quark Yukawa couplings. However, any alterations, such as shifts in the Higgs coupling to Z bosons, would introduce complexities that undermine the straightforward interpretation of the on-shell measurements. Therefore in the rest of this work we move our attention to off-shell production.

5.4 The off-shell Higgs

In the context of off-shell Higgs production, the utilization of the narrow width approximation, as employed in Eq. (5.17), is no longer applicable. Therefore, in this section, we need to reevaluate the theoretical prediction for the process $pp \to ZZ$ without relying on the narrow width approximation. Additionally, we will explore how this prediction is influenced by an enhancement of the first-generation Yukawa couplings.

References [167, 168] have highlighted the possibility of constraining light-quark Yukawa couplings through the process of Higgs pair production. In this case, the constraint primarily arises from the effective coupling between the light quarks and two Higgs bosons, which emerges from the presence of operators characterized by Wilson coefficients $C_{u\phi}$ or $C_{d\phi}$, corresponding to up-type and down-type quarks respectively. Via the Goldstone boson equivalence theorem, the production of longitudinal Z boson pairs will be driven by an effective coupling of two Goldstone bosons to two fermions, in the same way that the effective interaction between the light quarks and two Higgs bosons is relevant for di-Higgs production. This holds especially in the off-shell region. The partonic differential cross section for the production of two neutral Goldstone bosons in the limit of large partonic centre-of-mass energy $\hat{s}$ is given by

$$\frac{d\hat{\sigma}_{q_i\bar{q}_j}}{d\hat{t}} = \frac{1}{16\pi}\frac{1}{3\hat{s}} g^2_{G_0 G_0 q_i q_j} \,. \tag{5.20}$$

The cross section governing quark-initiated off-shell Higgs production is expected to serve as a promising avenue for investigating light-quark Yukawa couplings. This cross section exhibits a behavior analogous to that observed in the Higgs pair production process. This intriguing similarity motivates an exploration of the implications of light-quark Yukawa couplings within the context of off-shell Higgs measurements. Furthermore, we make use of the differences in the kinematics of the process with respect to the SM one.

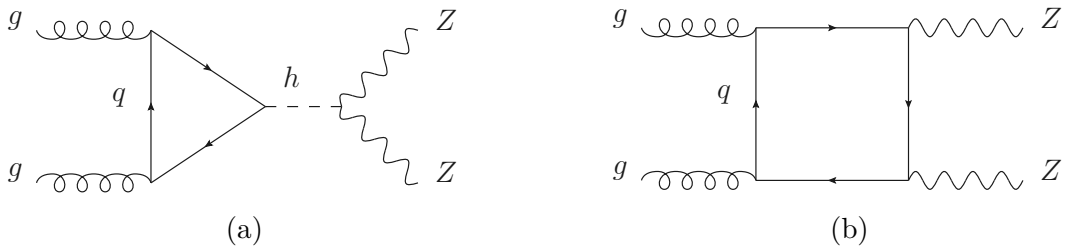

Figure 5.4: The two topologies for the Feynman diagrams occuring in the LO contribution to $gg \to ZZ$: (a) triangles associated to the Higgs-mediated process; (b) boxes associated to continuum production.

Parallel to the observations made in the preceding section, the enhancement of the light Yukawa couplings implies that the quark-fusion channel mediated by the Higgs boson (as depicted in Fig. 5.3a) becomes a significant factor to consider in the context of off-shell Higgs production. The LO partonic differential cross section for $q\bar{q} \to h^* \to ZZ$ is given by

$$\frac{d\hat{\sigma}_{q_i\bar{q}_j}}{d\hat{t}} = g^2_{hq_i\bar{q}_j} \frac{1}{16\pi} \frac{1}{12\hat{s}} \frac{1}{v^2} \frac{1}{(\hat{s}-m_h^2)^2} \left[12m_Z^4 - 4m_Z^2\hat{s} + \hat{s}^2\right], \tag{5.21}$$

which in the limit of large $\hat{s}$ corresponds to Eq. (5.20). From this the hadronic cross section can be obtained by

$$\sigma_{\text{hadronic}} = \int_{\tau_0}^{1} d\tau \int_{\hat{t}_-}^{\hat{t}_+} d\hat{t} \sum_{i,j} \frac{d\mathcal{L}^{q_i\bar{q}_j}}{d\tau} \frac{d\hat{\sigma}_{q_i\bar{q}_j}}{d\hat{t}}\,, \tag{5.22}$$

with $\tau_0 = 4\,m_Z^2/s$, $\hat{s} = \tau s$ and

$$\hat{t}_\pm = m_Z^2 - \frac{\hat{s}(1 \mp \beta)}{2} \qquad \text{and} \qquad \beta = \sqrt{1 - \frac{4m_Z^2}{\hat{s}}}\,. \tag{5.23}$$

The parton luminosity is given by

$$\frac{d\mathcal{L}^{q_i\bar{q}_j}}{d\tau} = \int_\tau^1 \frac{dx}{x} \left[f_{q_i}(\tau/x, \mu_F^2) f_{\bar{q}_j}(x, \mu_F^2) + f_{\bar{q}_j}(\tau/x, \mu_F^2) f_{q_i}(x, \mu_F^2)\right]. \tag{5.24}$$

We neglected all the kinematical masses of the light quarks, while the coupling of the Higgs boson to the light quarks (for flavour diagonal couplings) is given by Eq. (5.14) or Eq. (5.16).

Within the SM an off-shell Higgs boson is produced by gluon fusion, where a loop of third-generation quarks[3] couples to an off-shell Higgs boson, as in Fig. 5.4a. This process has large interference with box diagrams from *continuum* production, $gg \to ZZ$, see Fig. 5.4b. Using `FeynArts` [198], we computed the form factors for the gluon-fusion cross section at LO, checking the results with Ref. [199], to implement a Monte Carlo simulation

[3]We recall that we are neglecting the effect of a modified κ_q on the gluon-fusion channel.

with VEGAS algorithm [200] by which we derive the distribution in the invariant mass m_{ZZ} of $gg \to ZZ$ at LO, including the Higgs-mediated, the continuum and the interference contributions.

Finally, the main background to off-shell Higgs production is $q\bar{q} \to ZZ$ production, occurring via diagrams as shown in Fig. 5.3b. We computed the leading-order (LO) cross section for this background process and confirmed its consistency with the findings of Reference [201]. We note that there is no signal – background interference between the amplitudes for $q\bar{q} \to h^* \to ZZ$ and $q\bar{q} \to ZZ$. In particular, using the spinor-helicity formalism, one can observe that the $q\bar{q} \to h^* \to ZZ$ amplitude receives a non-zero contribution only when the (massless) fermions in the initial state have the same helicities, whereas for $q\bar{q} \to ZZ$ the initial fermions must have opposite helicities. For this reason the signal and the background processes are related to different helicity amplitudes, and cannot interfere. We remark that this helicity selection rule holds at higher perturbative orders, and that it is insensitive to the polarisation of the Z bosons in the final state, so that the interference cannot be *resurrected* e.g. by looking at the decay leptons of the Z bosons [202, 203]. However, the above reasoning does not automatically imply that, in the perturbative expansion of the SMEFT, we are considering purely BSM, $\mathcal{O}(1/\Lambda^4)$, effects. Indeed, the BSM/SM interference is already contained in the square of $g_{hq_i\bar{q}_j}$ in Eq. (5.21), which in fact includes both $\mathcal{O}(1/\Lambda^2)$ and $\mathcal{O}(1/\Lambda^4)$ contributions (see Eq. (5.14)). Still, the $\mathcal{O}(1/\Lambda^2)$ interference is very small because of the smallness of the light quark masses in the SM, and in the rest of this work we will neglect it. We note that the fact that our bound is dominated by $\mathcal{O}(1/\Lambda^4)$ effects does not invalidate the analysis given that a potential contribution of a dimension-8 operator would again be suppressed by the small quark masses.

5.5 Phenomenological analysis

In the following we analyse the sensitivity of the HL-LHC on the light-quark Yukawa coupling modifications from measurements of off-shell Higgs production. We consider specific signal processes: $d\bar{d} \to h^* \to ZZ \to 4\ell$ and $u\bar{u} \to h^* \to ZZ \to 4\ell$, where the enhanced Yukawa couplings for down-type and up-type quarks are respectively applied. As for background processes, we incorporate contributions from gluon fusion and the quark-induced ZZ production. Throughout our study, we focus on the scenario involving on-shell Z bosons, which accurately represents the process when the invariant mass of the Z boson pair significantly exceeds the kinematic threshold [204]. To ensure the reliability of this description, we implement a selection criterion by imposing a cut of $m_{ZZ} > 250$ GeV. In order to account for the impact of fundamental selection requirements, such as minimum transverse momentum ($p_{T\ell}$) and pseudorapidity ($|\eta_\ell|$) thresholds on the leptons, we utilize efficiency factors. These factors are computed using MadGraph_aMC@NLO [205] and are employed to reproduce the effects of the cuts $p_{T\ell} > 10$ GeV and $|\eta_\ell| < 2.5$.

In our analysis, we employ the LO matrix elements introduced in Sec. 5.4 as a starting point, but we improve them by incorporating K-factors. Currently, the background process involving four-lepton production through quark-antiquark ($q\bar{q}$) annihilation has been calculated at next-to-next-to-leading order (NNLO) [206]-[208]. To incorporate these

higher-order corrections, we introduce a K-factor, defined as $K = \sigma_{NNLO}/\sigma_{LO} = 1.6$. For the signal processes, the NLO QCD corrections can be inferred from $b\bar{b}h$ production [191]-[193]. We find $K^u = 1.47$ and $K^d = 1.63$ for the up- and down-initiated channels for a scale choice of $\mu_R = \mu_F = M_{ZZ}/2$. The gluon-fusion contribution is fully known only at LO [209, 210]. The NLO QCD corrections to the Higgs-mediated diagrams [211]-[213] and to the continuum production via loops of massless quarks [214, 215] are known in analytic form; the two-loop diagrams mediated by top-quark loops have been computed numerically in Refs. [216, 217] but they are still not included in a full NLO prediction. We use a $K = 1.83$ for the gluon fusion background following the estimate in Refs. [218, 219]. We use the `NNPDF40_lo_as_01180` parton distribution functions [220] and $\sqrt{s} = 14$ TeV.

In Fig. 5.5, we present the distribution of invariant masses for both signal and background processes. For the signal, we have chosen specific values of $\kappa_u = \kappa_d = 1000$, which correspond to modified couplings $\tilde{C}_{u\phi} = 0.21$ and $\tilde{C}_{d\phi} = 0.45$, assuming a NP scale fixed at $\Lambda = 1$ TeV. While the $q\bar{q}$ background is about two orders of magnitude larger than the signal, we can see that the latter contribution wins relative importance over the gluon-fusion background in the high invariant mass bins. This phenomenon is a consequence of both the κ_q enhancement and the distinct manner in which the quark parton distribution functions (PDFs) fall in comparison to the gluon one. Furthermore, the presence of destructive interference between the amplitudes associated with Higgs-mediated and continuum processes in ggF at elevated invariant masses contributes to an enhancement of the $q\bar{q}$ signal in relation to the ggF background. A direct comparison of Figs. 5.5a and 5.5b illustrates this effect.

In the pursuit of measuring the Higgs boson's width, kinematic discriminants rooted in the matrix element method have proven to be very powerful [73, 174, 221]. While the matrix element method is usually complicated by the fact that it requires the knowledge of a transfer function that describes the transfer of an event with parton-level momentum to an event with smeared detector-level momentum, for the off-shell Higgs analysis these terms cancel for the clean four-lepton final state when employing discriminants based on ratios of signal and background matrix elements. We define the weighted probability for an event initiated by the partons i, j, and with a fixed set v of kinematic variables, as

$$P_{ij}(v) = \frac{1}{\sigma_{ij\to 4\ell}} \int dx_1 dx_2 \delta(x_1 x_2 E^2_{CMS} - m^2_{4\ell}) f_i(x_1) f_j(x_2) \hat{\sigma}_{ij}(x_1, x_2, v)\,, \tag{5.25}$$

where f_i and f_j are the parton distribution functions, E_{CMS} is the collider energy and $\sigma_{ij\to 4\ell}$ is the hadronic cross section for the process initiated by i and j. We can then define the kinematic discriminants

$$D^d_s = \log_{10}\left(\frac{P^{sig}_{d\bar{d}}}{P^{back}_{q\bar{q}} + P^{back}_{gg}}\right) \qquad \text{and} \qquad D^u_s = \log_{10}\left(\frac{P^{sig}_{u\bar{u}}}{P^{back}_{q\bar{q}} + P^{back}_{gg}}\right). \tag{5.26}$$

We note that the dependence on the enhanced light-quark Yukawa couplings drops out in the respective definitions of $P^{sig}_{q\bar{q}}$.

5.5.1 Results based on D^d_s

In this section we will show our results for D^d_s. In Figure 5.6, we present the normalized

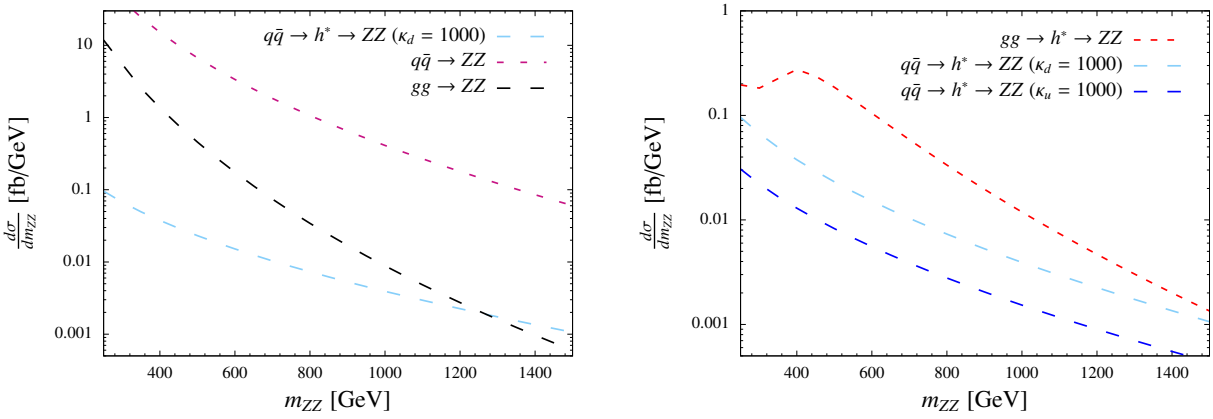

(a) (b)

Figure 5.5: Distribution in the invariant mass m_{ZZ} for the various ZZ production channels. (a) The $q\bar{q} \to ZZ$ SM background (violet), the $gg \to ZZ$ background (black) and the signal $d\bar{d} \to h^* \to ZZ$ (light blue) for a value $\kappa_d = 1000$, which corresponds to $\tilde{C}_{d\phi}/(1\ \text{TeV}^2) = 0.45$. (b) Comparison of the $gg \to h^* \to ZZ$ (triangle) contribution to the background with the $d\bar{d} \to h^* \to ZZ$ signal (light blue) and the $u\bar{u} \to h^* \to ZZ$ (dark blue) for $\kappa_u = 1000$ which corresponds to $\tilde{C}_{u\phi}/(1\ \text{TeV}^2) = 0.21$. Figure taken from [190].

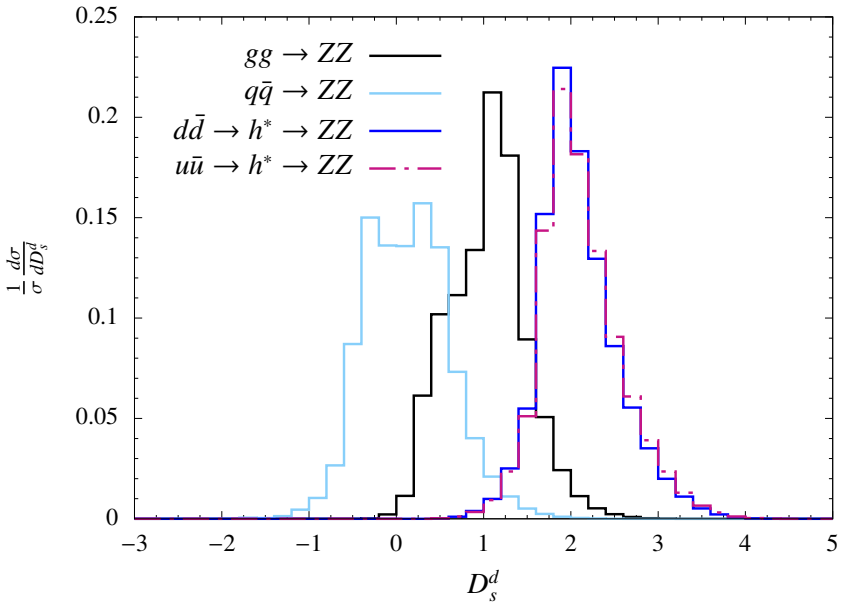

Figure 5.6: Normalised differential distributions with respect to D_s^d for signal (blue and pink dashed) and background (light blue and black) processes. Figure taken from [190].

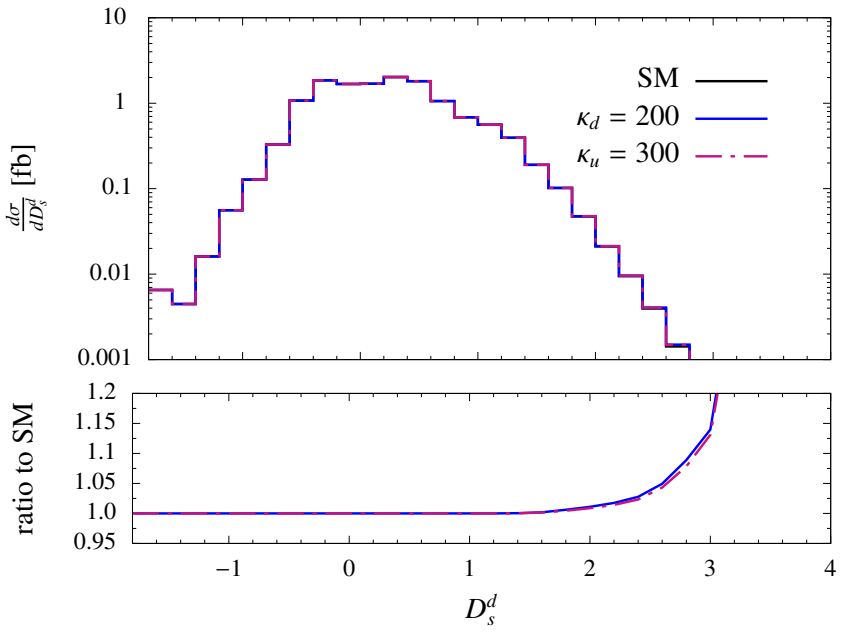

Figure 5.7: Distribution of the cross section of SM (black), SM+signal with $\kappa_d = 200$ (blue) and SM+signal with $\kappa_u = 300$ (pink dashed) as function of D_s^d. The lower panel shows the ratio to the SM. Taken from [190].

distribution of the signal processes $d\bar{d} \to h^* \to ZZ$ depicted as a blue line, and $u\bar{u} \to h^* \to ZZ$ shown as a pink dashed line. Additionally, the $gg \to ZZ$ background is displayed in black, while the $q\bar{q} \to ZZ$ background is illustrated in light blue. This visual representation clearly highlights the discriminating power of the D_s^d variable, primarily observed in bins where $D_s^d > 2$. This conclusion is reinforced by Fig. 5.7, where we compare the projected D_s^d distributions for the $pp \to ZZ \to 4\ell$ cross section in both the SM and the NP scenarios with $\kappa_d = 200$ and $\kappa_u = 300$. The $d\bar{d}$- and $u\bar{u}$-induced signals show instead very similar D_s^d distributions. Therefore, this process might not inherently differentiate between an amplified up or down Yukawa hypothesis. However, it's worth noting that this could be done in a global fit, using for instance also limits from $h\gamma$ where the up- and down-Yukawa contributions are distinguished due to the different quark charges [164]. We also explored the utilization of a kinematic discriminant as defined in the analysis presented in Ref. [222][4], and found that while it leads to slightly worse limits on the light-quark Yukawa couplings compared to our definition of D_s, it still shows very good discriminating power. The experimental analyses might hence be sensitive to similar order of magnitude modifications of light-quark Yukawa couplings compared to what we find in our study, without implementing a dedicated analysis.

To establish constraints on the light-quark Yukawa couplings, we undertake a shape analysis involving the D_s^d distributions. While we could in principle also include the m_{ZZ}

[4]While we find the same quantitative and qualitative behaviour of the thus defined D_s we find a shift on the x axis that we attribute to a different normalisation.

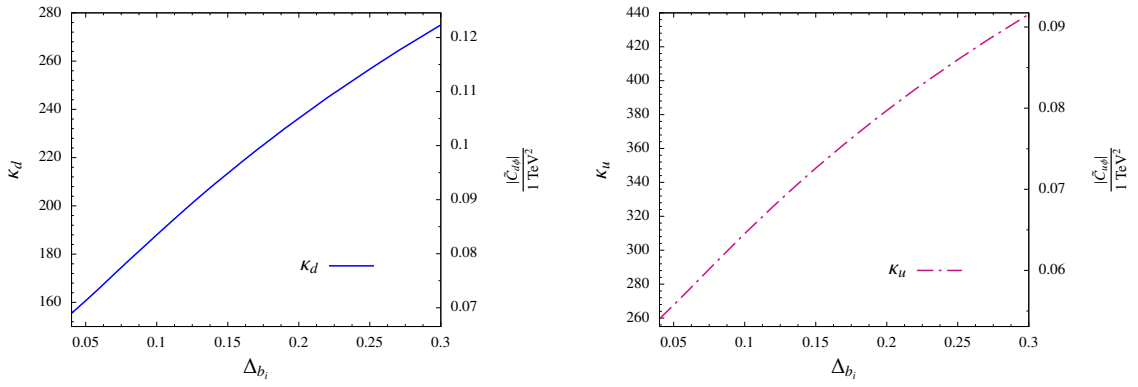

Figure 5.8: Dependence of the sensitivity bounds on κ_d ($\tilde{C}_{d\phi}$) in the left panel and κ_u ($\tilde{C}_{u\phi}$) in the right panel on the assumption made on the size of Δ_{b_i}. Figure taken from [190].

distribution in the analysis we found no difference doing so. To determine the significance within each bin, we calculate a Poisson ratio of likelihoods, which takes into account background uncertainties using the Asimov approximation [223]

$$Z_i = \sqrt{2\left[(s_i+b_i)\ln\frac{(s_i+b_i)(b_i+\sigma_{b_i}^2)}{b_i^2+(s_i+b_i)\sigma_{b_i}^2} - \frac{b_i^2}{\sigma_{b_i}^2}\ln\left(1+\frac{s_i\sigma_{b_i}^2}{b_i(b_i+\sigma_{b_i}^2)}\right)\right]}\,, \tag{5.27}$$

where s_i and b_i are respectively the number of signal and background events in the i-th bin. $\sigma_{b_i} = \Delta_{b_i} b_i$ denotes the standard deviation that characterises the (experimental and theoretical) uncertainties of the associated background in the bin. We assume a flat uncertainty and show in Fig. 5.8 the dependence of the sensitivity limit on κ_d and κ_u ($\tilde{C}_{d\phi}$ and $\tilde{C}_{u\phi}$) in dependence of Δ_{b_i}. Concerning our choice for the range of the plot, the lower limit is based on the total experimental systematic uncertainties expected for the $gg \to h^* \to ZZ$ signal strength, amounting to 5.0% and 3.9% in the baseline scenarios S1 and S2, respectively, as given by the ATLAS Collaboration [224]. The corresponding uncertainties of the CMS Collaboration are 7.3% and 4.1% [225]. Instead the upper limit $\Delta_{b_i} = 0.3$ corresponds to the approach advocated in Ref. [218], motivated by the observation that the scale uncertainties do not capture the difference between LO and K-factor improved prediction for $pp \to ZZ$. For this reason Ref. [218] proposed to take instead half of the difference between LO and K-factor improved prediction. Compared to the combination of scale and PDF+α_s uncertainty this approach leads to a much larger uncertainty and can hence be considered as very conservative.

We find that, assuming the optimistic scenario of $\Delta_{b_i} = 0.04$ at the HL-LHC, it is possible to obtain the following constraints

$$\begin{aligned} |\tilde{C}_{d\phi}|/(1\ \mathrm{TeV})^2 &< 0.069/\mathrm{TeV}^2 \quad (\kappa_d < 156), \\ |\tilde{C}_{u\phi}|/(1\ \mathrm{TeV})^2 &< 0.054/\mathrm{TeV}^2 \quad (\kappa_u < 260). \end{aligned}$$

In Fig. 5.9, we portray the dependence of the sensitivity limit on κ_d and κ_u on an upper

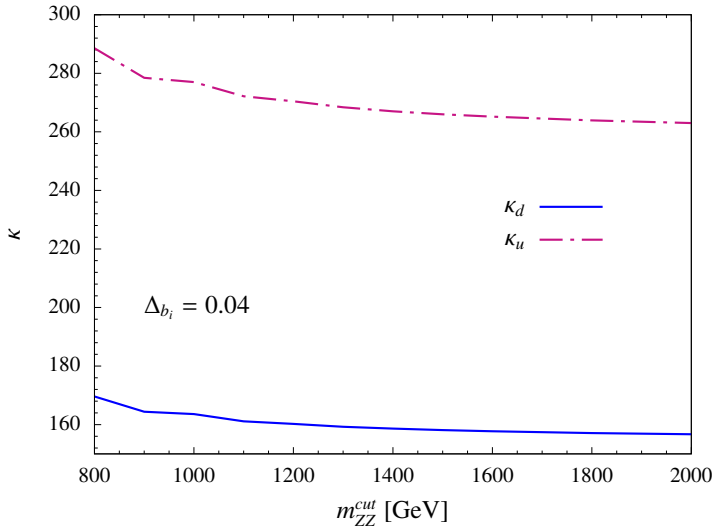

Figure 5.9: The projected sensitivity on κ_d (blue line) and κ_u (pink dashed line) as a function of an upper cut $m_{ZZ} < m_{ZZ}^{cut}$ using $\Delta_{b_i} = 0.04$. Figure taken from [190].

cut on the invariant ZZ mass, hence imposing $m_{ZZ} < m_{ZZ}^{cut}$, in order to check the validity of our EFT approach. This procedure of providing limits in terms of an upper cut on the energy probed, termed *clipping*, was suggested in Ref. [226]. We must underscore, particularly given the negligible impact of SM first-generation Yukawa couplings, that the sensitivity in our analysis on the coefficients $\tilde{C}_{u\phi}$ or $\tilde{C}_{d\phi}$ (or κ_d and κ_u) originates solely from the squared terms of the dimension-six contributions. Regarding Fig. 5.9, our assessment leads to the conclusion that the sensitivity of our analysis does not stem only from bins of high invariant mass, hence the utilization of the EFT approach appears well-justified.

5.5.2 Results based on D_s^u

In this section, we present the outcomes of our analysis incorporating the discriminant D_s^u, as defined in Eq.(5.26), as an alternative to D_s^d. In Fig. 5.10 we show the distribution of signal and background in D_s^u. Analogous to the D_s^d scenario, we observe that the signal distribution exhibits a peak at higher values compared to the background. This observation underscores the discriminating power of the D_s variable in distinguishing between the signal and the background. However, it's noteworthy that when employing D_s^u as the discriminating parameter, the degree of overlap between the signal and the gg-initiated background is larger than what is observed with the D_s^d variable. We find, assuming the optimistic scenario of only systematic error, $\Delta_{b_i} = 0.04$, that we can restrict

$$|\tilde{C}_{d\phi}|/(1\ \text{TeV})^2 < 0.073/\text{TeV}^2 \quad (\kappa_d < 165),$$
$$|\tilde{C}_{u\phi}|/(1\ \text{TeV})^2 < 0.057/\text{TeV}^2 \quad (\kappa_u < 275)$$

at the HL-LHC. These results are slightly worse than those obtained using the D_s^d variable. In Fig. 5.11 we finally show the dependence of the κ_d and κ_u sensitivity bounds on Δ_{b_i}

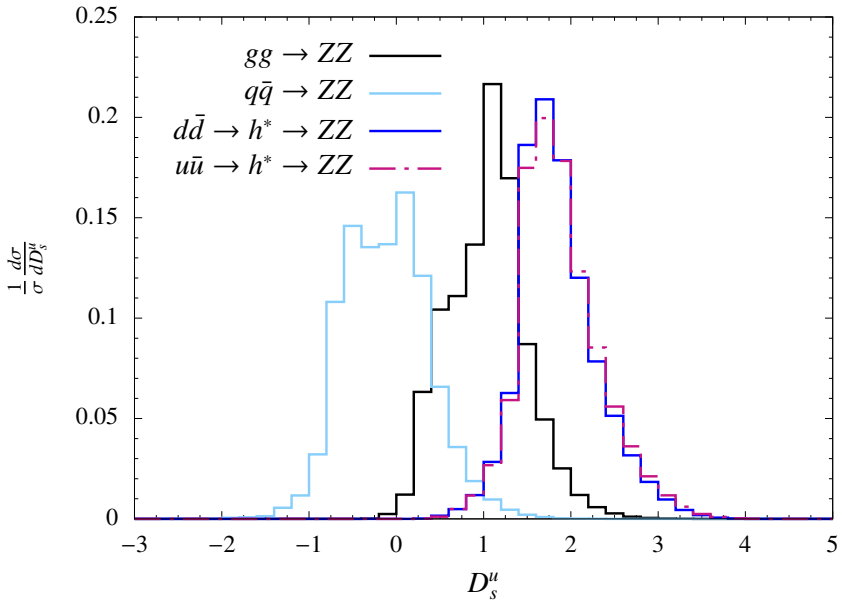

Figure 5.10: Normalised differential distributions with respect to D_s^d for signal (blue and pink dashed) and background (light blue and black) processes. Figure taken from [190].

using the D_s^u variable. Again, we observe some worsening of the sensitivity in comparison with the analysis based on the D_s^d variable.

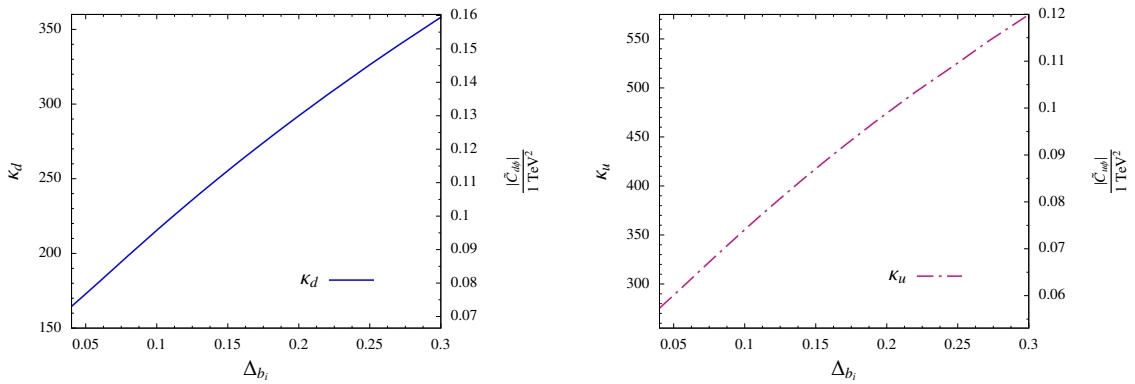

Figure 5.11: Dependence of the sensitivity bounds on κ_d ($\tilde{C}_{d\phi}$) in the left panel and κ_u ($\tilde{C}_{u\phi}$) in the right panel on the assumption made on the size of Δ_{b_i} using D_s^u. Taken from [190].

Finally, we would like to emphasise that the off-shell Higgs measurement so far seems to provide the most sensitive probe of both the up- and the down-quark Yukawa couplings.

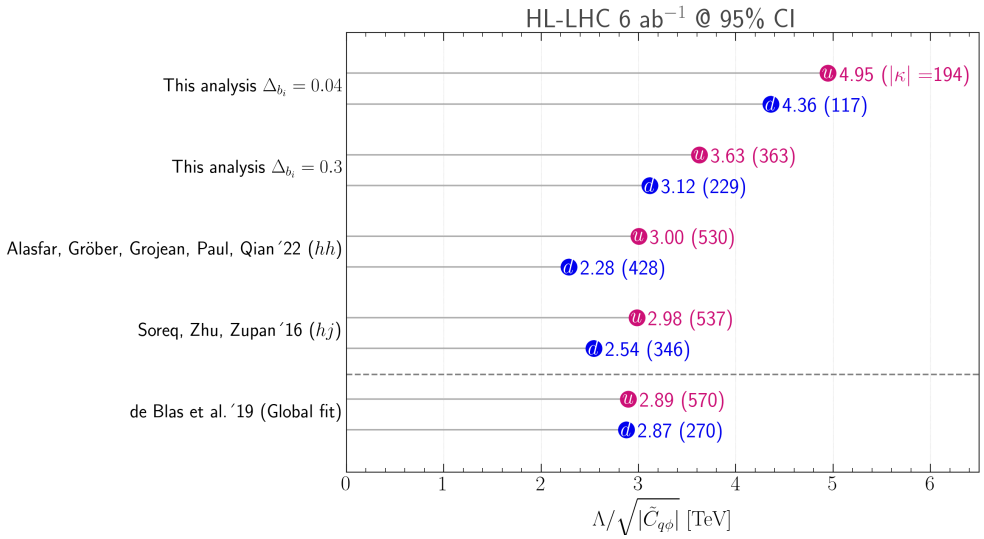

Figure 5.12: Comparison of projected constraints on $\tilde{C}_{d\phi}$ (blue) and $\tilde{C}_{u\phi}$ (pink) at 95% confidence level for the HL-LHC with 6 ab^{-1} luminosity, as estimated in this thesis and previous analyses [168, 165, 71]. The constraints are interpreted in terms of the NP scale Λ that can be probed via the measurement of the Wilson coefficients. The corresponding bounds on κ_q are included in parentheses. Figure taken from [190].

In Fig. 5.12 we compare our results with the ones obtained from alternative probes of the light-quark Yukawa couplings, *cf.* the summary plot of Ref. [168]. Even the constraints obtained in the conservative scenario assuming $\Delta_{b_i} = 0.3$ are still competitive with those found in Ref. [165].

Chapter 6

Conclusions

The E989 experiment at Fermilab, that gives us the most precise determination of the anomalous magnetic moment of the muon with a precision of 0.20 ppm, finds a discrepancy between the results from Run-1/2/3, $a_\mu^{\rm FNAL}$, and the 2020 SM prediction of the muon g-2 Theory Initiative (Ref. [5]) at 5σ [1, 2]. In [5], the leading-order hadronic contribution was obtained using $e^+e^- \to$ hadrons cross-section measurements performed by multiple experiments. However, a recent lattice calculation of the LO HVP contribution to a_μ by the BMW Collaboration [25] shows significant tension with the e^+e^- result. In addition, a new preliminary measurement of the $e^+e^- \to \pi^+\pi^-$ cross section from the CMD-3 experiment [26] disagrees significantly with all other e^+e^- data used in [5]. A new and competitive determination of LO hadronic vacuum polarization contribution is therefore desirable. This may be provided by the proposed MUonE experiment at CERN.

In the framework of this thesis, we presented simple analytic expressions to calculate the HVP contributions to the muon g-2 in the space-like region up to NNLO. These results can be employed in lattice QCD computations of $a_\mu^{\rm HVP}$ as well as in determinations based on scattering data, like those expected from the proposed MUonE experiment at CERN. In Chapter 3, following the derivation of the space-like formulation for the LO HVP contribution, obtained through the dispersion relation governed by the LO time-like kernel $K^{(2)}(z)$, I proceeded to present precise and comprehensive analytic expressions, extending the calculation of $a_\mu^{\rm HVP}$ to the NLO. The shapes of the space-like integrands of the $a_\mu^{\rm HVP}$(NLO) contributions were found to differ significantly from the LO one. In particular, the exact NLO space-like kernel $\kappa^{(4)}(x)$ provides a stronger weight to $\Delta\alpha_{\rm h}(q^2)$ at large negative values of q^2 than the LO kernel $\kappa^{(2)}(x)$. These different weights may help to shed light on the present tension between the lattice QCD determination of $a_\mu^{\rm HVP}$(LO) by the BMW collaboration and the time-like data-driven ones.

The NNLO HVP contribution to the muon g-2 is comparable to the final uncertainty expected from the Muon g-2 experiment at Fermilab. In this work, I presented straightforward analytical expressions in the space-like region for all classes of diagrams that account for these corrections. Specifically, I derived exact space-like integral formulas for diagrams featuring one- or two-loop QED vertices and two or more HVP insertions in the same photon line. For diagrams involving genuine three-loop QED vertices, such as electron or muon light-by-light graphs, I exploited generating integral representations

to fit the large-s approximate series expansions of the time-like kernels provided by Ref. [14], finding very good approximations to the space-like kernels. The uncertainty associated with these approximations of the kernels for $a_\mu^{\rm HVP}$(NNLO) is assessed to be less than $O(10^{-12})$.

In the space-like approach, the minimum required dimension of the space-like integral of $\Delta\alpha_{\rm h}(t)$ (or powers of it) to calculate a diagram's contribution to the muon g-2 is determined by the number of photon lines with distinct momenta containing HVP insertions. Consequently, to compute $a_\mu^{\rm HVP}$ at LO and NLO, one-dimensional space-like kernels are sufficient. This principle extends to NNLO, except for the specific class of diagrams featuring two HVP insertions in distinct photon lines, which necessitates a two-dimensional kernel. Generalising to two dimensions the one-dimensional method used earlier, we derived a good approximate two-dimensional space-like kernel matching the approximate time-like kernel with the series expansion of a two-dimensional generating integral representation. Once again, the uncertainty due to the kernel approximation is less than $O(10^{-12})$.

The precise calculation of higher-order HVP corrections to the muon g-2 necessitates a meticulous treatment of QED radiative corrections to the HVP function. Their leading effect, involving the emission and reabsorption of a photon by the HVP insertion, is normally incorporated into the time-like approach via the inclusion of final-state radiation corrections in the R-ratio. This is a notoriously delicate issue, because of the experimental cuts imposed by the analyses. On the other hand, the fully inclusive measurement of $\Delta\alpha_{\rm h}(t)$ expected from MUonE will naturally include these leading corrections in the space-like approach.

In conclusion, the results presented in Chapter 3 mark a significant milestone by facilitating the comparison between time-like and space-like calculations of $a_\mu^{\rm HVP}$ at NNLO accuracy. These eagerly anticipated comparisons will strengthen the SM prediction of the muon g-2 enhancing its potential to unveil new physics.

Since the time-momentum representation is often used in lattice QCD calculation, in Chapter 4 we derived a series expansion for the euclidian-time kernels up to the NLO. In particular, I obtained the analytical coefficients for the series expansion of the NLO time-kernel, on the regime of small $\hat{t}$. Additionally, we have derived representations of all components of the NLO time-kernel as Laplace integrals. From these representations we have worked out compact and fast numerical expansions of all the components of the NLO time-kernel, centered in $\hat{t} = \hat{t}_0$ and converging for $\hat{t} > \hat{t}_0/2$, for a given $\hat{t}_0$. The combination of these expansions, with a suitable choice of numbers of terms, the expansion point $\hat{t}_0$ and the separation point t_s between regimes, allows to determine the NLO time-kernel with an error $\Delta\tilde{f} < 3 \times 10^{-8}$ for every value of $\hat{t}$. The series expansions presented provide a solution to the issues posed by the asymptotic behavior of these calculations for large value of the time.

In Chapter 5 this thesis focuses on Higgs physics. The discovery of Higgs boson with a mass of approximately 125 GeV represents a monumental success for particle physics. It opened the door to the next phase, the meticulous measurement of the properties of this final component of the SM. In particular, the light-quark Yukawa couplings pose a significant challenge for experimental investigation due to their smallness in the SM. In

Chapter 5, we undertook a comprehensive study to explore the potential of off-shell Higgs production as a means to measure the Yukawa couplings of first-generation quarks. Our approach employs an EFT framework to disentangle quark masses from their couplings. This decoupling process becomes particularly valuable when addressing scenarios that involve large Yukawa couplings alongside massless quarks. The outcome of this approach is the emergence of small effective couplings, which in turn, support the use of perturbation theory and the application of a dimension-6 EFT analysis.

In scenarios where there are significant enhancements in the up and down Yukawa couplings, several notable effects come into play. First, these enhancements lead to an increase in the total width of the Higgs boson, subsequently causing a reduction in the Higgs branching ratios in its standard decay channels. On the other hand, large enhancements in Yukawa couplings also introduce a new production channel for the Higgs, in which the Higgs boson is directly generated through parton annihilation. The interplay between these effects makes it challenging to interpret off-shell measurements as a straightforward determination of the Higgs width, especially in such scenarios. Instead, the off-shell signal strength is altered, and by employing appropriate kinematic discriminants, it becomes possible to establish sensitivity limits on the modifications of the light-quark Yukawa couplings. The signal and background amplitudes exhibit distinct characteristics, such as the absence of interference related to the helicity selection rule, granting substantial discriminating power. Within the off-shell region, there are enhanced signal contributions, largely due to the behavior of the total cross section. This enhancement is particularly pronounced for processes involving the longitudinal Z boson. In the case of ggF, a similar enhancement in the off-shell region is observed. Nevertheless, at higher energy scales, the decay of the quark luminosity occurs at a slower rate compared to the gluon luminosity, resulting in an increased relative contribution from the quark channel in the off-shell region. In order to derive the distributions in the invariant mass for the ggF cross-section, I computed the form factors for the ggF amplitudes and implemented them into a Monte-Carlo code.

Throughout our investigation, our primary focus was on the scenario involving on-shell Z bosons, with specific signal process $d\bar{d} \to h^* \to ZZ \to 4\ell$ and $u\bar{u} \to h^* \to ZZ \to 4\ell$, where the enhanced Yukawa couplings are respectively applied. To ensure the robustness of this description, we introduced a selection criterion applying a cut of $m_{ZZ} > 250$ GeV and efficiency factors, whose effects have been computed and verified using `MadGraph_aMC@NLO` [205]. Our analysis has revealed that off-shell Higgs production stands out as a highly promising avenue for constraining the light-quark Yukawa couplings. In an optimistic scenario, with systematic uncertainties limited to just 4%, we have determined that values of $\kappa_d > 156$ and $\kappa_u > 260$ can be effectively excluded at HL-LHC. Here, κ_q represents the modification factor of the SM Yukawa coupling, specifically evaluated for $m_u = 2.2$ MeV and $m_d = 4.7$ MeV. These projected sensitivities surpass those obtained through the investigation of various other processes, such as Higgs pair production [167, 168], Higgs+jet interactions [165], Higgs+photon events [164], VVV [169], or the examination of charge asymmetry in $W^{\pm}h$ production [170]. We have also explored how the projected sensitivity varies based on different assumptions regarding uncertainties, and we have determined that the limits derived from off-shell production

remain competitive with other approaches even in a more conservative scenario.

The analysis we have presented is rather crude; to provide more realistic constraints it would be prudent to incorporate showers and detector effects. Additionally, considering the use of NLO matrix elements in the probabilities, as outlined in equation (5.25), could enhance the accuracy of our results. Despite the simplicity of our approach, the results are notably promising. This leads us to believe that off-shell Higgs production holds significant potential as a means to investigate the light-quark Yukawa couplings.

At the same time, it's worth noticing that the sensitivity of this analysis can be further enhanced. In ongoing off-shell analyses [73, 74], final states that include two neutrinos and two leptons, as well as Higgs production in association with jets, are being explored. Moreover, the addition of more kinematic distributions could also be beneficial.

Finally, it would be intriguing to investigate off-shell Higgs production within a more comprehensive EFT framework. This would involve incorporating additional EFT operators into the off-shell Higgs analysis and conducting a combined fit that encompasses various observables sensitive to the light-quark Yukawa couplings.

Appendix A

Tables Coefficients HVP at NNLO

(6a)	
$j_0 = 0;$	$h_0 = -\frac{359}{36};$
$j_1 = -\frac{3793}{864};$	$h_1 = \frac{122293}{5184};$
$j_2 = \frac{35087}{21600};$	$h_2 = -\frac{43879427}{648000};$
$j_3 = \frac{1592093}{43200};$	$h_3 = \frac{14388407}{48000};$
$g_0 = \frac{1301}{144} - \frac{19\pi^2}{9};$	
$g_1 = \frac{441277}{10368} + \pi^2\left(-\frac{355}{648} + \ln 4\right) + \frac{25\ \zeta(3)}{2};$	
$g_2 = -\frac{5051645167}{38880000} + \pi^2\left(\frac{221411}{32400} - 18\ln 2\right) - \frac{3919\ \zeta(3)}{60};$	
$g_3 = \frac{14588342017}{38880000} + \pi^2\left(-\frac{2479681}{64800} + 112\ln 2\right) + \frac{3113\ \zeta(3)}{10};$	
$p_0 = -\frac{1808080780513}{14580000} + \frac{41851\pi^4}{15} + \frac{8432\ln^4 2}{3} + 67456\ a_4 + \frac{2085448\ \zeta(3)}{15} +$ $+\pi^2\left(-\frac{11944163099}{194400} + \frac{272}{3}(180 - 31\ln 2)\ln 2 + \frac{115072\ \zeta(3)}{3}\right) - \frac{575360\ \zeta(5)}{3};$	
$p_1 = \frac{134017456919}{96000} - \frac{4481182\pi^4}{135} - \frac{98420\ln^4 2}{3} - 787360\ a_4 + 2255200\ \zeta(5) +$ $+\pi^2\left(\frac{23549054249}{32400} - 201122\ln 2 + \frac{98420\ln^2 2}{3} - 451040\ \zeta(3)\right) - \frac{57189259\ \zeta(3)}{36};$	
$p_2 = -\frac{13069081405453}{3888000} + \frac{330073\pi^4}{4} + 80790\ln^4 2 + 1938960\ a_4 + \frac{77371609\ \zeta(3)}{20} +$ $+\pi^2\left(-\frac{729995599}{405} + 6(85313 - 13465\ln 2)\ln 2 + 1114360\ \zeta(3)\right) - 5571800\ \zeta(5);$	
$p_3 = \frac{1274611832039}{583200} - \frac{986377\pi^4}{18} - 53340\ln^4 2 - 1280160\ a_4 + \frac{11057200\ \zeta(5)}{3} +$ $+\pi^2\left(\frac{5809659289}{4860} + 420\ln 2(-823 + 127\ln 2) - \frac{2211440\ \zeta(3)}{3}\right) - \frac{22833188\ \zeta(3)}{9};$	

Table A.1: The coefficients $g_i^{(6a)}, h_i^{(6a)}, j_i^{(6a)}, p_i^{(6a)} (i = 0, 1, 2, 3)$ from [46]. The superscript (6a) has been dropped for simplicity. In the above coefficients, the Riemann zeta function $\zeta(k) = \sum_{n=1}^{\infty} 1/n^k$ and $a_4 = \sum_{n=1}^{\infty} 1/\left(2^n n^4\right) = \mathrm{Li}_4(1/2)$.

(6b)	
$j_0 = 0;$	$h_0 = \frac{65}{54};$
$j_1 = \frac{11}{27};$	$h_1 = -\frac{3559}{1296} + \rho^2 + \frac{5}{18}\ln\rho;$
$j_2 = \frac{41}{120};$	$h_2 = \frac{3917}{432} - \frac{82\rho^2}{3} + \frac{61}{10}\ln\rho;$
$j_3 = -\frac{507}{40};$	$h_3 = -\frac{4109}{80} + \frac{2211\rho^2}{10} - \frac{1763}{30}\ln\rho;$
$g_0 = \frac{1}{108}\left(259 - 72\rho^2 + 276\ln\rho\right);$	
$g_1 = -\frac{9215}{1296} + \frac{65\pi^2}{162} - \frac{3\pi^2\rho}{4} + \frac{49\rho^2}{36} + \left(-\frac{301}{54} + 8\rho^2\right)\ln\rho + \frac{4}{3}\ln^2\rho + 2\,\zeta(3);$	
$g_2 = \frac{501971}{40500} - \frac{113\pi^2}{36} + \frac{270\pi^2\rho}{36} - \frac{8417\rho^2}{180} + \left(\frac{3479}{900} - 44\rho^2\right)\ln\rho - 8\ln^2\rho - 12\,\zeta(3);$	
$g_3 = -\frac{2523823}{324000} + \frac{625\pi^2}{36} - 49\pi^2\rho + \frac{84946\rho^2}{225} + \left(\frac{987}{50} + 200\rho^2\right)\ln\rho + \frac{112}{3}\ln^2\rho + 56\,\zeta(3);$	
$p_0 = -\frac{95519053063}{486000} - 7275\pi^2\rho + \pi^2\left(\frac{24382331}{810} - \frac{285184}{9}\ln 2\right) + \left(-\frac{587150693}{5400} + \frac{75272\rho^2}{3}\right)\ln\rho +$ $+\frac{120800\pi^2}{9}\ln\rho + 4720\ln^2\rho + \frac{1067115409\rho^2}{5400} - 32\pi^2\rho^2\left(687 + \ln 4\right) + \left(\frac{1135508}{9} + 96\rho^2\right)\zeta(3);$	
$p_1 = \frac{279489728279}{121500} + \frac{179283\pi^2\rho}{2} + \pi^2\left(-\frac{143574463}{405} + \frac{3352256\ln 2}{9}\right) + \left(\frac{2280933773}{1800} - 309540\rho^2\right)\ln\rho +$ $-\frac{1419328\pi^2}{9}\ln\rho - \frac{174712}{3}\ln^2\rho - \frac{174350167\rho^2}{75} + \frac{16}{3}\pi^2\rho^2\left(48481 + 90\ln 2\right) +$ $-\frac{10}{3}\left(446023 + 216\rho^2\right)\zeta(3);$	
$p_2 = -\frac{229560199193}{40500} - \frac{912495\pi^2\rho}{4} + \frac{4}{135}\pi^2(29597029 - 31048560\ln 2) + \left(-\frac{1867939691}{600}\right)\ln\rho +$ $+\left(788488\rho^2 + \frac{1168336\pi^2}{3}\right)\ln\rho + 148348\ln^2\rho + \frac{258653648\rho^2}{45} +$ $-\frac{320}{3}\pi^2\rho^2\left(5989 + \ln 512\right) + \left(\frac{11034553}{3} + 1440\rho^2\right)\zeta(3);$	
$p_3 = \frac{72762177677}{19440} + 154035\pi^2\rho + \frac{35}{162}\pi^2\left(-2687659 + 2816064\ln 2\right) +$ $-\frac{7}{108}\left(-31650719 + 3973440\pi^2 + 8220240\rho^2\right)\ln\rho +$ $-100240\ln^2\rho - \frac{513692207\rho^2}{135} + \frac{140}{3}\pi^2\rho^2\left(9055 + \ln 4096\right) - \frac{280}{9}\left(78283 + 27\rho^2\right)\zeta(3);$	

Table A.2: Table 2: The coefficients $g_i^{(6b)}, h_i^{(6b)}, j_i^{(6b)}, p_i^{(6b)} (i = 0, 1, 2, 3)$ from [46]. The superscript (6b) has been dropped for simplicity. In the above coefficients, $\rho = m_e/m$, the Riemann zeta function $\zeta(k) = \sum_{n=1}^{\infty} 1/n^k$, and $a_4 = \sum_{n=1}^{\infty} 1/\left(2^n n^4\right) = \mathrm{Li}_4(1/2)$.

(6bll)

$$j_0 = 0;$$
$$j_1 = \frac{4}{27} - \frac{9\rho^2}{2};$$
$$j_2 = -\frac{41}{48} + \frac{2201\rho^2}{216};$$
$$j_3 = \frac{3037}{900} - \frac{5909\rho^2}{216};$$

$$h_0 = -\frac{9}{2};$$
$$h_1 = \frac{59}{9} - \frac{275\rho^2}{36} - 18\rho^2 \ln\rho;$$
$$h_2 = -\frac{485}{32} + \frac{1351\rho^2}{48} + \frac{659\rho^2}{18}\ln\rho;$$
$$h_3 = \frac{282617}{6750} - \frac{10481\rho^2}{108} - \frac{851\rho^2}{9}\ln\rho;$$

$$g_0 = \frac{43}{8} - 4\pi^2\rho + 15\rho^2 + \pi^2\rho^2 - 18\rho^2\ln\rho + 6\rho^2\ln^2\rho;$$
$$g_1 = -\frac{73}{81} + \frac{8\pi^2}{81} + \frac{40\pi^2\rho}{9} + \frac{2437\rho^2}{108} + \frac{17\pi^2\rho^2}{9} + \frac{607\rho^2}{18}\ln\rho - \frac{20\rho^2}{3}\ln^2\rho + \frac{2}{3}\zeta(3) + 2\rho^2\zeta(3);$$
$$g_2 = -\frac{385}{162} - \frac{41\pi^2}{72} - \frac{28\pi^2\rho}{3} - \frac{89873\rho^2}{5184} - \frac{997\pi^2\rho^2}{324} - \frac{1961\rho^2}{72}\ln\rho + 14\rho^2\ln^2\rho - \frac{5}{2}\zeta(3) - \frac{16\rho^2}{3}\zeta(3);$$
$$g_3 = \frac{2691761}{202500} + \frac{3037\pi^2}{1350} + 24\pi^2\rho + \frac{655429\rho^2}{97200} + \frac{2359\pi^2\rho^2}{324} + \frac{6943\rho^2}{360}\ln\rho - 36\rho^2\ln^2\rho +$$
$$+\frac{42}{5}\zeta(3) + 15\rho^2\zeta(3);$$

$$p_0 = -\frac{343277101}{45000} - \frac{33156604927\rho^2}{583200} + \pi^2\left(-\frac{615427}{4050} + \frac{6776\rho}{3} + \frac{763121\rho^2}{972}\right) - \frac{4\pi^4}{135}\left(7817 + 3212\rho^2\right) +$$
$$+\left(-\frac{7290521}{3240} + \frac{49622\pi^2}{27} - \frac{128\pi^4}{9}\right)\rho^2\ln\rho + \left(-3388 - \frac{80\pi^2}{3}\right)\rho^2\ln^2\rho +$$
$$+\left(25642 + \frac{1515724\rho^2}{27} - 128\pi^2\rho^2 - 160\rho^2\ln\rho\right)\zeta(3) - \frac{1280}{3}\rho^2\zeta(5);$$
$$p_1 = \frac{89280434843}{972000} + \frac{248834878697\rho^2}{388800} - \frac{1}{324}\pi^2\left(-533001 + 9110736\rho + 3110417\rho^2\right) +$$
$$+\frac{2}{135}\pi^4\left(180247 + 73530\rho^2\right) + \left(\frac{11101973}{1080} - \frac{193400\pi^2}{9} + \frac{320\pi^4}{3}\right)\rho^2\ln\rho +$$
$$+\frac{1}{45}\left(-13410977 + 100\left(-292301 + 432\pi^2\right)\rho^2 + 54000\rho^2\ln\rho\right)\zeta(3) + 3200\rho^2\zeta(5) +$$
$$+\frac{2}{3}\left(63269 + 300\pi^2\right)\rho^2\ln^2\rho;$$
$$p_2 = -\frac{6209532853}{27000} - \frac{29997466847\rho^2}{19440} + \pi^2\left(-\frac{114521}{30} + 71840\rho + \frac{1970140\rho^2}{81}\right) +$$
$$-\frac{1}{54}\left(190613 - 2847360\pi^2 + 11520\pi^4\right)\rho^2\ln\rho - 80\left(1347 + 5\pi^2\right)\rho^2\ln^2\rho +$$
$$-\frac{10}{9}\left(-658509 + \left(-1431463 + 1728\pi^2\right)\rho^2 + 2160\rho^2\ln\rho\right)\zeta(3) - 6400\rho^2\zeta(5) +$$
$$-\frac{4}{9}\pi^4\left(14685 + 6032\rho^2\right)$$
$$p_3 = \frac{49726331179}{324000} + \frac{7324831423\rho^2}{7290} + \pi^2\left(\frac{3897971}{1620} - \frac{145880\rho}{3} - \frac{3977785\rho^2}{243}\right) + \frac{14}{27}\pi^4\left(8269 + 3419\rho^2\right) +$$
$$+\frac{7}{81}\left(-81551 - 401520\pi^2 + 1440\pi^4\right)\rho^2\ln\rho + \frac{140}{3}\left(1563 + 5\pi^2\right)\rho^2\ln^2\rho +$$
$$+\frac{35}{27}\left(-371889 + 16\left(-50437 + 54\pi^2\right)\rho^2 + 1080\rho^2\ln\rho\right)\zeta(3) + \frac{11200}{3}\rho^2\zeta(5);$$

Table A.3: The coefficients $g_i^{(6bll)}, h_i^{(6bll)}, j_i^{(6bll)}, p_i^{(6bll)} (i = 0, 1, 2, 3)$ from [46]. The superscript $(6bll)$ has been dropped for simplicity. In the above coefficients, $\rho = m_e/m$, the Riemann zeta function $\zeta(k) = \sum_{n=1}^{\infty} 1/n^k$, and $a_4 = \sum_{n=1}^{\infty} 1/\left(2^n n^4\right) = \mathrm{Li}_4(1/2)$.

Appendix B

Tables Coefficients HVP at NLO in TMR

$\mathbf{n}$	$\mathbf{a_n}$	$\mathbf{b_n}$	$\mathbf{c_n}$	$\mathbf{d_n}$
4	$\frac{317}{216}$	$-\frac{1}{3}$	$\frac{23}{18}$	0
6	$\frac{843829}{259200}$	$-\frac{371}{432}$	$\frac{877}{1080}$	$\frac{19}{36}$
8	$\frac{412181237}{5292000}$	$-\frac{233}{48}$	$-\frac{824603}{25200}$	$\frac{141}{20}$
10	$\frac{6272504689}{10584000}$	$-\frac{1165}{48}$	$-\frac{460711}{1680}$	$\frac{961}{20}$
12	$\frac{404220031035193}{121022748000}$	$-\frac{42443}{378}$	$-\frac{1359283213}{873180}$	$\frac{79342}{315}$
14	$\frac{14790819716039431}{890463974400}$	$-\frac{142931}{288}$	$-\frac{4138386457}{540540}$	$\frac{28243}{24}$
16	$\frac{38888413518277699}{503454631680}$	$-\frac{12895145}{6048}$	$-\frac{489120278261}{13970880}$	$\frac{2605993}{504}$
18	$\frac{3950633085365067019}{11462583132000}$	$-\frac{116506871}{12960}$	$-\frac{4589675124823}{29937600}$	$\frac{23642359}{1080}$
20	$\frac{364721869802634477577571}{243865691961091200}$	$-\frac{55559731}{1485}$	$-\frac{37593205363634911}{57616158600}$	$\frac{44767436}{495}$
22	$\frac{77392239282793945882249}{12165635426630400}$	$-\frac{610873921}{3960}$	$-\frac{26135521670035411}{9602693100}$	$\frac{121188929}{330}$
24	$\frac{27318770927965379913670522297}{1024872666654481444800}$	$-\frac{19509636989}{30888}$	$-\frac{5138081420797732289}{459392837904}$	$\frac{3789385597}{2574}$
26	$\frac{44996849076816882871466510066 3}{4076198106012142110000}$	$-\frac{5618399257}{2184}$	$-\frac{15810911801773817669}{348024877200}$	$\frac{151912159}{26}$
28	$\frac{25114629392949805515668354 9773}{554584776328182600000}$	$-\frac{678234361}{65}$	$-\frac{3787066553671821473}{20715766500}$	$\frac{1495034796}{65}$
30	$\frac{10079211746301768464355522417 8269168501}{54680554570762463049907200000}$	$-\frac{2551294690547}{60480}$	$-\frac{30599625762869165887553 3}{419236121304000}$	$\frac{64743309493}{720}$

Table B.1: Coefficients of the expansion of $\tilde{f}_4(t)$ for small $\hat{t}$ up to $\hat{t}^{30}$ (from [128]), see (4.22)

n	$a_n^{(b;1,1)}$	$a_n^{(b;1,2)}$	$a_n^{(b;2,1)}$	$a_n^{(b;2,2)}$	$a_n^{(b;2,3)}$
0	-1.4724671380	1.1589872337	-4.8942765691	0.2973718753	2.1170734478
1	0.1002442629	-0.0022459376	-2.9475017651	0.4127862149	1.0364595246
2	0.0021557710	0.0008279191	-0.5075497783	0.1109534688	0.1101698869
3	0.0001282655	0.0007999410	0.0115794503	-0.0040980259	0.0167667530
4	-0.0001467432	-0.0006094594	-0.0013940058	0.0003899989	-0.0035236970
5	9.35581×10^{-6}	7.37693×10^{-6}	0.0001421294	-0.0000133805	0.0008586372
6	0.0000260037	0.0002711371	7.67679×10^{-6}	-0.00001764961	-0.0002257379
7	-0.0000189910	-0.0002551246	-0.00001492424	.000011742325	0.0000612688
8	6.93309×10^{-6}	0.0001291619	8.61706×10^{-6}	-5.92454×10^{-6}	-0.0000164422
9	3.18779×10^{-7}	-0.0000121615	-4.20065×10^{-6}	2.78837×10^{-6}	4.04750×10^{-6}
10	-2.93399×10^{-6}	-0.0000553459	1.95419×10^{-6}	-1.29025×10^{-6}	-7.17744×10^{-7}
11	2.98580×10^{-6}	0.0000760414	-9.00478×10^{-7}	5.98351×10^{-7}	-7.67136×10^{-8}
12	-2.08433×10^{-6}	-0.0000669985	4.17032×10^{-7}	-2.80343×10^{-7}	1.94188×10^{-7}

Table B.2: Coefficients of the expansions in v of $\frac{m_\mu^2}{16\pi^2}\tilde{f}_4(t)$ up to v^{12} with $\hat{t}_0 = 5$ (from [128]), see (4.77).

Bibliography

[1] B. Abi *et al.* [Muon g-2], Phys. Rev. Lett. **126** (2021) no.14, 141801 [arXiv:2104.03281 [hep-ex]].
T. Albahri *et al.* [Muon g-2], Phys. Rev. D **103** (2021) no.7, 072002 [arXiv:2104.03247 [hep-ex]].
T. Albahri *et al.* [Muon g-2], Phys. Rev. A **103** (2021) no.4, 042208 [arXiv:2104.03201 [hep-ex]].
T. Albahri *et al.* [Muon g-2], Phys. Rev. Accel. Beams **24** (2021) no.4, 044002 [arXiv:2104.03240 [physics.acc-ph]].

[2] D. P. Aguillard *et al.* [Muon g-2], Phys. Rev. Lett. **131** (2023) no.16, 161802 [arXiv:2308.06230 [hep-ex]].

[3] G. W. Bennett *et al.* [Muon g-2], Phys. Rev. D **73** (2006), 072003 [arXiv:hep-ex/0602035 [hep-ex]].

[4] M. Abe *et al.* PTEP **2019** (2019) no.5, 053C02 [arXiv:1901.03047 [physics.ins-det]].

[5] T. Aoyama *et al.* Phys. Rept. **887** (2020), 1-166 [arXiv:2006.04822 [hep-ph]].

[6] F. Jegerlehner, Springer Tracts Mod. Phys. **274** (2017), pp.1-693 Springer, 2017,

[7] M. Davier, A. Hoecker, B. Malaescu and Z. Zhang, Eur. Phys. J. C **77** (2017) no.12, 827 [arXiv:1706.09436 [hep-ph]].

[8] A. Keshavarzi, D. Nomura and T. Teubner, Phys. Rev. D **97** (2018) no.11, 114025 [arXiv:1802.02995 [hep-ph]].

[9] G. Colangelo, M. Hoferichter and P. Stoffer, JHEP **02** (2019), 006 [arXiv:1810.00007 [hep-ph]].

[10] M. Hoferichter, B. L. Hoid and B. Kubis, JHEP **08** (2019), 137 [arXiv:1907.01556 [hep-ph]].

[11] M. Davier, A. Hoecker, B. Malaescu and Z. Zhang, Eur. Phys. J. C **80** (2020) no.3, 241 [erratum: Eur. Phys. J. C **80** (2020) no.5, 410] [arXiv:1908.00921 [hep-ph]].

[12] A. Keshavarzi, D. Nomura and T. Teubner, Phys. Rev. D **101** (2020) no.1, 014029 [arXiv:1911.00367 [hep-ph]].

[13] B. L. Hoid, M. Hoferichter and B. Kubis, Eur. Phys. J. C **80** (2020) no.10, 988 [arXiv:2007.12696 [hep-ph]].

[14] A. Kurz, T. Liu, P. Marquard and M. Steinhauser, Phys. Lett. B **734** (2014), 144-147 [arXiv:1403.6400 [hep-ph]].

[15] B. Chakraborty *et al.* [Fermilab Lattice, LATTICE-HPQCD and MILC], Phys. Rev. Lett. **120** (2018) no.15, 152001 [arXiv:1710.11212 [hep-lat]].

[16] S. Borsanyi *et al.* [Budapest-Marseille-Wuppertal], Phys. Rev. Lett. **121** (2018) no.2, 022002 [arXiv:1711.04980 [hep-lat]].

[17] T. Blum *et al.* [RBC and UKQCD], Phys. Rev. Lett. **121** (2018) no.2, 022003 [arXiv:1801.07224 [hep-lat]].

[18] D. Giusti, V. Lubicz, G. Martinelli, F. Sanfilippo and S. Simula, Phys. Rev. D **99** (2019) no.11, 114502 [arXiv:1901.10462 [hep-lat]].

[19] E. Shintani *et al.* [PACS], Phys. Rev. D **100** (2019) no.3, 034517 [arXiv:1902.00885 [hep-lat]].

[20] C. T. H. Davies *et al.* [Fermilab Lattice, LATTICE-HPQCD and MILC], Phys. Rev. D **101** (2020) no.3, 034512 [arXiv:1902.04223 [hep-lat]].

[21] A. Gérardin, M. Cè, G. von Hippel, B. Hörz, H. B. Meyer, D. Mohler, K. Ottnad, J. Wilhelm and H. Wittig, Phys. Rev. D **100** (2019) no.1, 014510 [arXiv:1904.03120 [hep-lat]].

[22] C. Aubin, T. Blum, C. Tu, M. Golterman, C. Jung and S. Peris, Phys. Rev. D **101** (2020) no.1, 014503 [arXiv:1905.09307 [hep-lat]].

[23] D. Giusti and S. Simula, PoS **LATTICE2019** (2019), 104 [arXiv:1910.03874 [hep-lat]].

[24] B. Chakraborty, C. T. H. Davies, J. Koponen, G. P. Lepage and R. S. Van de Water, Phys. Rev. D **98** (2018) no.9, 094503 [arXiv:1806.08190 [hep-lat]].

[25] S. Borsanyi *et al.* Nature **593** (2021) no.7857, 51-55 [arXiv:2002.12347 [hep-lat]].

[26] F. V. Ignatov *et al.* [CMD-3], "Measurement of the $e^+e^- \to \pi^+\pi^-$ cross section from threshold to 1.2 GeV with the CMD-3 detector," [arXiv:2302.08834 [hep-ex]].

[27] G. Colangelo, A. X. El-Khadra, M. Hoferichter, A. Keshavarzi, C. Lehner, P. Stoffer and T. Teubner, Phys. Lett. B **833** (2022), 137313 [arXiv:2205.12963 [hep-ph]].

[28] M. Cè *et al.* Phys. Rev. D **106** (2022) no.11, 114502 [arXiv:2206.06582 [hep-lat]].

[29] C. Alexandrou *et al.* [Extended Twisted Mass], Phys. Rev. D **107** (2023) no.7, 074506 [arXiv:2206.15084 [hep-lat]].

[30] A. Bazavov *et al.* [Fermilab Lattice, HPQCD, and MILC], Phys. Rev. D **107** (2023) no.11, 114514 [arXiv:2301.08274 [hep-lat]].

[31] T. Blum *et al.* [RBC and UKQCD], Phys. Rev. D **108** (2023) no.5, 054507 [arXiv:2301.08696 [hep-lat]].

[32] C. M. Carloni Calame, M. Passera, L. Trentadue and G. Venanzoni, Phys. Lett. B **746** (2015), 325-329 [arXiv:1504.02228 [hep-ph]].

[33] G. Abbiendi *et al.* Eur. Phys. J. C **77** (2017) no.3, 139 [arXiv:1609.08987 [hep-ex]].

[34] The MUonE Collaboration, *Letter of Intent: The MUonE Project*, CERN SPSC-2019-026/SPSC-I-252. https://cds.cern.ch/record/2677471/files/SPSC-I-252.pdf

[35] P. Mastrolia, M. Passera, A. Primo and U. Schubert, JHEP **11** (2017), 198 [arXiv:1709.07435 [hep-ph]].

[36] S. Di Vita, S. Laporta, P. Mastrolia, A. Primo and U. Schubert, JHEP **09** (2018), 016 [arXiv:1806.08241 [hep-ph]].

[37] M. Alacevich, C. M. Carloni Calame, M. Chiesa, G. Montagna, O. Nicrosini and F. Piccinini, JHEP **02** (2019), 155 [erratum: JHEP **02** (2022), 201] [arXiv:1811.06743 [hep-ph]].

[38] M. Fael, JHEP **02** (2019), 027 [arXiv:1808.08233 [hep-ph]].

[39] M. Fael and M. Passera, Phys. Rev. Lett. **122** (2019) no.19, 192001 [arXiv:1901.03106 [hep-ph]].

[40] P. Banerjee *et al.* Eur. Phys. J. C **80** (2020) no.6, 591 [arXiv:2004.13663 [hep-ph]].

[41] C. M. Carloni Calame, M. Chiesa, S. M. Hasan, G. Montagna, O. Nicrosini and F. Piccinini, JHEP **11** (2020), 028 [arXiv:2007.01586 [hep-ph]].

[42] P. Banerjee, T. Engel, A. Signer and Y. Ulrich, SciPost Phys. **9** (2020), 027 [arXiv:2007.01654 [hep-ph]].

[43] R. Bonciani *et al.* Phys. Rev. Lett. **128** (2022) no.2, 022002 [arXiv:2106.13179 [hep-ph]].

[44] E. Budassi, C. M. Carloni Calame, M. Chiesa, C. L. Del Pio, S. M. Hasan, G. Montagna, O. Nicrosini and F. Piccinini, JHEP **11** (2021), 098 [arXiv:2109.14606 [hep-ph]].

[45] A. V. Nesterenko, J. Phys. G **49** (2022) no.5, 055001 [arXiv:2112.05009 [hep-ph]].

[46] E. Balzani, S. Laporta and M. Passera, Phys. Lett. B **834** (2022), 137462 [arXiv:2112.05704 [hep-ph]].

[47] M. Fael, F. Lange, K. Schönwald and M. Steinhauser, Phys. Rev. Lett. **128** (2022) no.17, 172003 [arXiv:2202.05276 [hep-ph]].

[48] M. Fael, F. Lange, K. Schönwald and M. Steinhauser, Phys. Rev. D **106** (2022) no.3, 034029 [arXiv:2207.00027 [hep-ph]].

[49] D. Greynat and E. de Rafael, JHEP **05** (2022), 084 [arXiv:2202.10810 [hep-ph]].

[50] E. Budassi, C. M. Carloni Calame, C. L. Del Pio and F. Piccinini, Phys. Lett. B **829** (2022), 137138 [arXiv:2203.01639 [hep-ph]].

[51] A. Broggio *et al.* JHEP **01** (2023), 112 [arXiv:2212.06481 [hep-ph]].

[52] M. Fael, F. Lange, K. Schönwald and M. Steinhauser, Phys. Rev. D **107** (2023) no.9, 094017 [arXiv:2302.00693 [hep-ph]].

[53] S. Badger, J. Kryś, R. Moodie and S. Zoia, JHEP **11** (2023), 041 [arXiv:2307.03098 [hep-ph]].

[54] T. Ahmed, G. Crisanti, F. Gasparotto, S. M. Hasan and P. Mastrolia, [arXiv:2308.05028 [hep-ph]].

[55] G. Aad *et al.* [ATLAS], Phys. Lett. B **716** (2012), 1-29 [arXiv:1207.7214 [hep-ex]].

[56] S. Chatrchyan *et al.* [CMS], Phys. Lett. B **716** (2012), 30-61 [arXiv:1207.7235 [hep-ex]].

[57] S. L. Glashow, Nucl. Phys. **10** (1959), 107-117

[58] A. Salam and J. C. Ward, Nuovo Cim. **11** (1959), 568-577

[59] S. Weinberg, Phys. Rev. Lett. **19** (1967), 1264-1266

[60] G. 't Hooft and M. J. G. Veltman, Nucl. Phys. B **44** (1972), 189-213

[61] P. W. Higgs, Phys. Rev. Lett. **13** (1964), 508-509

[62] P. W. Higgs, Phys. Lett. **12** (1964), 132-133

[63] F. Englert and R. Brout, Phys. Rev. Lett. **13** (1964), 321-323

[64] G. S. Guralnik, C. R. Hagen and T. W. B. Kibble, Phys. Rev. Lett. **13** (1964), 585-587

[65] T. W. B. Kibble, Phys. Rev. **155** (1967), 1554-1561

[66] P. W. Anderson, Phys. Rev. **130** (1963), 439-442

[67] [ATLAS], Nature **607** (2022) no.7917, 52-59 [erratum: Nature **612** (2022) no.7941, E24] [arXiv:2207.00092 [hep-ex]].

[68] A. Tumasyan *et al.* [CMS], Nature **607** (2022) no.7917, 60-68 [arXiv:2207.00043 [hep-ex]].

[69] G. Aad *et al.* [ATLAS], Phys. Lett. B **812** (2021), 135980 [arXiv:2007.07830 [hep-ex]].

[70] A. M. Sirunyan *et al.* [CMS], JHEP **01** (2021), 148 [arXiv:2009.04363 [hep-ex]].

[71] J. de Blas *et al.* JHEP **01** (2020), 139 [arXiv:1905.03764 [hep-ph]].

[72] Y. Zhou, Phys. Rev. D **93** (2016) no.1, 013019 [arXiv:1505.06369 [hep-ph]].

[73] A. Tumasyan *et al.* [CMS], Nature Phys. **18** (2022) no.11, 1329-1334 [arXiv:2202.06923 [hep-ex]].

[74] G. Aad *et al.* [ATLAS], [arXiv:2304.01532 [hep-ex]].

[75] M. Passera, J. Phys. G **31** (2005), R75-R94. [arXiv:hep-ph/0411168 [hep-ph]].

[76] X. Fan, T. G. Myers, B. A. D. Sukra and G. Gabrielse, Phys. Rev. Lett. **130** (2023) no.7, 071801 [arXiv:2209.13084 [physics.atom-ph]].

[77] G. F. Giudice, P. Paradisi and M. Passera, JHEP **11** (2012), 113 [arXiv:1208.6583 [hep-ph]].

[78] T. Kinoshita and W. B. Lindquist, Phys. Rev. D **42** (1990), 636-655.

[79] T. Kinoshita, B. Nizic and Y. Okamoto, Phys. Rev. Lett. **52** (1984), 717.

[80] S. Laporta, Phys. Lett. B **772** (2017), 232-238. [arXiv:1704.06996 [hep-ph]].

[81] B. E. Lautrup, Phys. Lett. B **38** (1972), 408-410.

[82] A. Kurz, T. Liu, P. Marquard and M. Steinhauser, Nucl. Phys. B **879** (2014), 1-18 [arXiv:1311.2471 [hep-ph]].

[83] T. Aoyama, M. Hayakawa, T. Kinoshita and M. Nio, Phys. Rev. Lett. **109** (2012), 111808 [arXiv:1205.5370 [hep-ph]].

[84] J. S. Schwinger, Phys. Rev. **73** (1948), 416-417.

[85] C. M. Sommerfield, Phys. Rev. **107** (1957), 328-329.

[86] A. Petermann, Helv. Phys. Acta **30** (1957), 407-408.

[87] H. H. Elend, Phys. Lett. **20**, 682 (1966), [Erratum: Phys. Lett. **21**, 720 (1966)].

[88] G. Li, R. Mendel and M. A. Samuel, Phys. Rev. D **47** (1993), 1723-1725

[89] J. A. Mignaco and E. Remiddi Nuovo Cimento A **60** 519 (1969).
R. Barbieri and E. Remiddi, Phys. Lett. B **49** (1974), 468-470.
R. Barbieri and E. Remiddi, Nucl. Phys. B **90** (1975), 233-266.
R. Barbieri, M. Caffo and E. Remiddi, Phys. Lett. B **57** (1975), 460-462.
M. J. Levine, E. Remiddi and R. Roskies, Phys. Rev. D **20** (1979), 2068-2076.
S. Laporta and E. Remiddi, Phys. Lett. B **265** (1991), 182-184.
S. Laporta, Phys. Rev. D **47** (1993), 4793-4795.
S. Laporta, Phys. Lett. B **343** (1995), 421-426.
S. Laporta and E. Remiddi, Phys. Lett. B **356** (1995), 390-397.

[90] S. Laporta and E. Remiddi, Phys. Lett. B **379** (1996), 283-291. [arXiv:hep-ph/9602417 [hep-ph]].

[91] S. Laporta, Nuovo Cim. A **106** (1993), 675-683.

[92] S. Laporta and E. Remiddi, Phys. Lett. B **301** (1993), 440-446.

[93] M. Caffo, S. Turrini and E. Remiddi, Phys. Rev. D **30** (1984), 483.
E. Remiddi and S. P. Sorella, Lett. Nuovo Cim. **44** (1985), 231.
D. J. Broadhurst, A. L. Kataev and O. V. Tarasov, Phys. Lett. B **298** (1993), 445-452.
S. Laporta, Phys. Lett. B **312** (1993), 495-500.
P. A. Baikov and D. J. Broadhurst, [arXiv:hep-ph/9504398 [hep-ph]].

[94] R. H. Parker, C. Yu, W. Zhong, B. Estey and H. Müller, Science **360** (2018), 191. [arXiv:1812.04130 [physics.atom-ph]].

[95] R. Jackiw and S. Weinberg, Phys. Rev. D **5** (1972), 2396-2398.
I. Bars and M. Yoshimura, Phys. Rev. D **6** (1972), 374-376.
G. Altarelli, N. Cabibbo and L. Maiani, Phys. Lett. B **40** (1972), 415-419.
W. A. Bardeen, R. Gastmans and B. E. Lautrup, Nucl. Phys. B **46** (1972), 319-331.
K. Fujikawa, B. W. Lee and A. I. Sanda, Phys. Rev. D **6** (1972), 2923-2943.

[96] A. Czarnecki, B. Krause and W. J. Marciano, Phys. Rev. D **52** (1995), 2619-2623. [arXiv:hep-ph/9506256 [hep-ph]].

[97] A. Czarnecki, B. Krause and W. J. Marciano, Phys. Rev. Lett. **76** (1996), 3267-3270. [arXiv:hep-ph/9512369 [hep-ph]].

[98] T. Kaneko and N. Nakazawa, [arXiv:hep-ph/9505278 [hep-ph]].

[99] S. Peris, M. Perrottet and E. de Rafael, Phys. Lett. B **355** (1995), 523-530 [arXiv:hep-ph/9505405 [hep-ph]].

[100] A. Czarnecki, W. J. Marciano and A. Vainshtein, Phys. Rev. D **67** (2003), 073006. [arXiv:hep-ph/0212229 [hep-ph]].

[101] M. Knecht, S. Peris, M. Perrottet and E. De Rafael, JHEP **11** (2002), 003 [arXiv:hep-ph/0205102 [hep-ph]].

[102] C. Gnendiger, D. Stöckinger and H. Stöckinger-Kim, Phys. Rev. D **88** (2013), 053005. [arXiv:1306.5546 [hep-ph]].

[103] T. Ishikawa, N. Nakazawa and Y. Yasui, Phys. Rev. D **99** (2019) no.7, 073004. [arXiv:1810.13445 [hep-ph]].

[104] M. Tanabashi *et al.* [Particle Data Group], Phys. Rev. D **98** (2018) no.3, 030001.

[105] C. Bouchiat and L. Michel, J. Phys. Radium **22** (1961) no.2, 121-121.

[106] A. Masiero, P. Paradisi and M. Passera, [arXiv:2002.05418 [hep-ph]].

[107] P. S. B. Dev, W. Rodejohann, X. J. Xu and Y. Zhang, JHEP **05** (2020), 053 [arXiv:2002.04822 [hep-ph]].

[108] R. V. Harlander and M. Steinhauser, Comput. Phys. Commun. **153** (2003), 244-274. [arXiv:hep-ph/0212294 [hep-ph]].

[109] G. Abbiendi *et al.*, JINST **15** (2020) no.01, 01. [arXiv:1905.11677 [physics.ins-det]].

[110] S. J. Brodsky and E. De Rafael, Phys. Rev. **168** (1968), 1620-1622

[111] B. E. Lautrup and E. De Rafael, Phys. Rev. **174** (1968), 1835-1842

[112] J. Calmet, S. Narison, M. Perrottet and E. de Rafael, Phys. Lett. B **61** (1976), 283-286

[113] B. Krause, Phys. Lett. B **390** (1997), 392-400 [arXiv:hep-ph/9607259 [hep-ph]].

[114] G. Colangelo, M. Hoferichter, A. Nyffeler, M. Passera and P. Stoffer, Phys. Lett. B **735** (2014), 90-91 [arXiv:1403.7512 [hep-ph]].

[115] F. Ignatov, R. N. Pilato, T. Teubner and G. Venanzoni, Phys. Lett. B **848** (2024), 138344 [arXiv:2309.14205 [hep-ph]].

[116] G. Abbiendi *et al.* JINST **16** (2021) no.06, P06005 [arXiv:2102.11111 [hep-ex]].

[117] R. Barbieri and E. Remiddi, Nucl. Phys. B **90** (1975), 233-266

[118] B. e. Lautrup, A. Peterman and E. de Rafael, Phys. Rept. **3** (1972), 193-259

[119] T. Blum, Phys. Rev. Lett. **91** (2003), 052001 [arXiv:hep-lat/0212018 [hep-lat]].

[120] S. Laporta, Talk given at the STRONG 2020 Virtual Workshop on Spacelike and Timelike determination of the Hadronic Leading Order contribution to the Muon g-2, November 26, 2021. https://agenda.infn.it/event/28089/.

[121] M. Passera, Talk given at Inspired by Precision, Symposium in honor of Professor Ettore Remiddis 80th birthday, Accademia delle Scienze, Bologna, Italy, December 10, 2021. https://agenda.infn.it/event/28554.

[122] K. Hagiwara, A. D. Martin, D. Nomura and T. Teubner, Phys. Rev. D **69** (2004), 093003 [arXiv:hep-ph/0312250 [hep-ph]].

[123] K. Hagiwara, A. D. Martin, D. Nomura and T. Teubner, Phys. Lett. B **649** (2007), 173-179 [arXiv:hep-ph/0611102 [hep-ph]].

[124] S. Actis *et al.* [Working Group on Radiative Corrections and Monte Carlo Generators for Low Energies], Eur. Phys. J. C **66** (2010), 585-686 [arXiv:0912.0749 [hep-ph]].

[125] K. Hagiwara, R. Liao, A. D. Martin, D. Nomura and T. Teubner, J. Phys. G **38** (2011), 085003 [arXiv:1105.3149 [hep-ph]].

[126] S. Groote, J. G. Korner and A. A. Pivovarov, Eur. Phys. J. C **24** (2002), 393-405 [arXiv:hep-ph/0111206 [hep-ph]].

[127] M. Hoferichter and T. Teubner, Phys. Rev. Lett. **128** (2022) no.11, 112002 [arXiv:2112.06929 [hep-ph]].

[128] E. Balzani, S. Laporta and M. Passera, PLB in preparation.

[129] D. Bernecker and H. B. Meyer, Eur. Phys. J. A **47** (2011), 148 [arXiv:1107.4388 [hep-lat]].

[130] A. Francis, B. Jaeger, H. B. Meyer and H. Wittig, Phys. Rev. D **88** (2013), 054502 [arXiv:1306.2532 [hep-lat]].

[131] X. Feng, S. Hashimoto, G. Hotzel, K. Jansen, M. Petschlies and D. B. Renner, Phys. Rev. D **88** (2013), 034505 [arXiv:1305.5878 [hep-lat]].

[132] M. Della Morte, A. Francis, V. Gülpers, G. Herdoíza, G. von Hippel, H. Horch, B. Jäger, H. B. Meyer, A. Nyffeler and H. Wittig, JHEP **10** (2017), 020 [arXiv:1705.01775 [hep-lat]].

[133] A. M. Frolov and D. M. Wardlaw, Eur. Phys. J. B **85** (2012), 348 [arXiv:1110.3433 [nucl-th]].

[134] G. Aad *et al.* [ATLAS and CMS], Phys. Rev. Lett. **114** (2015), 191803 [arXiv:1503.07589 [hep-ex]].

[135] M. Aaboud *et al.* [ATLAS], Phys. Lett. B **784** (2018), 345-366 [arXiv:1806.00242 [hep-ex]].

[136] A. M. Sirunyan *et al.* [CMS], JHEP **11** (2017), 047 [arXiv:1706.09936 [hep-ex]].

[137] A. M. Sirunyan *et al.* [CMS], Phys. Lett. B **805** (2020), 135425 [arXiv:2002.06398 [hep-ex]].

[138] M. Aaboud *et al.* [ATLAS], Phys. Lett. B **786** (2018), 223-244 [arXiv:1808.01191 [hep-ex]].

[139] A. M. Sirunyan *et al.* [CMS], Phys. Rev. D **99** (2019) no.11, 112003 [arXiv:1901.00174 [hep-ex]].

[140] G. Aad *et al.* [ATLAS], Eur. Phys. J. C **75** (2015) no.10, 476 [erratum: Eur. Phys. J. C **76** (2016) no.3, 152] [arXiv:1506.05669 [hep-ex]].

[141] V. Khachatryan *et al.* [CMS], Phys. Rev. D **92** (2015) no.1, 012004 [arXiv:1411.3441 [hep-ex]].

[142] A. M. Sirunyan *et al.* [CMS], Phys. Lett. B **792** (2019), 369-396 [arXiv:1812.06504 [hep-ex]].

[143] [ATLAS], "Measurements and interpretations of Higgs-boson fiducial cross sections in the diphoton decay channel using 139 fb1 of pp collision data at $\sqrt{s} = 13$ TeV with the ATLAS detector," ATLAS-CONF-2019-029.

[144] [ATLAS], "Combined measurement of the total and differential cross sections in the $H \to \gamma\gamma$ and the $H \to ZZ^* \to 4\ell$ decay channels at $\sqrt{s} = 13$ TeV with the ATLAS detector," ATLAS-CONF-2022-002.

[145] [CMS], "Measurements of properties of the Higgs boson in the four-lepton final state in proton-proton collisions at $\sqrt{s} = 13$ TeV," CMS-PAS-HIG-19-001.

[146] [ATLAS], "Combined measurements of Higgs boson production and decay using up to 139 fb^{-1} of proton-proton collision data at $\sqrt{s} = 13$ TeV collected with the ATLAS experiment," ATLAS-CONF-2021-053.

[147] [CMS], "Combined Higgs boson production and decay measurements with up to 137 fb^{-1} of proton-proton collision data at $\sqrt{s} = 13$ TeV," CMS-PAS-HIG-19-005.

[148] [ATLAS], "Combined measurements of the mass and signal strength of the Higgs-like boson with the ATLAS detector using up to 25 fb^{-1} of proton-proton collision data," ATLAS-CONF-2013-014.

[149] [CMS], "Combination of standard model Higgs boson searches and measurements of the properties of the new boson with a mass near 125 GeV," CMS-PAS-HIG-13-005.

[150] G. Aad *et al.* [ATLAS], Eur. Phys. J. C **82** (2022), 717 [arXiv:2201.11428 [hep-ex]].

[151] A. M. Sirunyan *et al.* [CMS], JHEP **03** (2020), 131 [arXiv:1912.01662 [hep-ex]].

[152] L. M. Carpenter, T. Han, K. Hendricks, Z. Qian and N. Zhou, Phys. Rev. D **95** (2017) no.5, 053003 [arXiv:1611.05463 [hep-ph]].

[153] G. Perez, Y. Soreq, E. Stamou and K. Tobioka, Phys. Rev. D **93** (2016) no.1, 013001 [arXiv:1505.06689 [hep-ph]].

[154] G. T. Bodwin, F. Petriello, S. Stoynev and M. Velasco, Phys. Rev. D **88** (2013) no.5, 053003 [arXiv:1306.5770 [hep-ph]].

[155] A. L. Kagan, G. Perez, F. Petriello, Y. Soreq, S. Stoynev and J. Zupan, Phys. Rev. Lett. **114** (2015) no.10, 101802 [arXiv:1406.1722 [hep-ph]].

[156] M. König and M. Neubert, JHEP **08** (2015), 012 [arXiv:1505.03870 [hep-ph]].

[157] S. Alte, M. König and M. Neubert, JHEP **12** (2016), 037 [arXiv:1609.06310 [hep-ph]].

[158] M. Aaboud *et al.* [ATLAS], Phys. Lett. B **786** (2018), 134-155 [arXiv:1807.00802 [hep-ex]].

[159] A. Tumasyan *et al.* [CMS], Phys. Lett. B **842** (2023), 137534 [arXiv:2206.03525 [hep-ex]].

[160] I. Brivio, F. Goertz and G. Isidori, Phys. Rev. Lett. **115** (2015) no.21, 211801 [arXiv:1507.02916 [hep-ph]].

[161] F. Bishara, U. Haisch, P. F. Monni and E. Re, Phys. Rev. Lett. **118** (2017) no.12, 121801 [arXiv:1606.09253 [hep-ph]].

[162] N. Vignaroli, Symmetry **14** (2022) no.6, 1183 [arXiv:2205.09449 [hep-ph]].

[163] J. Duarte-Campderros, G. Perez, M. Schlaffer and A. Soffer, Phys. Rev. D **101** (2020) no.11, 115005 [arXiv:1811.09636 [hep-ph]].

[164] J. A. Aguilar-Saavedra, J. M. Cano and J. M. No, Phys. Rev. D **103** (2021) no.9, 095023 [arXiv:2008.12538 [hep-ph]].

[165] Y. Soreq, H. X. Zhu and J. Zupan, JHEP **12** (2016), 045 [arXiv:1606.09621 [hep-ph]].

[166] G. Bonner and H. E. Logan, [arXiv:1608.04376 [hep-ph]].

[167] L. Alasfar, R. Corral Lopez and R. Gröber, JHEP **11** (2019), 088 [arXiv:1909.05279 [hep-ph]].

[168] L. Alasfar, R. Gröber, C. Grojean, A. Paul and Z. Qian, JHEP **11** (2022), 045 [arXiv:2207.04157 [hep-ph]].

[169] A. Falkowski, S. Ganguly, P. Gras, J. M. No, K. Tobioka, N. Vignaroli and T. You, JHEP **04** (2021), 023 [arXiv:2011.09551 [hep-ph]].

[170] F. Yu, Nucl. Part. Phys. Proc. **285-286** (2017), 123-125

[171] F. Yu, JHEP **02** (2017), 083 [arXiv:1609.06592 [hep-ph]].

[172] N. Kauer and G. Passarino, JHEP **08** (2012), 116 [arXiv:1206.4803 [hep-ph]].

[173] F. Caola and K. Melnikov, Phys. Rev. D **88** (2013), 054024 [arXiv:1307.4935 [hep-ph]].

[174] J. M. Campbell, R. K. Ellis and C. Williams, JHEP **04** (2014), 060 [arXiv:1311.3589 [hep-ph]].

[175] C. Englert and M. Spannowsky, Phys. Rev. D **90** (2014), 053003 [arXiv:1405.0285 [hep-ph]].

[176] C. Englert, Y. Soreq and M. Spannowsky, JHEP **05** (2015), 145 [arXiv:1410.5440 [hep-ph]].

[177] S. Weinberg, Phys. Lett. B **91** (1980), 51-55

[178] S. R. Coleman, J. Wess and B. Zumino, Phys. Rev. **177** (1969), 2239-2247

[179] C. G. Callan, Jr., S. R. Coleman, J. Wess and B. Zumino, Phys. Rev. **177** (1969), 2247-2250

[180] B. Grzadkowski, M. Iskrzynski, M. Misiak and J. Rosiek, JHEP **10** (2010), 085 [arXiv:1008.4884 [hep-ph]].

[181] R. Contino, M. Ghezzi, C. Grojean, M. Muhlleitner and M. Spira, JHEP **07** (2013), 035 [arXiv:1303.3876 [hep-ph]].

[182] G. Blankenburg, J. Ellis and G. Isidori, Phys. Lett. B **712** (2012), 386-390 [arXiv:1202.5704 [hep-ph]].

[183] R. Harnik, J. Kopp and J. Zupan, JHEP **03** (2013), 026 [arXiv:1209.1397 [hep-ph]].

[184] E. E. Jenkins, A. V. Manohar and M. Trott, JHEP **01** (2014), 035 [arXiv:1310.4838 [hep-ph]].

[185] D. Egana-Ugrinovic, S. Homiller and P. Meade, Phys. Rev. Lett. **123** (2019) no.3, 031802 [arXiv:1811.00017 [hep-ph]].

[186] D. Egana-Ugrinovic, S. Homiller and P. R. Meade, Phys. Rev. D **100** (2019) no.11, 115041 [arXiv:1908.11376 [hep-ph]].

[187] S. Bar-Shalom and A. Soni, Phys. Rev. D **98** (2018) no.5, 055001 [arXiv:1804.02400 [hep-ph]].

[188] M. Cepeda, S. Gori, P. Ilten, M. Kado, F. Riva, R. Abdul Khalek, A. Aboubrahim, J. Alimena, S. Alioli and A. Alves, *et al.* CERN Yellow Rep. Monogr. **7** (2019), 221-584 [arXiv:1902.00134 [hep-ph]].

[189] C. Anastasiou, C. Duhr, F. Dulat, E. Furlan, T. Gehrmann, F. Herzog, A. Lazopoulos and B. Mistlberger, JHEP **05** (2016), 058 [arXiv:1602.00695 [hep-ph]].

[190] E. Balzani, R. Gröber and M. Vitti, "Light-quark Yukawa couplings from off-shell Higgs production," [arXiv:2304.09772 [hep-ph]].

[191] D. Dicus, T. Stelzer, Z. Sullivan and S. Willenbrock, Phys. Rev. D **59** (1999), 094016 [arXiv:hep-ph/9811492 [hep-ph]].

[192] C. Balazs, H. J. He and C. P. Yuan, Phys. Rev. D **60** (1999), 114001 [arXiv:hep-ph/9812263 [hep-ph]].

[193] R. V. Harlander and W. B. Kilgore, Phys. Rev. D **68** (2003), 013001 [arXiv:hep-ph/0304035 [hep-ph]].

[194] A. Djouadi, J. Kalinowski and M. Spira, Comput. Phys. Commun. **108** (1998), 56-74 [arXiv:hep-ph/9704448 [hep-ph]].

[195] A. Djouadi *et al.* [HDECAY], Comput. Phys. Commun. **238** (2019), 214-231 [arXiv:1801.09506 [hep-ph]].

[196] D. de Florian *et al.* [LHC Higgs Cross Section Working Group], [arXiv:1610.07922 [hep-ph]].

[197] G. Aad *et al.* [ATLAS], Eur. Phys. J. C **80** (2020) no.10, 957 [erratum: Eur. Phys. J. C **81** (2021) no.1, 29; erratum: Eur. Phys. J. C **81** (2021) no.5, 398] [arXiv:2004.03447 [hep-ex]].

[198] T. Hahn, "Generating Feynman diagrams and amplitudes with FeynArts 3," Comput. Phys. Commun. **140** (2001), 418-431 [arXiv:hep-ph/0012260 [hep-ph]].

[199] M. Vitti, 'Virtual QCD Corrections via a Transverse Momentum Expansion for Gluon-Initiated ZH and ZZ Production", PhD Thesis, Rome III University, 2022.

[200] G. P. Lepage, "A New Algorithm for Adaptive Multidimensional Integration," J. Comput. Phys. **27** (1978), 192

[201] B. Mele, P. Nason and G. Ridolfi, Nucl. Phys. B **357** (1991), 409-438

[202] G. Panico, F. Riva and A. Wulzer, Phys. Lett. B **776** (2018), 473-480 [arXiv:1708.07823 [hep-ph]].

[203] A. Azatov, J. Elias-Miro, Y. Reyimuaji and E. Venturini, JHEP **10** (2017), 027 [arXiv:1707.08060 [hep-ph]].

[204] J. M. Campbell, R. K. Ellis, E. Furlan and R. Röntsch, Phys. Rev. D **90** (2014) no.9, 093008 [arXiv:1409.1897 [hep-ph]].

[205] J. Alwall, R. Frederix, S. Frixione, V. Hirschi, F. Maltoni, O. Mattelaer, H. S. Shao, T. Stelzer, P. Torrielli and M. Zaro, JHEP **07** (2014), 079 [arXiv:1405.0301 [hep-ph]].

[206] F. Cascioli, T. Gehrmann, M. Grazzini, S. Kallweit, P. Maierhöfer, A. von Manteuffel, S. Pozzorini, D. Rathlev, L. Tancredi and E. Weihs, Phys. Lett. B **735** (2014), 311-313 [arXiv:1405.2219 [hep-ph]].

[207] M. Grazzini, S. Kallweit and D. Rathlev, Phys. Lett. B **750** (2015), 407-410 [arXiv:1507.06257 [hep-ph]].

[208] G. Heinrich, S. Jahn, S. P. Jones, M. Kerner and J. Pires, JHEP **03** (2018), 142 [arXiv:1710.06294 [hep-ph]].

[209] D. A. Dicus, C. Kao and W. W. Repko, "Gluon Production of Gauge Bosons," Phys. Rev. D **36** (1987), 1570

[210] E. W. N. Glover and J. J. van der Bij, "Z BOSON PAIR PRODUCTION VIA GLUON FUSION," Nucl. Phys. B **321** (1989), 561-590

[211] U. Aglietti, R. Bonciani, G. Degrassi and A. Vicini, JHEP **01** (2007), 021 [arXiv:hep-ph/0611266 [hep-ph]].

[212] C. Anastasiou, S. Beerli, S. Bucherer, A. Daleo and Z. Kunszt, JHEP **01** (2007), 082 [arXiv:hep-ph/0611236 [hep-ph]].

[213] R. Harlander and P. Kant, JHEP **12** (2005), 015 [arXiv:hep-ph/0509189 [hep-ph]].

[214] A. von Manteuffel and L. Tancredi, JHEP **06** (2015), 197 [arXiv:1503.08835 [hep-ph]].

[215] F. Caola, K. Melnikov, R. Röntsch and L. Tancredi, Phys. Rev. D **92** (2015) no.9, 094028 [arXiv:1509.06734 [hep-ph]].

[216] B. Agarwal, S. P. Jones and A. von Manteuffel, JHEP **05** (2021), 256 [arXiv:2011.15113 [hep-ph]].

[217] C. Brønnum-Hansen and C. Y. Wang, JHEP **05** (2021), 244 [arXiv:2101.12095 [hep-ph]].

[218] U. Haisch and G. Koole, JHEP **02** (2022), 030 [arXiv:2111.12589 [hep-ph]].

[219] L. Buonocore, G. Koole, D. Lombardi, L. Rottoli, M. Wiesemann and G. Zanderighi, JHEP **01** (2022), 072 [arXiv:2108.05337 [hep-ph]].

[220] R. D. Ball *et al.* [NNPDF], Eur. Phys. J. C **82** (2022) no.5, 428 [arXiv:2109.02653 [hep-ph]].

[221] [ATLAS], "Evidence of off-shell Higgs boson production and constraints on the total width of the Higgs boson in the $ZZ \to 4\ell$ and $ZZ \to 2\ell 2\nu$ decay channels with the ATLAS detector," ATLAS-CONF-2022-068.

[222] M. Aaboud *et al.* [ATLAS], "Measurement of the four-lepton invariant mass spectrum in 13 TeV proton-proton collisions with the ATLAS detector," JHEP **04** (2019), 048 [arXiv:1902.05892 [hep-ex]].

[223] G. Cowan, K. Cranmer, E. Gross and O. Vitells, "Asymptotic formulae for likelihood-based tests of new physics," Eur. Phys. J. C **71** (2011), 1554 [erratum: Eur. Phys. J. C **73** (2013), 2501] [arXiv:1007.1727 [physics.data-an]].

[224] [ATLAS], "Projections for measurements of Higgs boson cross sections, branching ratios, coupling parameters and mass with the ATLAS detector at the HL-LHC," ATL-PHYS-PUB-2018-054.

[225] [CMS], "Sensitivity projections for Higgs boson properties measurements at the HL-LHC," CMS-PAS-FTR-18-011.

[226] I. Brivio *et al.* "Truncation, validity, uncertainties," [arXiv:2201.04974 [hep-ph]].

Acknowledgements

The doctoral training journey has been one of the most challenging experiences, during which I chose to fully engage and invest myself. Having now reached the final milestone, I would like to express my gratitude to those who accompanied and supported me on this journey.

First of all, I want to thank my supervisor, Dr. Massimo Passera. In these three years, he has been constantly motivating me with his uncommon patience, guiding me through my research with invaluable advice. A special thanks for being a reliable source of support during both the joyful and challenging moments of my doctoral journey. Your willingness to share in the difficulties, always offering comfort and encouragement, and consistently pushing me to give my best is truly appreciated. I am particularly grateful for dedicating not only time to read and discuss draft versions of the thesis but also for your involvement in other projects undertaken during the doctoral program. A special thanks also goes to Stefano Laporta. Not only for the engaging physics discussions but also for the assistance and support during the research work. I particularly valued his availability in every stage of drafting and revising the thesis.

I would like to extend my heartfelt gratitude to my co-supervisor, Prof.ssa Ramona Gröber. Taking me under your wing midway through the journey, your guidance and support have been indispensable. Without your mentorship, this thesis would not have come to fruition. Thank you for your unwavering support and guidance throughout. I couldn't be happier and grateful to have you by my side as a supervisor.

I also wanted to thank the people without whom I would literally not be able to write this thesis and exist at all: my father and my mother, who have always encouraged and supported me during my University years. One day I will explain to you what I do in detail, I promise. Thanks to my sister for being there and for the love you have always given me.

An extra special mention goes to my second family, my beloved housemates on Via Marzolo. You've infused every shared moment in our cozy abode with a warmth that is truly irreplaceable. To me, you are more than just friends; you're the ones with whom I've laughed, cried, and created memories that I will hold close to my heart. I've left not just a piece but a piece full of emotions in that apartment, just as you've left an

enduring imprint that I will carry with me always. Each return to Padova felt like a soulful homecoming, a sentiment I owe entirely to you. Though our journeys may take different turns, rest assured, we will forever be more than just friends we are a family, bound by the emotional tapestry we've woven together.

An immense and heartfelt thank you goes out to my dearest friends. These incredible souls have been my unwavering pillars, standing by me through thick and thin, and celebrating each triumph as if it were their own. Their presence has illuminated the darkest days and multiplied the joy of every achievement. I am truly blessed to have friends who share not only in my challenges but also in the sheer delight of every success.

And, finally, I want to express heartfelt gratitude to my other half, Manuel. Your enduring love, steadfast support, and unwavering understanding have been the driving force behind every stride in this journey. Without you by my side, I would never have navigated through the darkest moments. If I can now look back with pride at the achievements, it's because of your constant presence and genuine encouragement. You are my greatest supporter, and I feel your joy in my successes more than words can express. Thank you for being the strength that made all of this possible.